

## REPORT DOCUMENTATION PAGE

Form Approved  
OMB No. 0704-0188

1

Pub  
gac  
coll  
Dev

AD-A234 987



average 1 hour per response, including the time for reviewing instructions, searching existing data sources, gathering the collection of information. Send comments regarding this burden estimate or any other aspect of this report to Washington Headquarters Services, Directorate for Information Operations and Reports, 1215 Jefferson Avenue, Management and Budget, Paperwork Reduction Project (0704-0188), Washington, DC 20503.

1. ATE		3. REPORT TYPE AND DATES COVERED 09/01/87 to 02/28/91	
4. Laboratory Modelling of the Dynamics of Coastal Upwelling		5. FUNDING NUMBERS Contract No. N00014-87-k-0809	
6. AUTHOR(S) T. Maxworthy & S. Narimousa			
7. PERFORMING ORGANIZATION NAME(S) AND ADDRESS(ES) University of Southern California Department of Mechanical Engineering Los Angeles, CA 90089-1453		8. PERFORMING ORGANIZATION REPORT NUMBER	
9. SPONSORING/MONITORING AGENCY NAME(S) AND ADDRESS(ES) Office of Naval Research - Thomas Kinder Code 1121CS 800 North Quincy Street Arlington, VA 22217-5000		10. SPONSORING/MONITORING AGENCY REPORT NUMBER	
11. SUPPLEMENTARY NOTES DTIC ELECTE APR 17 1991			
12a. DISTRIBUTION/AVAILABILITY STATEMENT Approved for public release: Distribution unlimited.		12b. DISTRIBUTION CODE	
13. ABSTRACT (Maximum 200 words) The aim of this research was to study and understand the dynamics of the filamentary structures that have been repeatedly observed by satellite (IR) images taken from the West Coast of the USA, during coastal upwelling episodes. We have simulated such episodes in our laboratory model and generated coastal upwelling fronts and associated jets and eddies. When the experimental model was free of coastal irregularities (capes, ridges, canyons, etc.), the upwelled front was uniform and a train of cyclonic-anticyclonic eddies were formed. Under some circumstances, many of these eddies pinched-off and moved offshore into the fluid interior. We have investigated the structure of such an eddy system and shown that its structure falls within the category of two-dimensional and/or geostrophic turbulence. This in turn suggests that the eddy field contains many turbulent jets or rivers that are responsible for the transport of the passive material and cold, upwelled fluid across the eddy field. To demonstrate this, we have released a passive marker near the front and noted that it was immediately transported offshore by the turbulent jets, and filamentary structures, similar to those seen in the satellite (IR) images, have evolved. When coastal irregularities were included into the system many more eddies were generated and injected into the eddy system.			
14. SUBJECT TERMS		15. NUMBER OF PAGES	
		16. PRICE CODE	
17. SECURITY CLASSIFICATION OF REPORT Unclassified	18. SECURITY CLASSIFICATION OF THIS PAGE Unclassified	19. SECURITY CLASSIFICATION OF ABSTRACT Unclassified	20. LIMITATION OF ABSTRACT UL

NSN 7540-01-280-5500

Standard Form 298 (Rev. 2-89)  
Prescribed by ANSI Std. Z39-18

DTIC FILE COPY

A

91 4 16 001

## **DISCLAIMER NOTICE**

**THIS DOCUMENT IS BEST QUALITY  
PRACTICABLE. THE COPY FURNISHED  
TO DTIC CONTAINED A SIGNIFICANT  
NUMBER OF PAGES WHICH DO NOT  
REPRODUCE LEGIBLY.**

## Final Technical Report

Title: Laboratory Modelling of the Dynamics of Constant Upwelling.

Sponsored by: Office of Naval Research

Period: 09-01-87 to 02-28-91, Contract No. N00014-87-k-0809

Accession For	
NTIS ORNAT	<input checked="" type="checkbox"/>
DTIC TAB	<input type="checkbox"/>
Unannounced	<input type="checkbox"/>
Justification	
By	
Distribution/	
Availability Codes	
Dist	Avail and/or
A-1	Special

The subject grant was concerned with the study of dynamics of the filamentary structures that have been repeatedly observed on satellite (IR) images taken of the West Coast of the USA, during coastal upwelling episodes. These filaments have extended several hundreds of kilometers offshore, typically. The main goal of this research was to unravel the mechanisms that cause such filaments. To accomplish this, we have generated model coastal upwelling fronts and associated jets and eddies in our laboratory apparatus. A detailed report follows:



Stratified two-layer fluid systems were brought to solid-body counterclockwise rotation inside a 1m diameter cylindrical tank having a conical bottom. A tangential stress (a model of the wind stress at air-sea interface) was then applied to the top surface of the water by means of a clockwise, differentially-rotating disk. The resulting Ekman-layer flux caused the top layer to spin-down and the interface to rise near the wall and to descend at the center of the tank. As this process continued, the interface between the two layers intersected the top disk, and an axisymmetric front was formed around the outer edge of the tank. The front then migrated in the offshore direction and was replaced by upwelled, sub-surface water at the surface. This process continued, until, eventually a steady state was reached, and the front became stationary. At this stage, the radial pressure gradient caused by front deformation balanced the Coriolis force, on the average. In many cases before this stage was reached i.e. during its migration, the axisymmetric front became unstable to small-scale baroclinic instabilities. Due to nonlinear interactions these instabilities continued to grow until they reached a saturated size that was controlled by the initial, external parameters, defined in the form of a single non-dimensional number  $\theta_* = gh_0/u_* f \lambda$ , (where  $g' = g\delta\rho$  is the reduced gravity,  $h_0$  is the initial depth of the top layer,  $u_*$  is the friction velocity,  $f$  is the Coriolis parameter and  $\lambda$  is the final width of the upwelled water at the surface). At low values of  $\theta_*$  i.e. strong forcing, cyclonic eddies pinched-off from the front and moved offshore into the fluid interior. Combinations of these eddies and those at the front generated a complex meso-scale eddy fields that contained many turbulent jets (Narimousa & Maxworthy (1989)). To study the statistical structure of such eddy field, we have measured the kinetic energy spectrum assuming that the field can be considered as a 2D turbulent field. The early results (Narimousa et al. (1991)) have shown that two inertial subranges exist, one of the form,  $k^{-5/3}$ , which

is consistent with that predicted by classical theories for the inverse energy cascade range of 2D turbulence, and one with a slope of  $k^{-5}$  in the so-called, enstrophy cascade range. The latter is steeper than that found from classical theories but in agreement with that reported in high resolution numerical models. In fact, our results are the first physical evidence that support the latest results obtained in recent numerical modelling of 2D-turbulence (Narimousa et al. (1991)). When a passive marker was released near the upwelled front it was transported offshore by the jet flow of the eddy field in the form of thin filaments similar to those seen repeatedly in the satellite (IR) images taken of the West Coast of the USA. These results have suggested that the prototype systems we are attempting to model can also be considered to be a 2D and/or geostrophic turbulent field at large scales. Since jet-like structures and/or rivers evolve in such a field in the laboratory (Narimousa & Maxworthy (1989)), then presumably they do so also in the natural flow. This helps to explain the observed filamentary structure which transport passive markers, e.g. heat and marine life.

Of the other important features off the West Coast of the USA, also revealed repeatedly by satellite (IR) images, the most dramatic are the large off-shore extending standing waves which are created by coastal protuberances. These standing waves play a significant role in the initiation of the flows that transport the coastal upwelled water off-shore. The satellite (IR) images clearly show that such events always takes place at locations like the extensive Mendocino Ridge. From looking at many satellite (IR) images for different years (Narimousa & Maxworthy (1989)) it has become obvious that the interaction of coastal upwelling systems with the Mendocino Ridge causes such standing waves. Therefore, as a first attempt, we introduced a bottom topography in our experiment, consisting of a steep upward slope with a maximum height at the wall of the tank, gradually reducing to zero near the center of the tank. In later experiments we modified the bottom topography by introducing a steep downward slope, downstream of the upward slope. When such bottom topographic features interacted with the coastal upwelling system standing waves were formed over the ridge and downstream in a similar fashion to those seen in the satellite (IR) images near the Mendocino Ridge. Our results have thus suggested that it is the Mendocino Ridge that initiates those standing features. A comprehensive application of our results to prototype field situation (West Coast of the USA, Mexico & Peru) is reported in Narimousa & Maxworthy (1989).

#### Publications:

S. Narimousa and T. Maxworthy. "Application of a laboratory model to the interpretation of satellite and field observations of coastal upwelling." Dyn. Atmos. Oceans. (1989) 13, 1-46.



S. Narimousa, T. Maxworthy, and G. R. Spedding. "Experiments on forced, Quasi two-dimensional turbulence at Upwelling Fronts." Proceedings of Seventh Symposium on Turbulent Shear Flows. September, 1989, Grenoble, France.

S. Narimousa and T. Maxworthy. "Effects of Coastline Perturbations on Coastal Currents and Fronts". Stratified Flows, Edited by E. J. List and G. H. Jirka (1990), 194-203.

S. Narimousa, T. Maxworthy and G. R. Spedding. "Experiments on Structure and dynamics forced, Quasi two-dimensional turbulence." J. Fluid Mech., (1991), 223, 113-133.

S. Narimousa. Homogeneous rotating flow past a coastal submarine ridge. Submitted to J. Geophys. Res., (1991).

## APPLICATION OF A LABORATORY MODEL TO THE INTERPRETATION OF SATELLITE AND FIELD OBSERVATIONS OF COASTAL UPWELLING

S. NARIMOUSA and T. MAXWORTHY \*

*Department of Mechanical Engineering, University of Southern California,  
Los Angeles, CA 90089-1453 (U.S.A.)*

(Received January 27, 1988; revised April 22, 1988; accepted May 3, 1988)

### ABSTRACT

Narimousa, S. and Maxworthy, T., 1989. Application of a laboratory model to the interpretation of satellite and field observations of coastal upwelling. *Dyn. Atmos. Oceans*, 13: 1-46.

An attempt is made to apply the results of our laboratory modeling of coastal upwelling to similar events off the west coasts of major continental masses. These include the west coasts of the U.S.A., Peru, and Baja California, Mexico. For the purpose of the present study, we ran new experiments on the effects of asymmetric ridges (similar to Mendocino escarpment) and a perturbed coastline (similar to that in the neighborhood of Point Conception) on the upwelling and the overall results were similar to symmetric cases reported in our previous studies. In general, the model suggests that the large, standing features (waves) that extend far off-shore and which are seen repeatedly in satellite (IR) images near major capes and ridges are produced as the result of interaction of the upwelling system with the coastal irregularities themselves. In the absence of any major coastal protuberances the standing features are absent also, and instead a uniform upwelled front and associated smaller scale, frontal, baroclinic eddies develop. The baroclinic eddies generated at the upwell front, those pinched-off from the upwelling system and/or those pre-existing off-shore combine to produce a complex eddy field. Measurements of the turbulent characteristics of such a field in our laboratory model have indicated that the structure of these eddies is two dimensional and geostrophic. When such eddy fields interact with the upwelling system, geostrophic jets transport the upwelled water far off-shore in the form of meandering filaments, as seen in (IR) images.

An estimate of the value of the control parameter  $\theta^* = g'h_0/u^*f\lambda_c$  (where  $g' = g\delta\rho$  is the reduced gravity,  $\delta\rho$  the density difference between top and bottom layers,  $h_0$  the depth of the top layer,  $u^*$  the friction velocity applied to the top surface,  $f$  the Coriolis parameter and  $\lambda_c$  the final width of the upwelled water at surface) for the above-mentioned regions gave values of  $< 6$ . Under such circumstances, our model predicts that the standing features and the uniform upwelled front should eventually become unstable and grow to allow cyclonic eddies to pinch-off from the upwelling system, as seen repeatedly in satellite (IR) images. An

---

\* Also: Department of Aerospace Engineering, U.S.C. and Earth & Space Sciences Division, Jet Propulsion Laboratory, Pasadena, CA, U.S.A.

estimate of a topographic Rossby  $\beta$  number,  $R_\beta$  (see section 4.1.2), for the west coast of the U.S.A. and the laboratory model yielded a value of about  $R_\beta \approx 0.1$  for both cases, leading us to believe in the similarity between the field and the laboratory flow. When our measurements of the characteristics of the upwelling system are compared with those seen and measured from such images and field observations, we find reasonable, and in some cases excellent, agreement.

## 1. INTRODUCTION

Large-amplitude, standing features extending far off-shore are often associated with coastal perturbations in satellite (IR) images and field observations of the west coasts of the U.S.A., Peru, and Baja California, Mexico. For example, a variety of such images, taken of the west coast of the U.S.A. (Ikeda and Emery, 1984; Mooers and Robinson, 1984; Breaker, 1985; Flament et al., 1985; Breaker and Moores, 1986; and Pelaez and McGowan, 1986), have repeatedly indicated association of the standing features with major coastal perturbations. A satellite (IR) image released by NASA has shown the presence of large, distinct standing features, near large capes off Baja California (shown here as Fig. 24). Although we know of no satellite (IR) images of the upwelling system off Peru, there are reports (Brink et al., 1980) indicating the presence of standing waves near major coastal perturbations. These features usually transport a large quantity of the coastal upwelled water far off-shore. Numerical simulations (Peffley and O'Brien, 1976; Preller and O'Brien, 1980; Ikeda and Emery, 1984), field observations (Brink et al., 1980), and laboratory modeling (Narimousa and Maxworthy 1985, 1986b, 1987a, b, hereafter NM1, NM2, NM3 and NM4, respectively) have demonstrated that these standing features are indeed associated with coastal perturbances. In our experiments we have observed permanent, standing plumes or upwelling maxima at ridges, but not at capes; while large-amplitude standing waves (upwelling centers) occurred on the downstream side of both the capes and the ridges (NM1, 2 and 4). When the experiments were free of coastline and bottom perturbations (NM3) the standing waves were absent and usually a uniform, migrating, upwelled front appeared at the surface. At later times this front became unstable to baroclinic instabilities to form circular cyclonic and anticyclonic eddies. In the presence of any coastal perturbations, baroclinic instabilities appeared only upstream or far downstream of the perturbations. In some experiments (NM2) we introduced an off-shore curl in the surface stress, which generated off-shore eddies. One important role of these eddies was to transport a large quantity of the upwelled water off-shore, in the form of meandering, thin filaments, when they interacted with the upwelled front. To understand the evolution of such filaments in the laboratory, we have investigated the structure of a typical eddy field resulting from the large-amplitude instabil-

ity of an upwelled front. Measurements of wavenumber energy spectra (Narimousa et al., 1987) have indicated that the structure of such an eddy field produces an enstrophy cascade with a steeper energy spectrum than the predictions of two-dimensional turbulence theory (Kraichnan, 1967; Leith, 1968; Batchelor, 1969). This suggested that the turbulence was geostrophic and that meandering, geostrophic, turbulent jets are characteristic of such eddy fields, which are, in turn, mainly responsible for the transportation of material through the field.

When all of the above-mentioned mechanisms together influence the upwelled front, they produce such complicated flow patterns that individual effects may be hard to extract. In the present paper we apply our experimental result to the observed upwelling events, considering each of the above-mentioned perturbations separately. Owing to the limitations of our laboratory model in producing the exact geometry of the natural flow, we only apply those of our results in which the driving effects seem unambiguous and which reasonably resemble flow patterns observed from satellite (IR) images and measured in field experiments.

Among the characteristics of the flow field which we estimate are the wavelength  $L_w = 2\lambda_w$  ( $\lambda_w$  is the average diameter of a circular cyclone or anticyclone at the upwelled front) of the baroclinic instabilities at the upwelled front; the size of the off-shore eddies  $\lambda_0$ ; the distance ( $D_{sw}$ ) of the first and the most significant downstream standing wave, or upwelling center from a cape or a ridge, which produced the wave; the extreme off-shore extension,  $A_{sw}$ , of the first stable, downstream standing-wave trough from the wall of the tank, and that over the ridge,  $A_{sp}$  (see section 3). In our estimation of these lengths we need to determine the value of  $\lambda_s$  (the final width of the upwelled front at the surface far from any perturbations) in order to determine the value of a control parameter  $\theta^* = g'h_0/u^*f\lambda_s$ .

Up to now the coastal perturbations (capes and ridges) used in our laboratory models have had a symmetric shape. Actual, major bottom-topographic and coastline perturbations are often abrupt and their shape is far from symmetrical. As an example, the Mendocino Ridge, which has a strong influence on the upwelling system off the west coast of the U.S.A., has just these characteristics. Because of this we have performed additional experiments where the effects of a similar bottom topography were investigated. Experiments were performed also to investigate the effects of abrupt coastline variations on the upwelling system (see details in sections 2 and 4).

## 2. THE EXPERIMENTS

The experimental model has already been discussed in detail in NM1-4, here, for the sake of convenience, we give a brief discussion of the original model only.

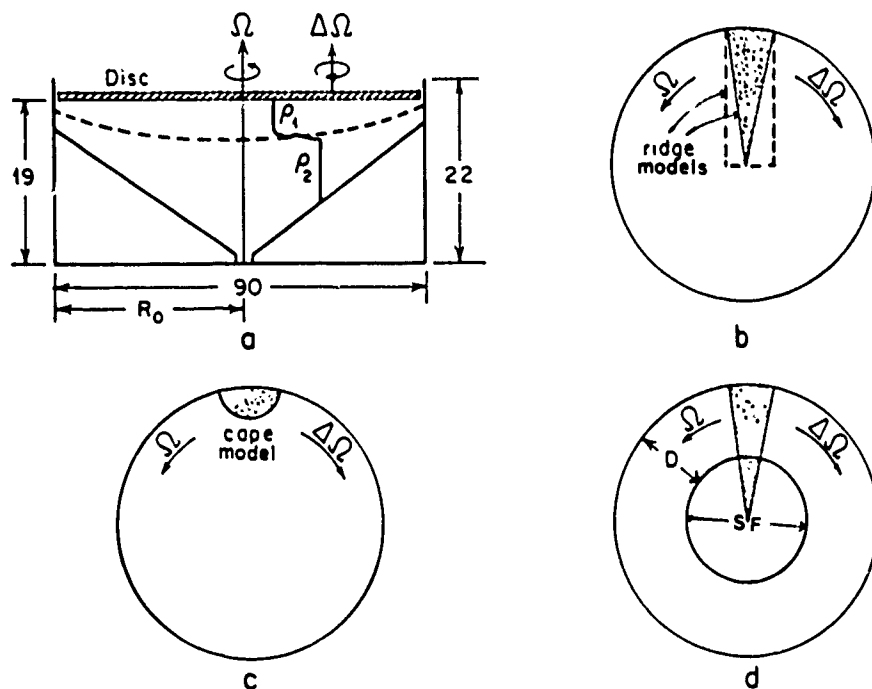


Fig. 1. (a) Cross-sectional side view of the experimental tank (lengths in centimeters). (b and c) Plan view of the tank with (b) a ridge and (c) cape in place. (d) Similar to (b) except here the outer  $D$  cm of the surface of the top water as indicated is stressed, while the inner  $(R_0 - D)$  cm of the surface of the top layer is stress free (SF).

Two layers of salt water of slightly different densities were brought to solid-body counter-clockwise rotation inside a cylindrical tank (90 cm in diameter and 22 cm in depth) having a conical bottom with a slope  $\alpha = 0.27$  (Fig. 1a). The surface of the top fluid was in contact with a circular, smooth disc, so that as it rotated a stress was applied to the top surface of the less dense water, in order to model the wind stress at the air-sea interface. For the purpose of this study the disc was rotated in a clockwise direction opposite to the basic rotation of the apparatus. The applied stress caused the top layer to drift outward and the interface (front) between the two fluids to rise near the wall. As this process continued the front intersected the disc surface and then migrated away from the wall to allow the bottom fluid to appear at the surface around the outer edge of the tank. This frontal movement was observed by placing small neutrally buoyant particles in the front and their motion was recorded by streak photography. The direction of motion of these particles was found by firing an electronic flash at the beginning of the time exposure. In some of our experiments we injected dye into the system to reveal the eddy structure, the standing features and the resulting off-shore jets.

In this laboratory model we have performed experiments to study the effects of, (i) bottom topography (NM1), (ii) bottom topography with an offshore curl in the surface stress (NM2) and (iii) capes (NM4) on coastal

upwelling. We have also investigated, (iv) the characteristics of coastal upwelling when the model was free of all geometric perturbations (NM3). All the experiments were conducted in the same tank with the same bottom slope (Fig. 1a). The plan views of different perturbations are shown in Fig. 1b for a ridge, Fig. 1c for a cape and Fig. 1d for a ridge with a sharp, off-shore cut-off in the surface stress. In the latter case (Fig. 1d) the tank was partially filled so that the surface of the top layer was only in contact with the outer  $D$  cm of the disc, so that the stress applied to the top surface was discontinuous and a surface-stress curl occurred at this location. The cape models (NM4) were manufactured by cutting a cylinder of radius  $R_c$  in half through its vertical axis, these were then placed vertically on the conical bottom, at the wall (Fig. 1c). The ridge models were manufactured by cutting either a cone or a cylinder in half, and these were also placed on the conical bottom as shown in Fig. 1b and 1d.

For the purpose of the present study, we decided to perform new experiments for situations in which the shape of the coastal perturbations

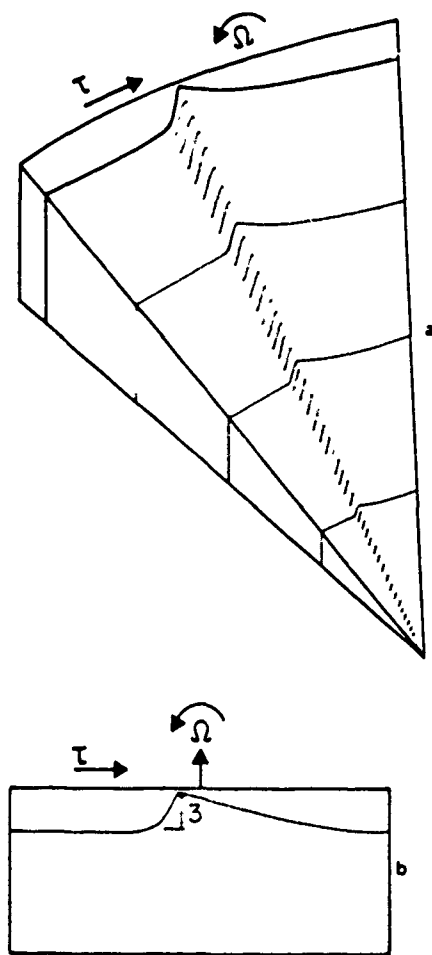


Fig. 2. (a) A perspective view of the sloping bottom with an abrupt, steep slope upstream. This is similar to that at Mendocino Ridge. (b) Side view of the ridge (lengths in cm).

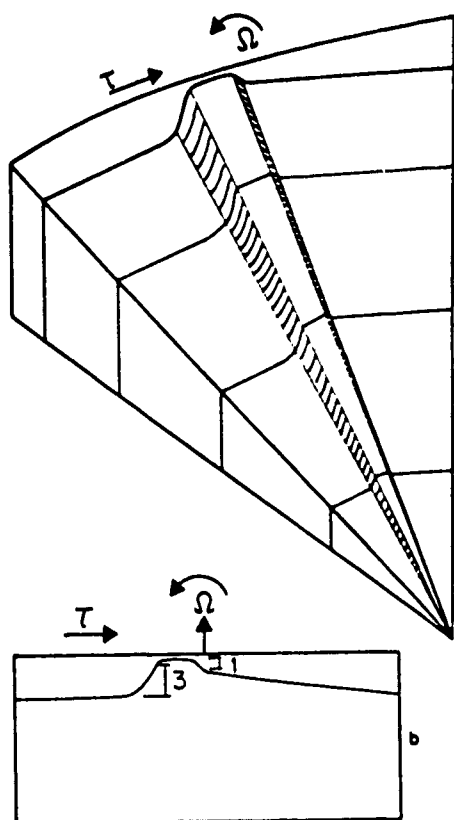


Fig. 3. (a) A modified version of Fig. 2, where a much smaller downward slope is added to the downstream side of the ridge. (b) Side view of the ridge (lengths in cm).

were not symmetric. Typical examples were simple models of the areas like Mendocino Ridge and Point Conception, off the west of the USA. To model a ridge similar to that at Mendocino, we manufactured two types of bottom irregularity. To produce the first type (Case A) it was an easy matter to cut the existing conical bottom radially, thus allowing us to elevate one side of the cut with respect to the other. The maximum elevation (3 cm) occurred at the outer edge of the conical bottom and gradually reduced to zero at the center of the tank. In this way an upward steep slope was produced in the laboratory model, followed by a gentle slope back to the original conical bottom (Fig. 2). To produce the second type (Case B) we modified Case A by creating a downward, steep slope downstream of the one in Case A. The downward slope was made as in Case A, except that the maximum lowering at the outer edge of the conical bottom was about 1 cm (Fig. 3). In this way, bottom topography consisted of an upward steep slope on the upstream side followed by a smaller downward steep slope on the downstream side. In both Case A and B the bottom topography was non-symmetric, in a way that would produce upwelling features similar to those caused by the Mendocino Ridge. Details of the results are to be found in section 4.1.

Abrupt coastline irregularities like the one at Point Conception and their effect on coastal upwelling are of significant concern. In addition, the

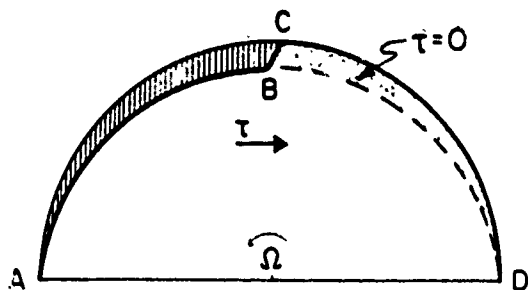


Fig. 4. Plan view of half of the experimental tank with a coastline (ABCD) showing an abrupt change at BC similar to that at Point Conception. The dashed area (ABC) is solid and the dotted area (BCD) is free from the surface stress.

existing field data suggest that the average, along-shore, summer wind stress distribution around Point Conception changes abruptly also. According to Hickey, (1979) and Nelson (1977), the average summer wind stress is large upstream (north) and at Point Conception, while wind is weak downstream of the Point. To investigate the effects of such changes in surface wind stress around an abrupt change in coastline shape we produced a similar situation in the laboratory model. The experimental arrangement is shown in Fig. 4. The vertically shaded area is the new coastline, with zero off-shore extension at point A, and gradually increasing to a maximum ( $\sim 8$  cm) at point B, where it abruptly reduces to zero at point C. In the area BCD, indicated by dots, a stationary plexiglass sheet was placed on top of this area to shield the fluid from any direct effects of the surface stress in this area. The results obtained from this model are discussed in section 4.

### 3. DESCRIPTION OF THE FEATURES OF INTEREST IN THE LABORATORY MODEL

In this section we give a brief discussion to those upwelled features seen in the experiments which will be the subject of our application to similar features seen in the satellite (IR) images and field observations. As mentioned in section 1 an important feature of interest is the average diameter of the baroclinic eddies at the uniform upwelled front  $\lambda_w$ , or alternatively, the wavelength between the two consecutive crests or troughs ( $L_w = 2\lambda_w$ ). These disturbances usually appear at the upwelled front at the surface when the front has migrated a distance, designated  $\lambda_r$ , away from the wall of the tank (details are in NM1 and NM3). Our measurements of  $\lambda_w$  upstream of a ridge, a cape and also in their absence have shown that the value of  $\lambda_w$  within an uncertainty of  $\sim 10\%$ , is the same for all cases (Fig. 5).

Subsequently, when we introduced an off-shore curl in the surface stress, eddies were produced at that location and then moved off-shore (Fig. 6). In



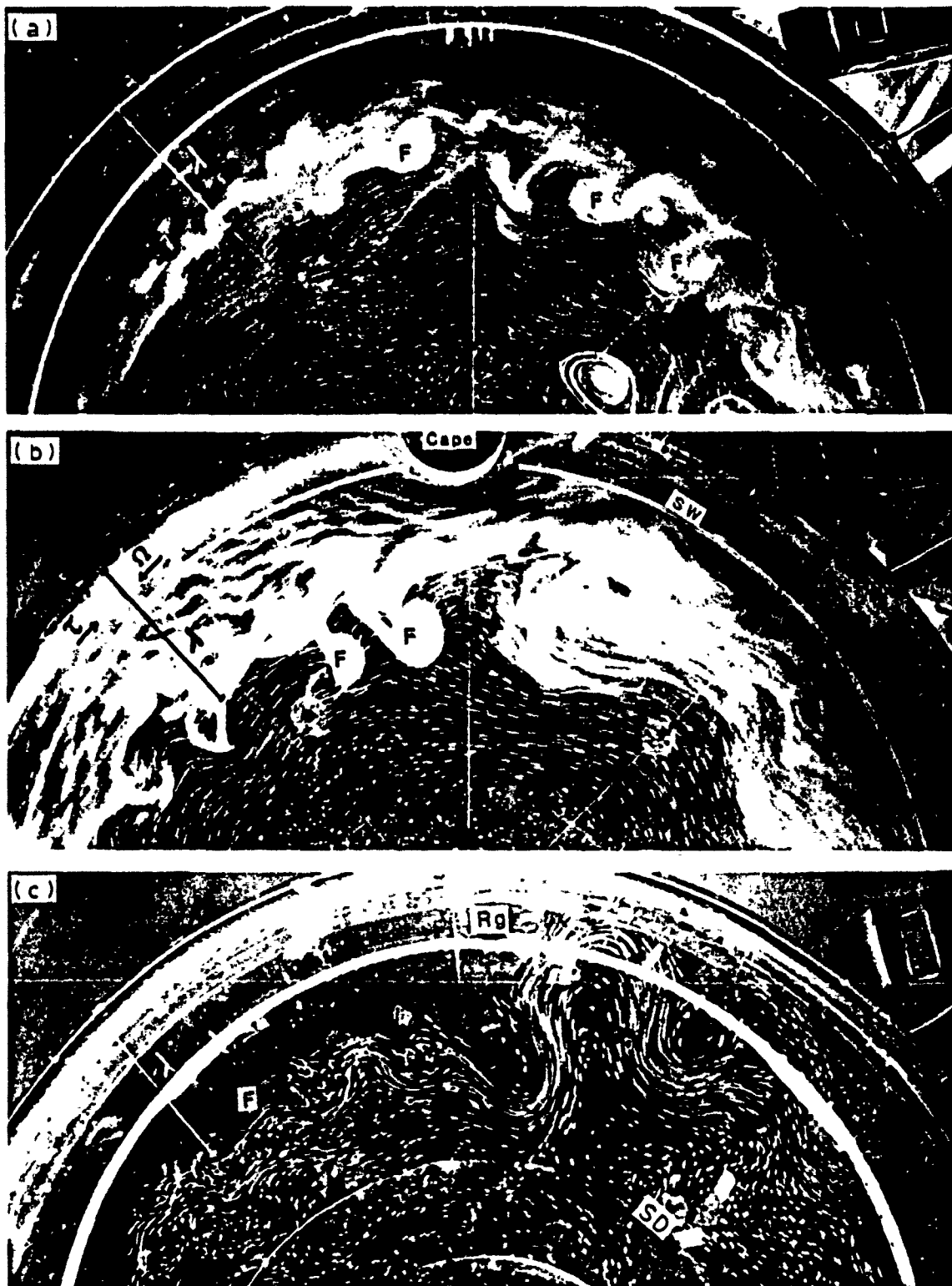


Fig. 5. A set of streak and dye photographs with a 0.5 s time exposure for small values of  $\theta^*$ , showing the effect of different types of perturbation on the coastal current and the upwelled front. Photograph (a) has a value of  $\theta^* \approx 2.2$  and the model is free of coastal perturbations (NM3). Notice the frontal baroclinic waves (F) as shown by dye and particle streaks. Photograph (b) has a value of  $\theta^* \approx 2.2$ , and a cape is introduced into the model. Notice the upstream baroclinic waves approaching the cape and the downstream standing waves caused by the cape. Photograph (c) has a value of  $\theta^* \approx 2.5$ , in this case there is a ridge and an off-shore curl in the surface stress at position (SD). In this photograph the upwelled front did not interact with the stress discontinuity (SD) and frontal baroclinic waves upstream of the ridge are undisturbed by (SD). Notice the maximum upwelling at the ridge in the form of jet

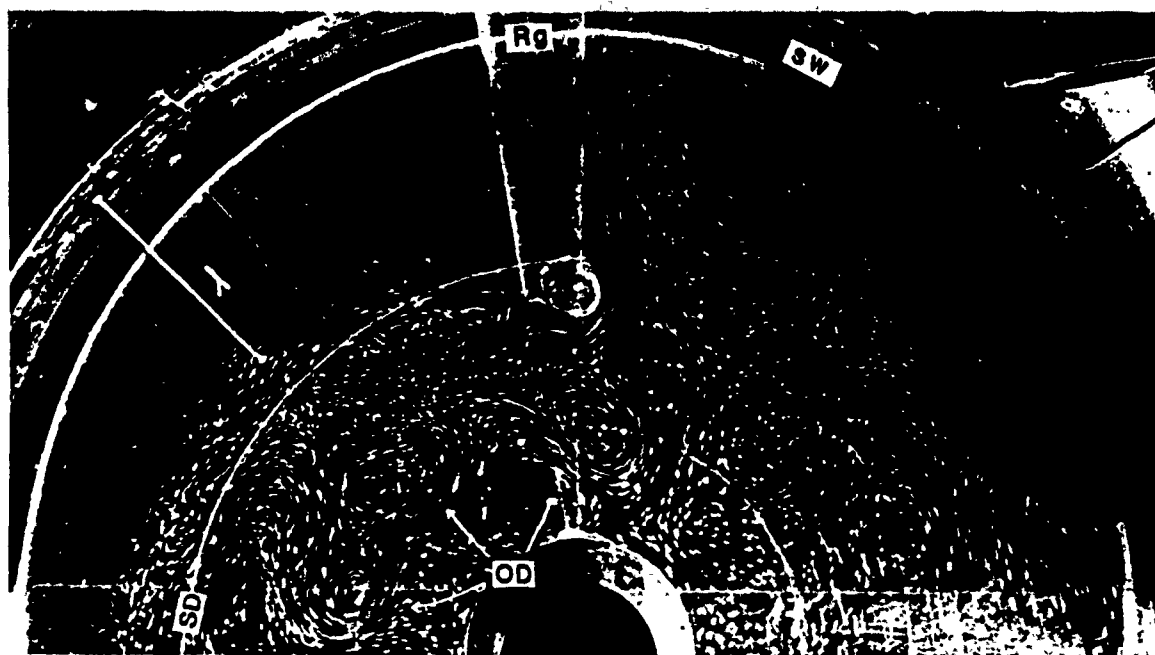
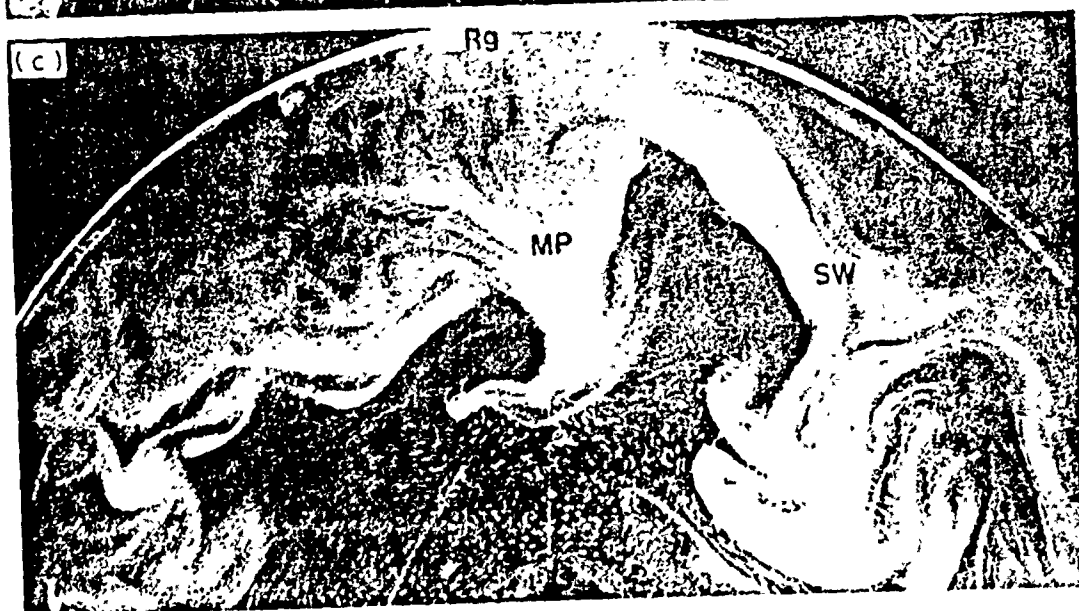
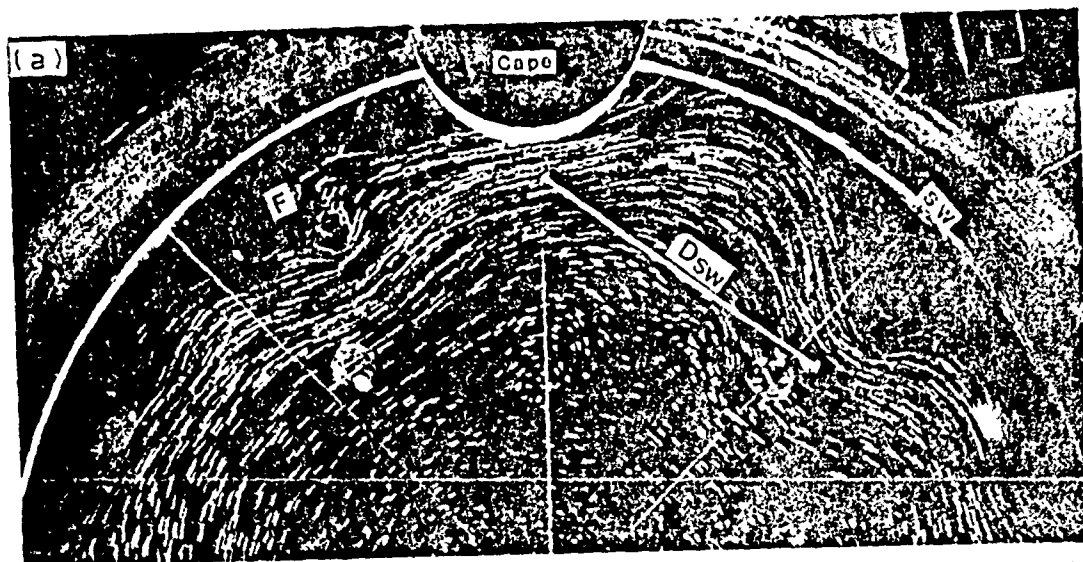


Fig. 6. A streak photograph with a 0.5 s time exposure, with a value of  $\theta^* \approx 2$ . Similar to Fig. 5c, except that here the upwelled front interacted with (SD). The frontal eddies have vanished as separate entities and have become incorporated into a number of large off-shore eddies (OD) which have been produced at the stress free region.

NM2, we showed that these off-shore eddies played an important role in transporting the upwelled water off-shore. Our measurements of the mean diameter  $\lambda_0$  of these off-shore eddies indicated that their size, for a given value of  $\theta^*$ , was about twice the value of that of the frontal eddies, i.e.,  $\lambda_0 \approx 2\lambda_w$  (NM2).

When we introduced a subsurface ridge into the model (Figs. 5 and 7) a maximum upwelling in the form of a high-speed, jet-like plume was produced as a permanent standing feature at the ridge (NM1). The high-speed jet flow extended a considerable distance downstream in the form of standing waves. For values of  $\theta^* > 6$ , the standing wave system was usually stable, while for values of  $\theta^* < 6$  it usually became unstable after about 50 rotation periods, with troughs propagated in the off-shore direction. This wave growth often caused cyclones to pinch-off from the unstable wave troughs. It was these pinched cyclones which played an important role in transporting the upwelled water off-shore (Narimousa and Maxworthy, 1985, 1986a). With the applications in mind, we studied effects of different size ridges on the upwelling system in order to relate ridge geometry to the behavior of the associated standing features (see section 4). In this way, the average height ( $h_r$ ) and width ( $w$ ) of a given ridge together with the average height ( $H$ ) of the adjacent water column appeared in the relations leading to the estimates of  $A_{sp}$ ,  $D_{sw}$  and  $A_{sw}$  given in NM1, with appropriate caveats.



In the case of a cape the situation was somewhat different since the upwelling was not maximum at the cape (Fig. 7a and b), yet standing waves were formed downstream of the cape as well. IN NM4 we studied the effects of different size capes on the upwelled front, and were then able to include the cape geometry into formulations leading to estimates of  $D_{sw}$  and  $A_{sw}$ . At values of  $\theta^* > 6$ , the standing wave caused by a cape was usually stable, while at values of  $\theta^* < 6$ , the standing wave tended to become unstable and repeated the process already discussed above for standing waves caused by a ridge. Also, at values of  $\theta^* < 6$ , often a diverging, rotary-type flow configuration formed between the cape and the downstream standing wave. Such a flow configuration produced long off-shore extending filaments of cold upwelled water.

When we placed the new ridges or capes into the experimental tank (see section 2 and Figs. 2–4), flow patterns were induced which were generally similar to those already discussed for a symmetric ridge or cape. We note the detailed differences in section 4 when the corresponding full-scale flows are discussed.

#### 4. APPLICATIONS OF THE MODEL

##### 4.1. *To the west coast of North America*

###### 4.1.1. *Descriptive*

Of all the important features off the west coast of the U.S.A. the most dramatic are the large off-shore-extending standing waves which are created by coastal protuberances. These standing features play a significant role in the initiation of the transportation of the coastal upwelled water off-shore. For example, see Figs. 8–10 where IR images for the west coast of the U.S.A. are shown. An upwelling maximum in the form of a standing plume

---

Fig. 7. (a) Streak photographs with a 0.5 s time exposure with a value of  $\theta^* \approx 5.5$ , showing flow pattern caused by a single cape. Notice the baroclinic frontal waves upstream and the large stable standing wave downstream of the cape. (b) The long time behavior of (a). Here the standing wave is unstable and has propagated a considerable distance off-shore. When dye was released into the system near the surface, it was transported abruptly off-shore by the unstable wave. In (b) the value of  $A_{sw}$  for an unstable wave is much larger than  $A_{sw}$  for the stable wave in (a). Also notice that there is no upwelling maximum or plume at the cape. (c) A streak and dye photograph with a 0.5 s time exposure showing flow pattern caused by a medium symmetric size ridge (similar to NM1, but 40% smaller in height). Notice upwelling maximum (MP) at the ridge with strong cyclonic circulation and a large unstable standing wave downstream. Also notice that a large quantity of dye is transported off-shore at the ridge and at the unstable standing wave downstream. In both (b) and (c) the unstable wave eventually generates a cyclone from its trough.



at the Mendocino Ridge is clearly shown in these IR images. The existence of this feature is consistent with the upwelling maximum observed over bottom topography in our laboratory model (NM1 and NM2). The variability of the standing feature in the three figures (8–10) is also striking. According to our model this could be related to various flow conditions. For example, detachment of cyclonic eddies from the head of the standing plume (Narimousa and Maxworthy, 1985, 1986a), interaction of the standing plume with off-shore eddies (NM2) and the presence of an off-shore curl in the surface wind stress. When the upwelling maximum at the ridge interacted with the off-shore curl in the wind stress a variety of off-shore-extending features developed (for details see NM2). However, the major difference is that the bottom topography used in our model is symmetric, while the prototype, Mendocino Ridge, is not. As the contour map (see Fig. 19) indicates, Mendocino Ridge consists of a steep slope (an escarpment) to the North (upstream) and a relatively mild slope to the south (downstream). Since such a shape is far from symmetric and because of great concern about its possible, strong effects on coastal currents and fronts, we have produced a similar shape in our model. For the first set of experiments (Case A: Fig. 2) the bottom topography consisted of a steep upward slope with a maximum height at the wall of the tank, gradually reducing to zero near the center of the tank. Under such circumstances, when the fluid columns reached the step, vortex contraction caused the columns to move along the step toward the center of the tank in a jet-like fashion similar to NM1 (see also Maxworthy, 1977). Eventually, at some distance off-shore, the fluid columns flowed over the step and returned inshore to produce an upwelling maximum. Because of the lack of a steep downward step, the return flow immediately downstream was much weaker than that observed in NM1 (see

---

Fig. 8. A satellite (IR) image showing an example of an upwelling event off the west coast of the U.S.A. (taken in June 1981 courtesy of Pierre Flament). A maximum plume (A) at Mendocino Ridge (MD) and a cyclonic rotation at the head of the plume is shown clearly on this (IR) image. The downstream standing wave (B) associated with Mendocino cape and ridge is clearly shown at Point Arena (B). The downstream standing wave (C) caused by Point Arena (PA) is shown near San Francisco Bay. The much weaker bottom topography just off-shore from San Francisco Bay and that at Point Sur also produced maximum plumes (D,E) and standing waves (F) downstream of Point Sur (PS). The downstream standing wave associated with Point Conception (PC) is indicated also (G). Since we have estimated a value of  $\theta^* \approx 5$  for the west coast of the U.S.A. then, according to the prediction by the laboratory model, the above standing features should become unstable and grow in the off-shore direction, which is the case in this (IR) image. Also, the induced flow associated with eddies in the California current system and those associated with the upwelling system itself have produced a number of filaments of cold upwelled water, which extend several hundred kilometres off-shore.

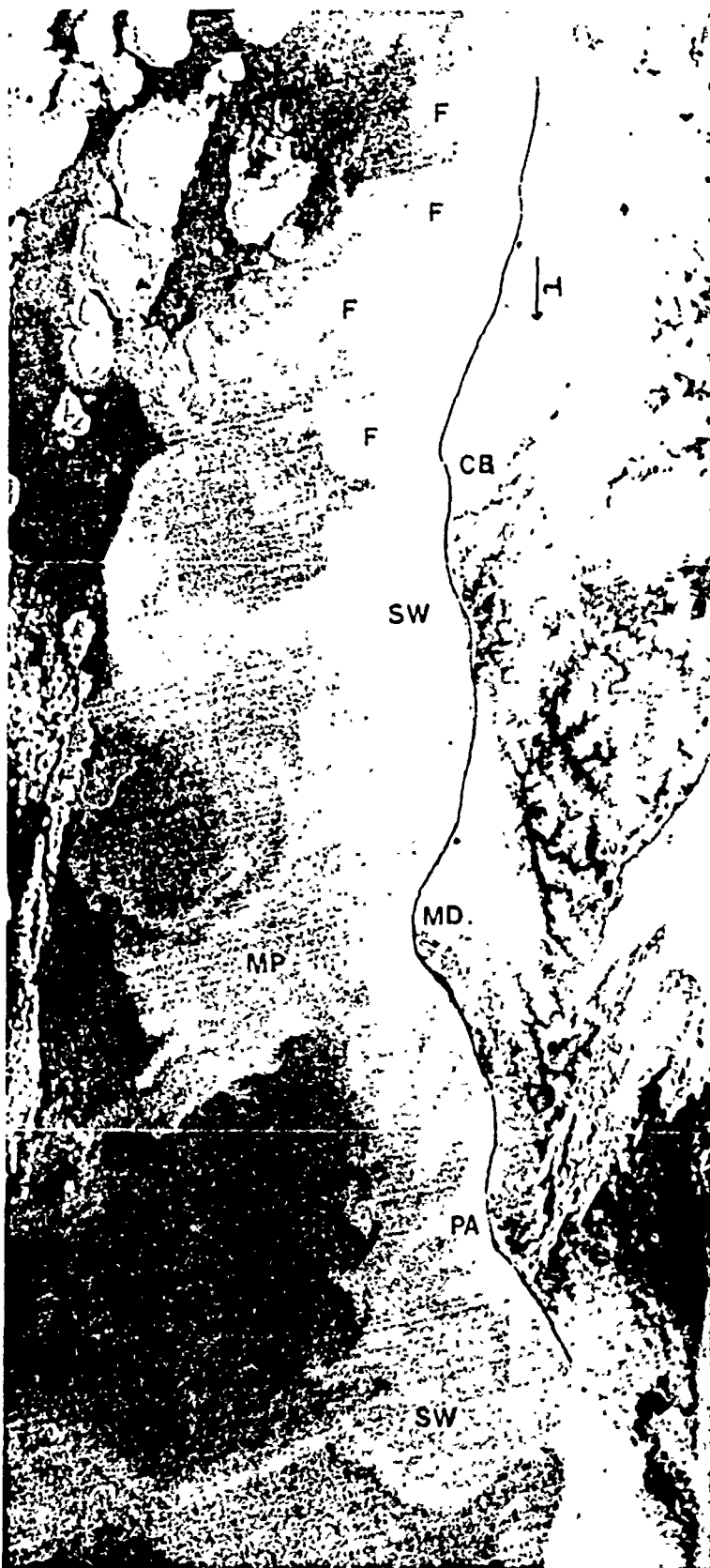


Fig. 9. A satellite (IR) image of an upwelling event, off the west coast of U.S.A. (taken in October 1974). The upwelling maximum at Mendocino Ridge, the downstream standing wave caused by Point Arena and that produced by Cape Blanco (CB) are shown clearly. Upstream of Cape Blanco, the absence of major coastal perturbances has allowed a uniform upwelled front and associated frontal baroclinic eddies (F) to develop. Downstream of Cape Blanco, the presence of major perturbances allowed standing features to develop only (see Fig. 8 and 10 also) and a uniform upwelled front is always absent in this region.

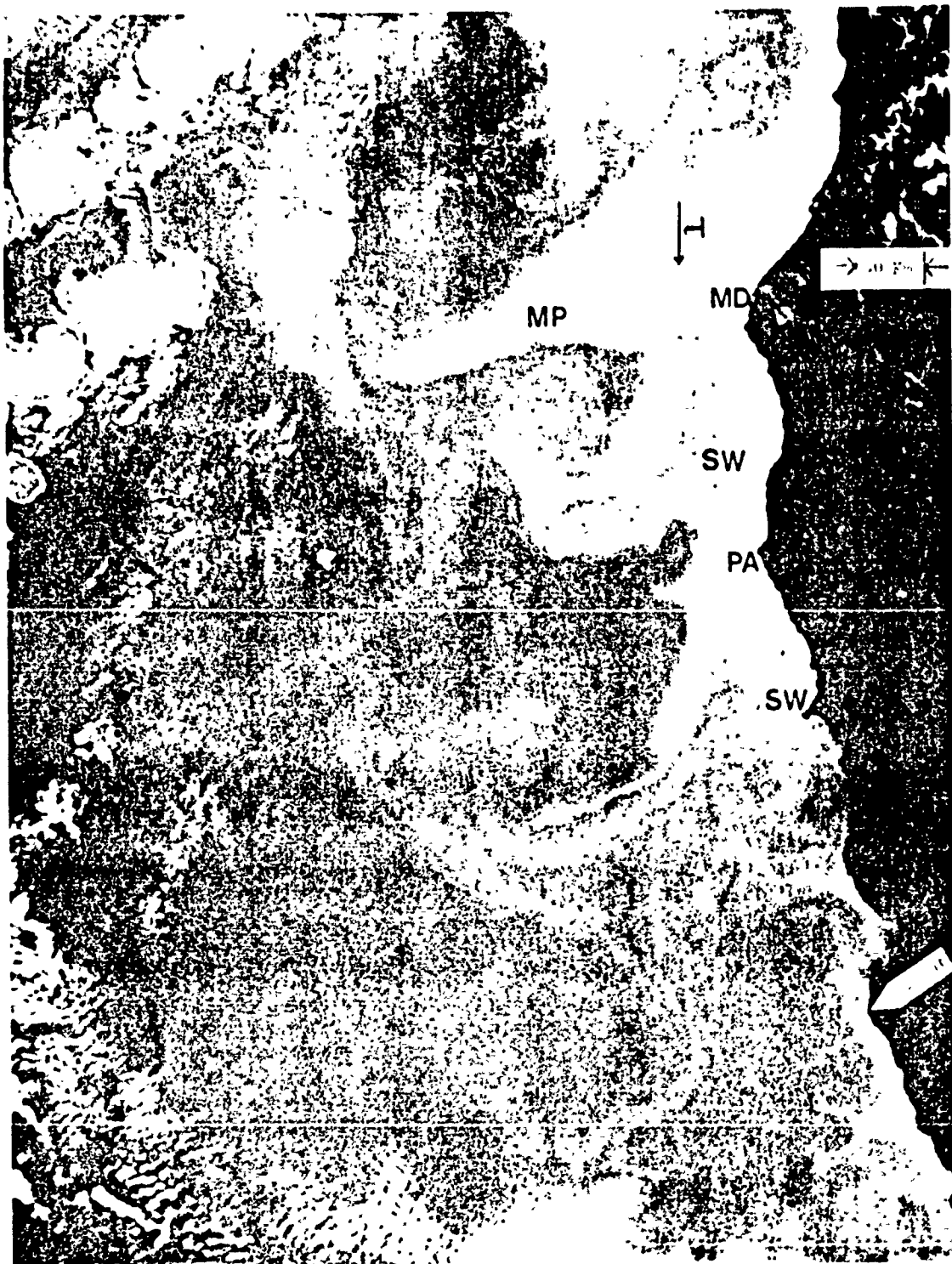


Fig. 10 A satellite (IR) image showing another example of an upwelling system off the west coast of the U.S.A. (taken in September 1980). Upwelling maximum and the downstream standing wave associated with Mendocino perturbances are shown clearly. Also notice the downstream standing wave associated with Point Arena. In this image, as predicted by the model, the indicated standing features are unstable and propagated in the off-shore direction.



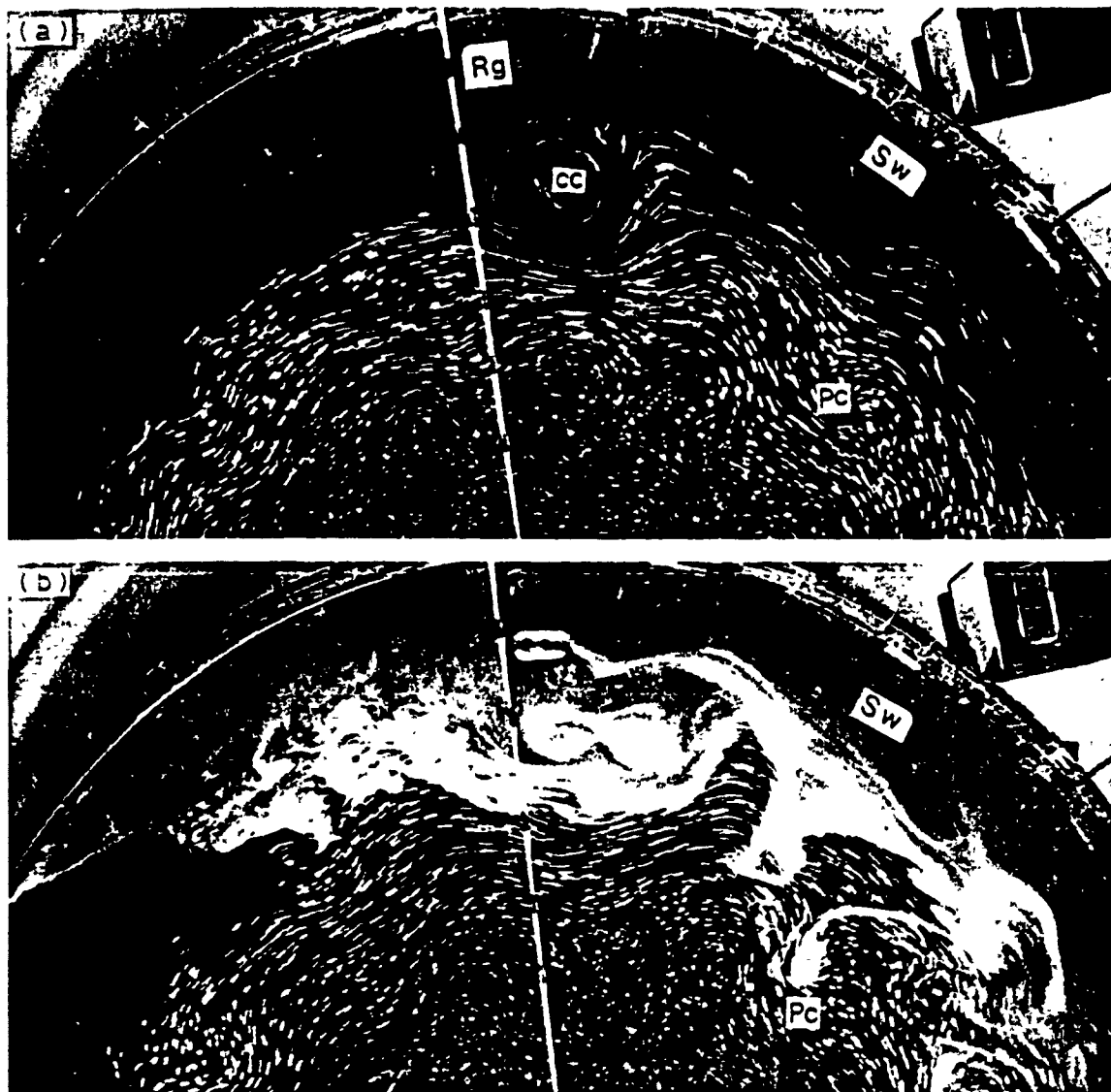


Fig. 11. Streak and dye photographs with 0.5 s time exposure showing the flow pattern caused by the ridge of Case A. Experimental conditions are:  $h_m = 2.5$  cm,  $g' = 19.6$  cm s<sup>-2</sup>,  $f \approx 4$  s<sup>-1</sup>,  $\Delta\Omega = 0.125$  s<sup>-1</sup>,  $u_* = 0.28$  cm s<sup>-1</sup>,  $\lambda_c = 15$  cm and  $\theta_* \approx 3$ . (a) Taken after  $\sim 100 \Omega$ , and shows the resulting upwelling maximum together with cyclonic circulation (CC) over the steep ridge and the standing wave with the associated pinched-off (PC) eddy downstream of the ridge. (b) Taken a few rotation periods later than (a), only here dye is released into the system near the surface. Notice that dye is transported off-shore by the standing wave and the pinched-off eddy. At a later time, as shown in Fig. 12, larger amounts of dye will be transported off-shore by the pinched-off eddy.

Figs. 5c and 7c, and compare with Fig. 11). Nevertheless, as in NM1, a strong cyclonic circulation (eddy) was formed over the step (see Fig. 11). The much weaker downstream jet flow (when compared with NM1) produced weaker standing waves further downstream from the cyclonic circulation. The first of these standing waves at low values of  $\theta_* < 6$  could become unstable in a fashion similar to NM1 to allow cyclonic eddies to pinch-off from its trough (see Fig. 11).

In Case B, we modified the escarpment of Case A by introducing a steep downward slope, downstream of the upward slope in Case A (for details see section 2). In this case, the presence of the smaller downward step caused the fluid columns to move in a fashion intermediate between the two extreme cases, i.e., A and NM1, so that a jet flow, which was stronger than Case A but weaker than that of NM1, was produced downstream of the

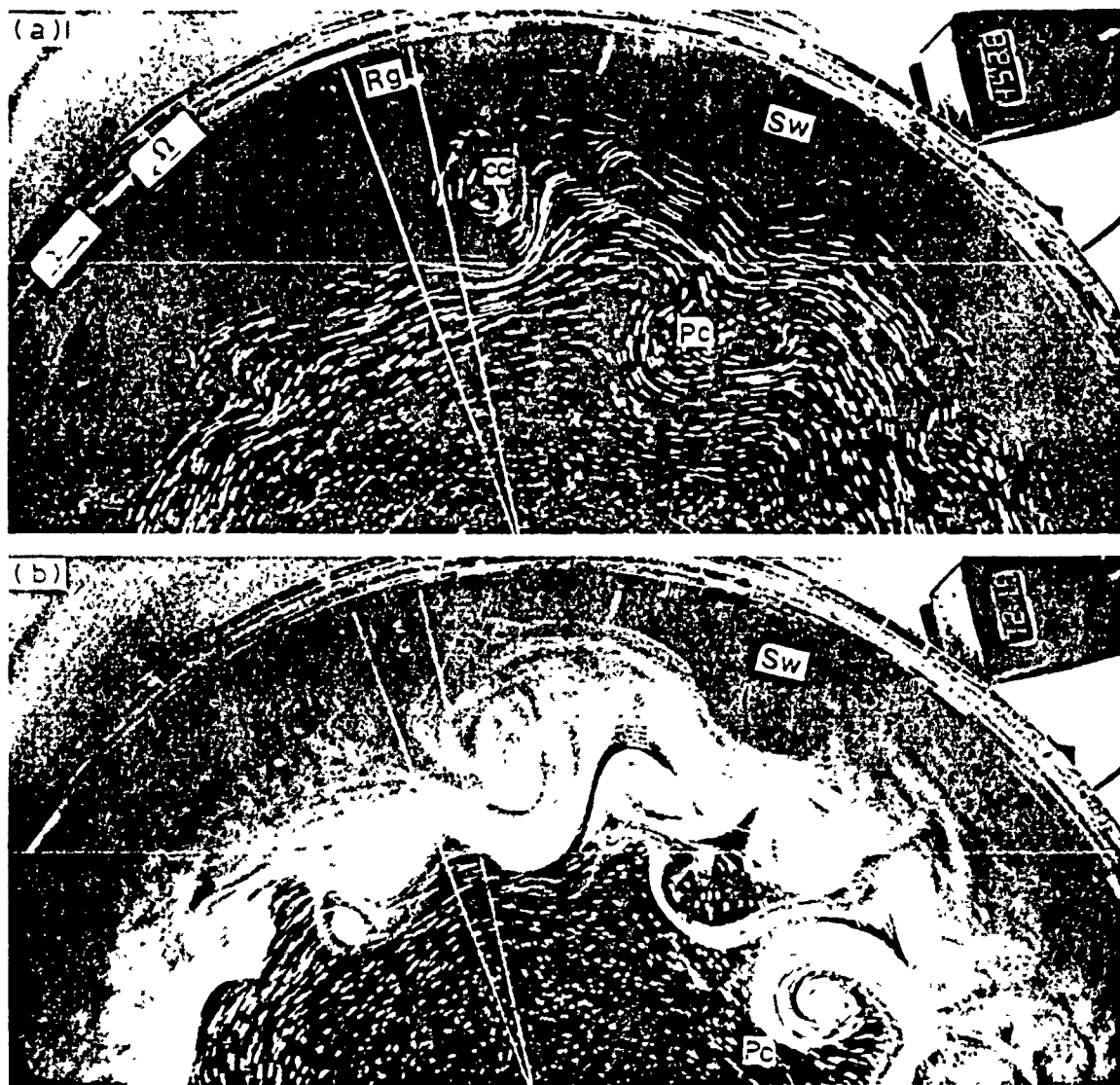


Fig. 12 Streak and dye photographs with 0.5 s time exposure showing the flow pattern caused by the ridge of Case B. Experimental conditions are:  $h = 2.15$  cm,  $g' = 25$  cm s $^{-2}$ ,  $f = 4$  s $^{-1}$ ,  $\Delta\Omega = 0.125$  s $^{-1}$ ,  $u_* \approx 0.28$  cm s $^{-1}$ ,  $\lambda \approx 14.6$  cm and  $\theta_* \approx 3.3$ . (a) Taken after  $\sim 100$   $\Omega$ . Description of the flow pattern as in Fig. 11, only here the downstream slope causes a more intense flow pattern at the ridge and downstream. (b) Taken a few rotation periods later than (a), here dye which is released into the system near the surface is transported off-shore by the standing wave and the associated pinched-off eddy.

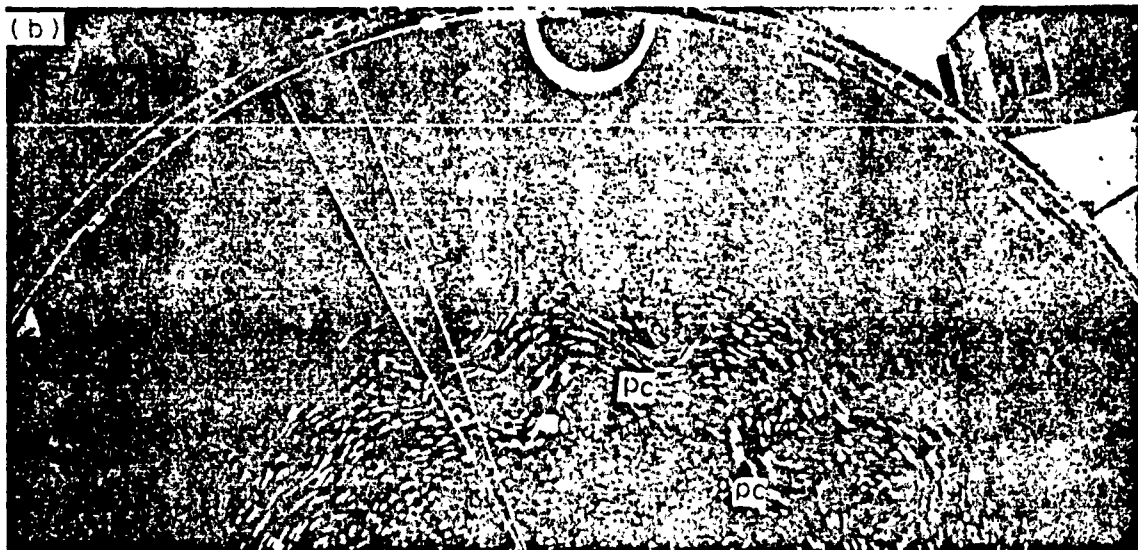
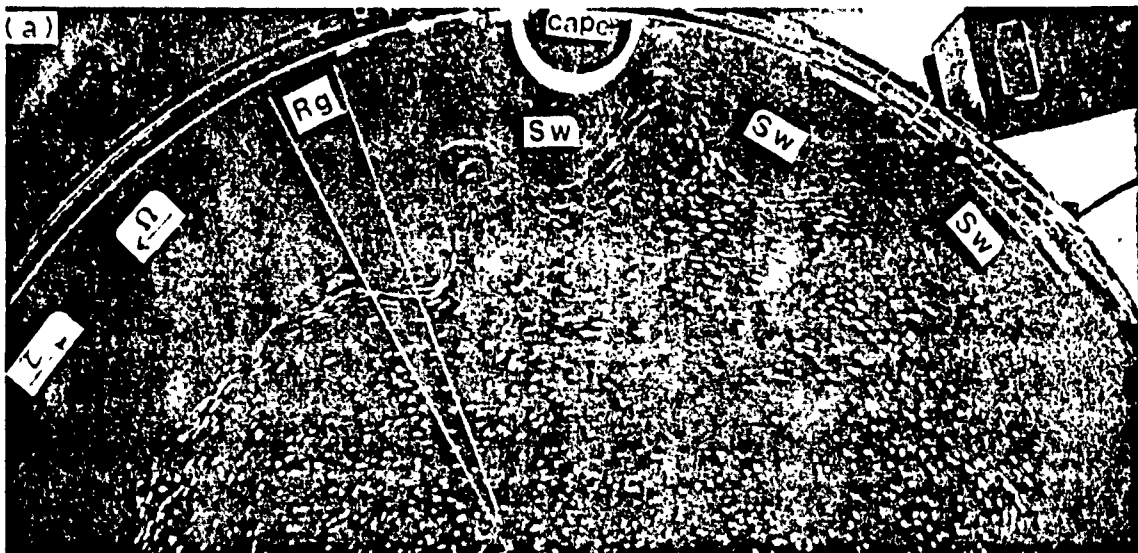
bottom topography in the form of standing waves with characteristics similar, but not identical, to those of NM1 and Case A (Fig. 12).

In general, when we introduced a variety of off-shore-extending symmetric and asymmetric ridges separately into our model an upwelling of maximum off-shore extent was produced at the ridge and standing waves were formed downstream. The smallest ridge used in the model had an average height of  $\sim 0.5$  cm, yet it still produced the above-mentioned features (see Fig. 14). These results alone should help explain the observed upwelling maximum at the Mendocino Ridge and standing waves downstream. We note here that, as shown in NM4 and section 3, capes alone do not produce an upwelling maximum, they produce downstream standing waves only. As we will see later in this section, we estimate that the peak of the first standing wave downstream of the Mendocino Ridge should occur near Point Arena. Satellite (IR) images (Fig. 8, and see Fig. 22) often show such an upwelling maximum at point Arena; our model (NM4) suggests that this maximum is not due to the presence of Point Arena itself, but is part of the large, standing-wave pattern caused by Cape Mendocino and bottom topography. To show this effect, we modified Case B by inserting a model cape some distance downstream of the ridge. We then ran a controlled experiment allowing the first standing wave of the ridge to occur near the cape. The result is shown in Fig. 13. It can be seen that a maximum now exists at the cape, a phenomenon which was not observed when the model consisted of a cape alone. This maximum represents the amplification by the cape of the first downstream standing wave associated with the upstream ridge!

The contour map of bottom topography (see Fig. 19) off the west coast of the U.S.A. indicates the presence of a cape and associated bottom topography at Point Sur, which are considerably smaller than that at Mendocino. Based on our experiment, one would expect that Point Sur should produce

---

Fig. 13. Streak and dye photographs with 0.5 s time exposure showing the flow pattern caused by combination of the ridge of Case B and a cape. Experimental conditions are:  $h_0 = 2.1$  cm,  $g' = 21$  s $^{-2}$ ,  $f = 5$  s $^{-1}$ ,  $\Delta\Omega = 0.123$  s $^{-1}$ ,  $u_* \approx 0.24$  cm s $^{-1}$ ,  $\lambda_r = 17$  cm and  $\theta_* \approx 2$ . Note that these conditions are chosen so that the first downstream standing wave caused by the ridge is almost coincidental with the cape. (a) Flow pattern over the ridge as in Fig. 12. The first standing wave caused by the ridge is formed almost at the cape and one should not assume that this is an upwelling maximum caused by the cape (compare with Fig. 7) as might be assumed from satellite images of Point Arena, for example. Also notice that the second standing wave of the ridge occurred at the position where the standing wave of the cape should occur. Further downstream there exist weaker standing waves. (b) Taken about 20 rotation periods later than (a) shows that the standing waves of (a) are all unstable and many cyclones have pinched-off. (c) Dye is released into the system near the surface and is transported off-shore vigorously by the pinched-off eddies.



standing features similar to those caused by Mendocino. To look in detail at this possibility, we have previously inserted either a small topography or a small cape into our model to examine their effect on coastal upwelling. In NM4 we showed that small capes can produce features similar to a larger

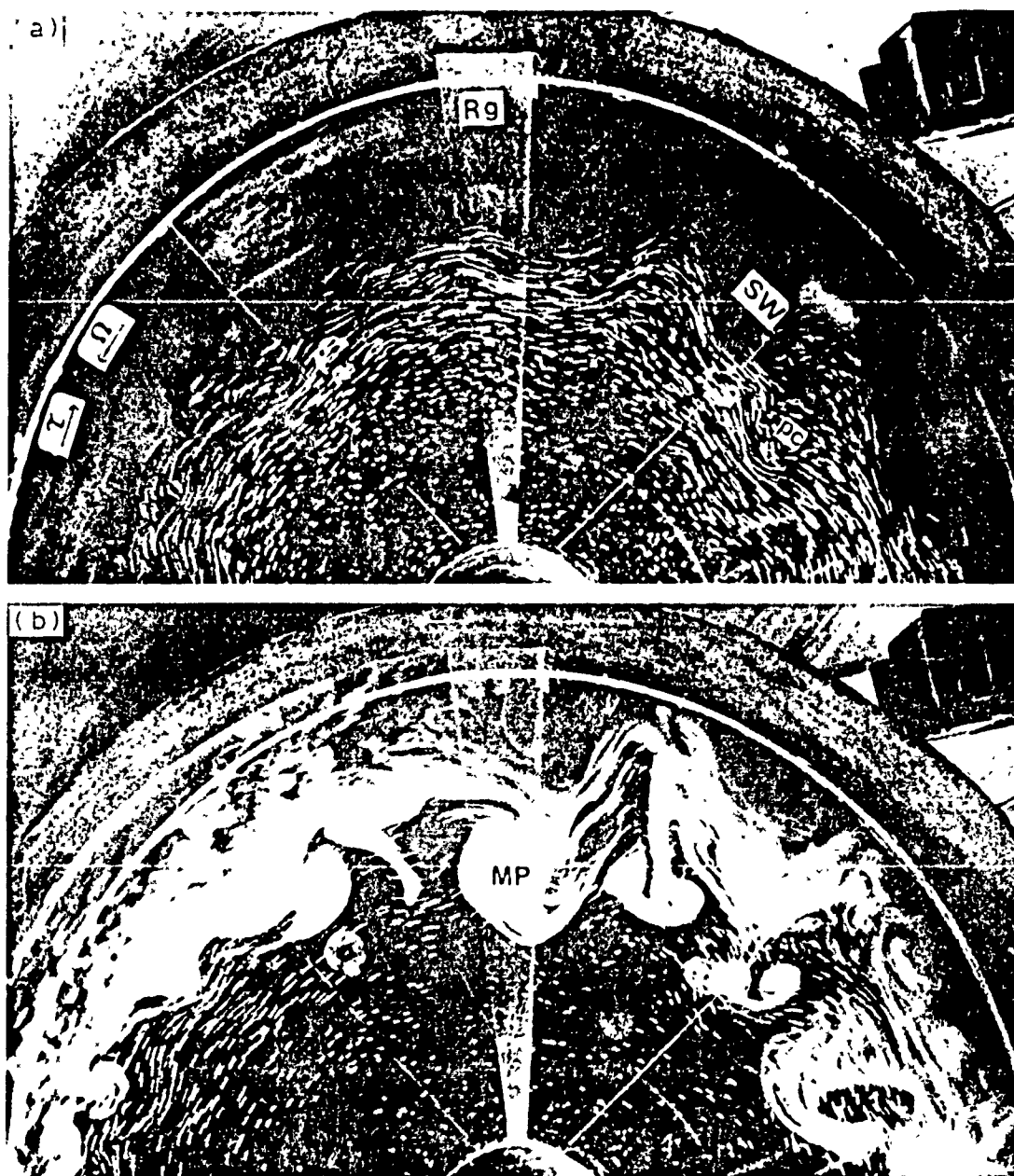


Fig. 14. Streak and dye photographs with 0.5 s time exposure showing the flow pattern caused by a smaller ridge (similar to NM1, but 70% smaller in height). Experimental conditions are:  $h_0 = 2.83$  cm,  $g' = 28.5$  cm s<sup>-2</sup>,  $f = 4.6$  s<sup>-1</sup>,  $\Delta\Omega = 0.15$  s<sup>-1</sup>,  $u^* = 0.34$  cm s<sup>-1</sup>,  $\lambda_c = 13.8$  cm and  $\theta^* = 4$ . (a) Shows an upwelling maximum at the ridge and standing wave with an associated pinched off eddy downstream. These features are much less intense than those observed for a medium or large ridge (see Figs. 5c and 7c). (b) Dye is released into the system near the surface and is transported off-shore by the plume, the standing wave and the pinched-off eddies.

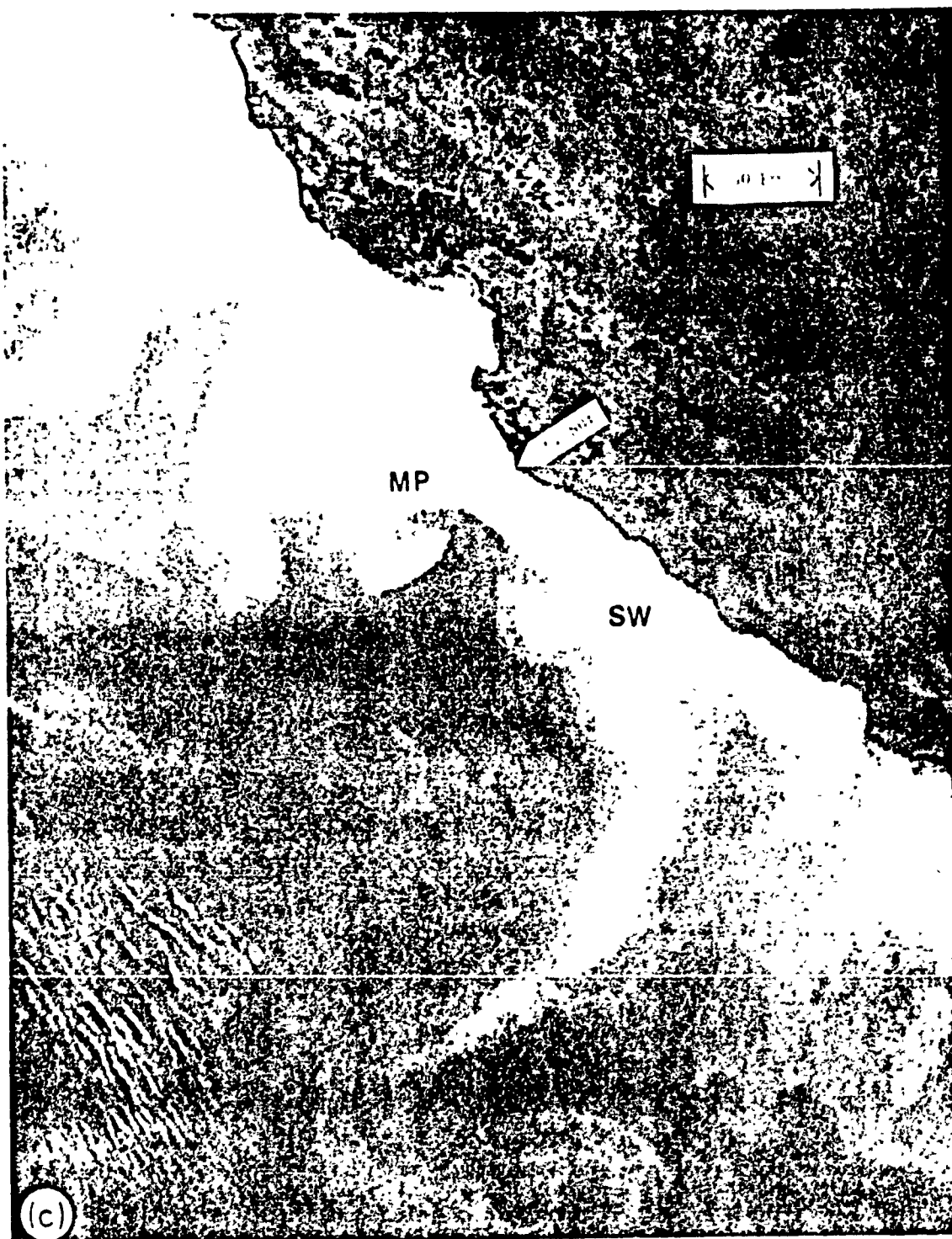


Fig. 15. Satellite (IR) images taken from the west coast of the U.S.A. (a) Taken on June 2, 1980, showing an upwelling maximum at Point Sur and the associated standing wave downstream. (b) Taken 38 days later on July 10, 1980, indicates that the standing plume at the ridge is unstable and has grown in the off-shore direction. Notice the cyclonic eddy which is about to be pinched-off from the head of the plume. The downstream standing wave is also unstable and its behavior is similar to that of the standing plume. (c) Taken in June 1981, again showing the standing features described in (b), only here the downstream standing wave probably interacted with an off-shore eddy to produce the indicated filament.



cape, but that the amplitudes of the features scales with the cape size. Again, when we introduced a smaller ridge than that of NM1 and Case A and B into the laboratory model we observed that the effects of small ridge on upwelling were again similar to that seen in those studies (Fig. 14), except here the standing features were of smaller amplitude. In Fig. 15 it can be





seen that Point Sur can produce an upwelling plume at the bottom topography and standing wave downstream as the model suggests.

In general, it appears from satellite (IR) images that consistent, large-amplitude standing features often exist downstream off major capes on the west coast of the U.S.A. Kelly (1985) has reported one of these standing features





Fig. 16. A satellite (IR) image from the west coast of the U.S.A. (taken in July 1980), shows the presence of two filaments (FI), one at Point Arena and the other at Point Conception at the position where, as predicted by the model, a diverging rotary type flow configuration should occur. Description of the features near Point Sur are as in Fig. 15.

downstream of Point Arena. Figures 8 and 10 show features similar to those reported by her downstream of Point Arena. These IR images show standing features downstream of Cape Blanco and Cape Mendocino also. As we have discussed in detail in NM4 (see also section 2), capes often produce a diverging, rotary-type motion between the cape and the first standing wave. Interaction between this rotary motion and the upwelled fluid produced long, thin filaments of cold water, which extended a considerable distance off-shore. Eventually, the filaments, as they drifted downstream, were absorbed by the large downstream standing wave, while at the same time new ones were formed by the rotary motion. Such filaments have often been observed near the major capes (see Fig. 16) off the west coast of the U.S.A.

The most abrupt coastline irregularity off the west coast of the U.S.A. occurs at Point Conception. Reports indicate (see section 2) that the average

equatorward summer, wind-stress upstream (north) and at Point Conception is large, while it is weak downstream (south) of this location. In order to investigate the effect of such wind stress distribution near an abrupt change in coastline shape during an upwelling episode, we produced a similar situation in the laboratory model (for details see section 2). A typical

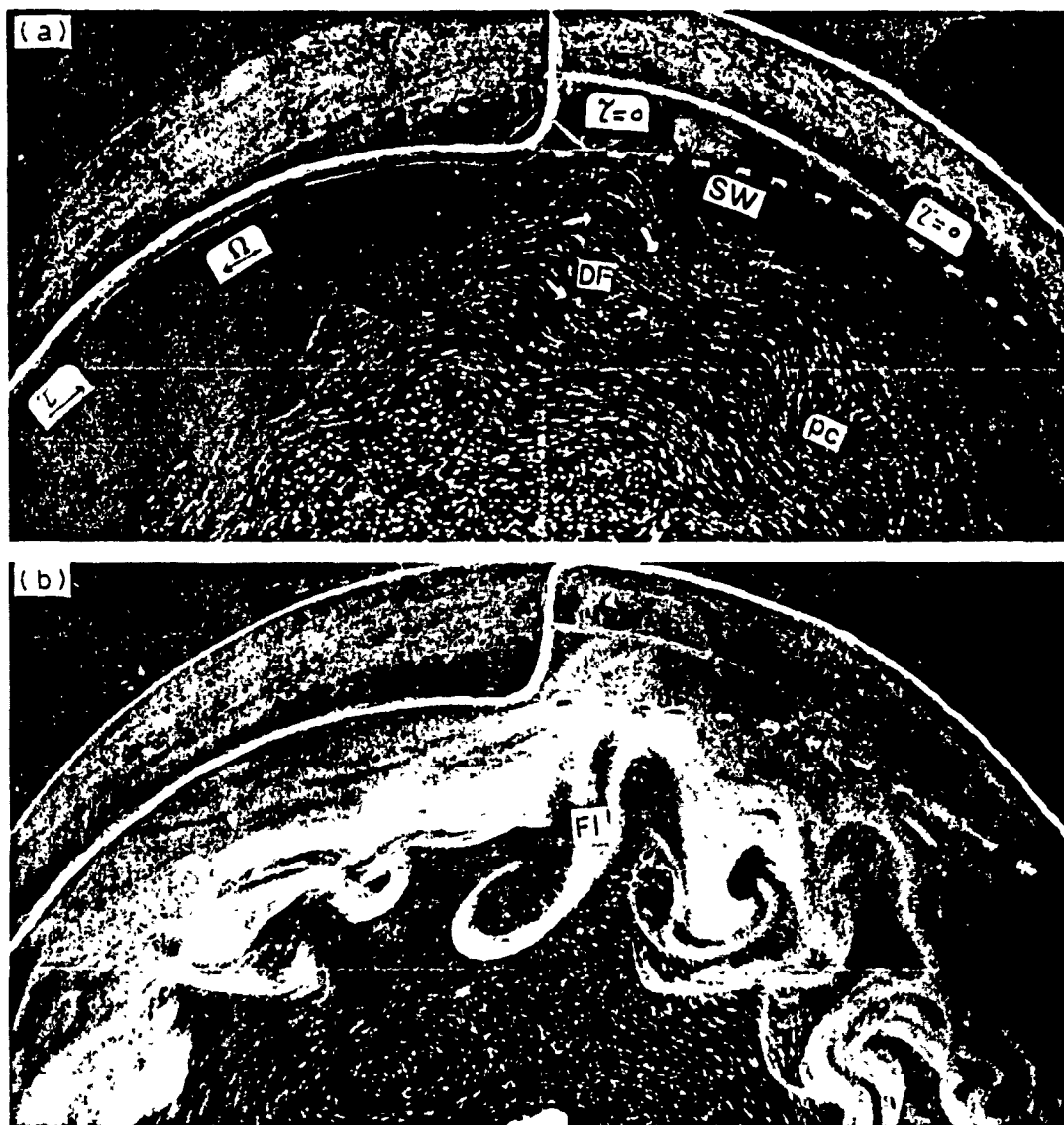


Fig. 17. Streak and dye photographs with 0.5 s time exposure, showing the flow pattern caused by the abrupt change in coastline shape. Experimental conditions are  $h_0 = 2.8$  cm,  $g' = 21$  cm s $^{-2}$ ,  $t = 4$  s,  $\Delta\Omega = 0.15$  s $^{-1}$ ,  $u_* = 0.33$  cm s $^{-1}$ ,  $\lambda_c \approx 15$  cm,  $\theta_* \approx 3$ . (a) Shows a diverging flow (DF) just downstream of the abrupt change. A standing wave and a pinched-off eddy are shown further downstream. Note that such a flow pattern is similar to that produced by a symmetric cape alone (see Fig. 7). (b) Dye is released into the system near the surface and is transported off-shore by the diverging flow, the standing wave and associated pinched-off eddies. Notice the formation of the indicated filament, which is produced by the diverging flow. Note that as the filament was convected downstream a new one formed in its place (for details see NM4).

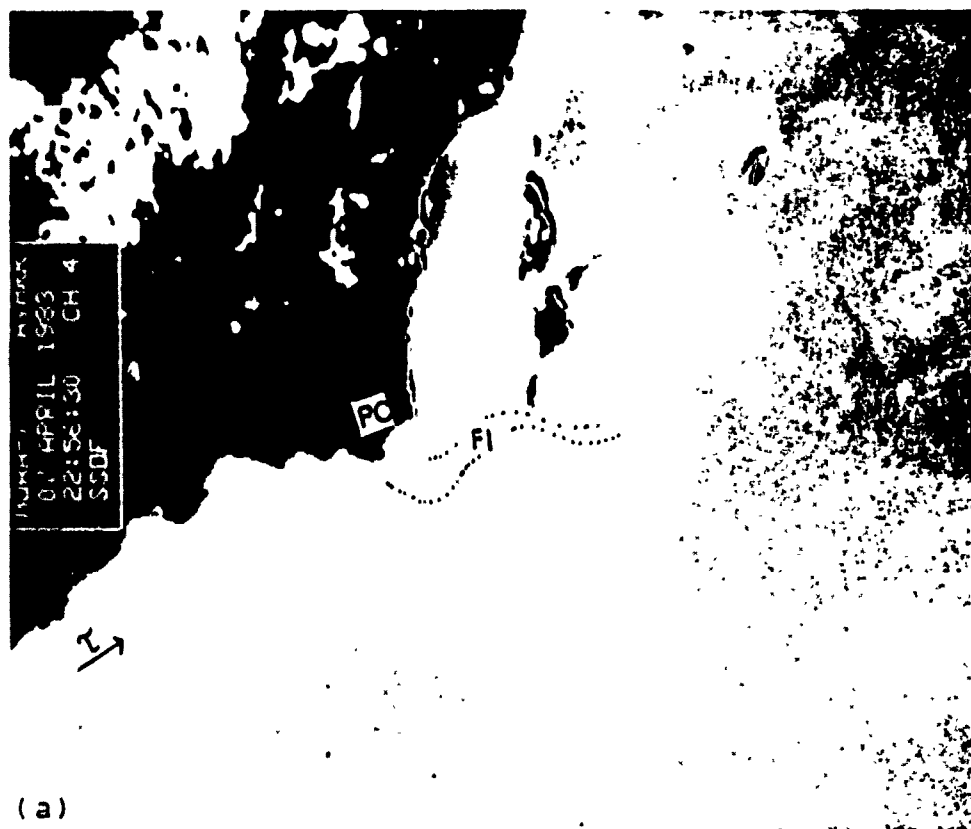


Fig. 18. Satellite (IR) images showing an upwelling system near Point Conception (courtesy of Burton Jones). (a) Taken on April 7, 1983 showing the presence of a filament near Point Conception at the position where a rotary-type flow configuration should occur. (b) Taken on May 16, 1983, showing a fully developed upwelling feature near Point Conception with characteristics similar to those described in Fig. 17.

experimental result is shown in Fig. 17. Characteristics of the flow caused by such a laboratory arrangement are similar to those produced by a cape alone except for the existence of a stagnant or separated zone immediately downstream of the cape. The flow divergence, the downstream standing

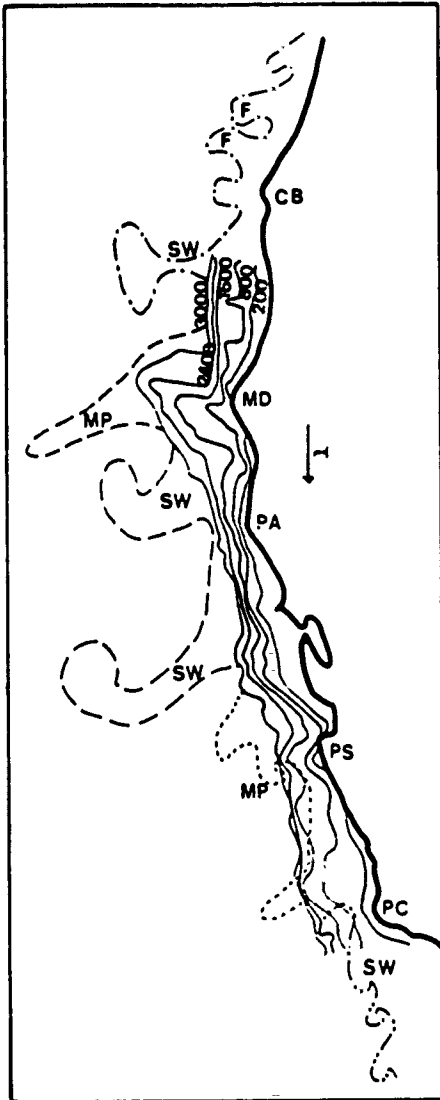


Fig. 19. Coastline variations ( — ) and contour map of bottom topography ( — ) off the west coast of the U.S.A. Superimposed are the interface between cold upwelled water and warmer surface water, drawn according to the satellite (IR) images of Fig. 9 (---), 10 (— — —), 15c (-----) and 18 (---). Descriptions of the upwelling features as in Figs. 8, 9, 10, 15 and 18, only here their relations with coastal perturbances are shown clearly. Owing to the presence of major capes and ridges to the south of Cape Blanco, the upwelled features are standing while the absence of major coastal perturbances to the north of Cape Blanco allow a uniform upwelled front and associated frontal eddies to develop. Notice that it is the Mendocino Ridge that produced the largest standing features and Point Sur which produced relatively small features. Since we have estimated a value of  $\theta^* \approx 5$  for the west coast of the U.S.A., all the standing features are probably unstable and will propagate in the off-shore direction.

wave and the pinched-off eddy are clearly shown in Fig. 17. When dye was released into the upwelled fluid upstream of the cape it was transported off-shore in a similar fashion to that already described for capes in NM4. This suggests that the large features seen in IR images near Point Conception are indeed induced by the presence of the Point itself (see Figs. 8, 16 and 18).

The discussion up to this point has been concerned with upwelling events to the south of Cape Blanco (Fig. 19). To the north of the cape the coast is free of major perturbations. According to the model, in such regions, standing features, as described above, should be absent, instead a uniform upwelled front and associated traveling frontal-eddies should develop. Satellite (IR) images, e.g., Figs. 9 and 20, and a recent publication by Thomson and Papadakis (1987), indeed indicate the presence of a uniform upwelled front with superimposed frontal, baroclinic eddies to the north of Cape Blanco.

In summary, to give a simple and clear overall picture of the upwelling system off the west coast of the U.S.A., we have superimposed four satellite (IR) images on to the contour map of bottom topography (see Fig. 19). The



Fig. 20. A satellite (IR) image taken in September 1982, showing an interaction between the coastally induced standing features and off-shore eddies. Induced turbulent jets associated with the off-shore eddy field have transported the coastal upwelled water far off-shore in the form of filaments. Notice that the interaction has revealed the presence of off-shore eddies.

four IR images taken together cover most of the important features of the upwelling system. Each image shows features that are repeated in a large number of images and can be considered typical of the region under study.

More recently we have studied the statistical properties of the field of frontal, baroclinic eddies and those which were pinched-off from the upwelling system. Measurements of the wavenumber energy spectrum indicated that such an eddy field is close to being two dimensional and geostrophic (Narimousa et al., 1987). The dispersion characteristics of such a field are closely associated with the high-speed, often turbulent, jets between vortices of like sign. A similar mechanism is often seen in the ocean, where these jets transport cold upwelled water far off-shore in the form of meandering filaments, as shown in Figs. 8 and 20 and see Fig. 22.

#### 4.1.2. Quantitative

In this section we apply quantitative results from our model for some of the characteristics of the upwelling system (see section 2) to the similar features seen in satellite (IR) images. In our applications of the model, we use the basic data gathered by Mooers et al. (1976), Hickey (1979), Breaker and Mooers (1986), and those already used in the numerical modeling of Peffley and O'Brien (1976), and Ikeda and Emery (1984) to calculate a value for the appropriate independent variable  $\theta^*$ . Thus, we choose  $h_0 \approx 50 \times 10^2$  cm,  $g' \approx 1.5$  cm s<sup>-2</sup>,  $f \approx 10^{-4}$  s<sup>-1</sup>,  $u^* = 1.5$  cm s<sup>-1</sup> (i.e.,  $\tau = 2$  dyn cm<sup>-2</sup>) and  $\lambda_s \approx 10^7$  cm. Note that in our original experiments we did not measure  $u^*$  directly, it was deduced from direct measurements of the mean velocity  $U$  in the upper layer (see NM1) using an empirical relation  $u^* \approx 0.1 U$ , given by Narimousa et al. (1986). Using the above data we estimate a value of  $\theta^* \approx 5$  for the west coast of the U.S.A.

Furthermore, for comparison of model and prototype we also need to estimate a value of the Rossby  $\beta$  number  $R_\beta = U/\beta a^2$  (here  $a$  is the width of the current,  $\beta = f/1/h \, dh/dr$ ,  $h$  is the average depth and  $\alpha = dh/dr$  is the bottom slope). For the laboratory model we have  $\alpha \approx 0.27$ ,  $a \approx 20$  cm,  $f \approx 3$  s<sup>-1</sup>,  $U \approx 4$  cm s<sup>-1</sup> and  $h \approx 10$  cm, giving an average value of  $R_\beta \approx 0.12$ . For the west coast of the U.S.A., we have  $\alpha \approx 0.05$ ,  $a \approx 6 \times 10^6$  cm and  $h \approx 15 \times 10^4$  cm, giving an average value of  $R_\beta \approx 0.1$ , which is about the same as that found in the laboratory model. This similarity between the field and the laboratory model allows us to apply the quantitative results of the model to field observations.

According to the model, baroclinic waves should appear at the upwelled front at an off-shore distance  $\lambda_i$  (see NM3) given by

$$\lambda_i/\lambda_s \approx 0.7\theta^*{}^{-0.5} \quad (1)$$

Application of eqn. (1) to the above field data gives a value of  $\lambda_i \approx 30$  km.

for the off-shore distance in which the waves should appear at the upwelled front. Figure 21 shows an early stage of the upwelled front at the surface between Point Sur and Point Conception, where the front has migrated a distance of  $\lambda \approx 35$  km, off-shore from the coast. Small baroclinic disturbances with a diameter,  $\lambda_w$  of  $\approx 15$  km, have already been formed at the front at about the distance predicted above by the model (Fig. 21). Observations from the laboratory model in the absence of any coastal perturbations (NM3) demonstrated that the upwelled front should continue to migrate off-shore and at the same time the frontal baroclinic waves should continue to grow in amplitude. Eventually, a steady-state situation is reached and the radial pressure gradient caused by front deformation balances the radial Coriolis force beneath the ageostrophic surface Ekman layer, the upwelling



Fig. 21. A satellite (IR) image taken in April 1981, showing an early stage of upwelling between Point Sur (PS) and Point Conception (PC). The upwelled front has migrated a distance of  $\sim 35$  km off-shore, where baroclinic disturbances with a mean diameter of  $\sim 15$  km have appeared at the front. An incipient upwelling maximum at Point Sur is also clearly shown.



Fig. 22. A satellite (IR) image from the west coast of the U.S.A. showing that the standing features associated with major coastal perturbations dominate the upwelling system to the south of Cape Blanco, as in Figs. 9, 10 and 23. To the north of Cape Blanco a nearly uniform upwelled front and frontal baroclinic eddies are apparent. Some of the characteristics of the coastal upwelling ( $\lambda_w$ ,  $D_{sw}$ ,  $A_{sw}$ ,  $\lambda_o$ ) are indicated. Off-shore eddies and associated turbulent jets, as indicated, are revealed also. In this IR image, the standing features are unstable and have grown in the off-shore direction.

front becomes stationary and the frontal waves reach a saturated size given by eqn. (2). In the real ocean the situation is not always as clean-cut as this since the upwelling front, during its migration and before reaching its final location, often interacts with the off-shore eddies and thereafter the eddies transport the upwelled water off-shore as described in section 4.1.1. Also, coastal perturbation as demonstrated in the laboratory and repeatedly seen in IR images, produce large, off-shore-extending standing features (see sections 3 and 4.1.1) which tend to dominate the upwelling system (Fig. 22). Such influences in the actual ocean greatly reduce the chance for formation of a fully developed, uniform upwelled front and the associated frontal eddies. The satellite (IR) image, Fig. 21, shows an early stage of upwelled front at the surface in a region (between PS and PC) where major coastal perturbations are absent. Even in such a region, the indicated uniform upwelled front will not last for very long and it will soon lose its identity due to the above-mentioned mechanisms. For example, Breaker (1985) included a sequence of IR images (taken on June 1981 between PS and PC) showing an early stage of the upwelled front which had lost its form mostly due to interaction with the off-shore disturbances.



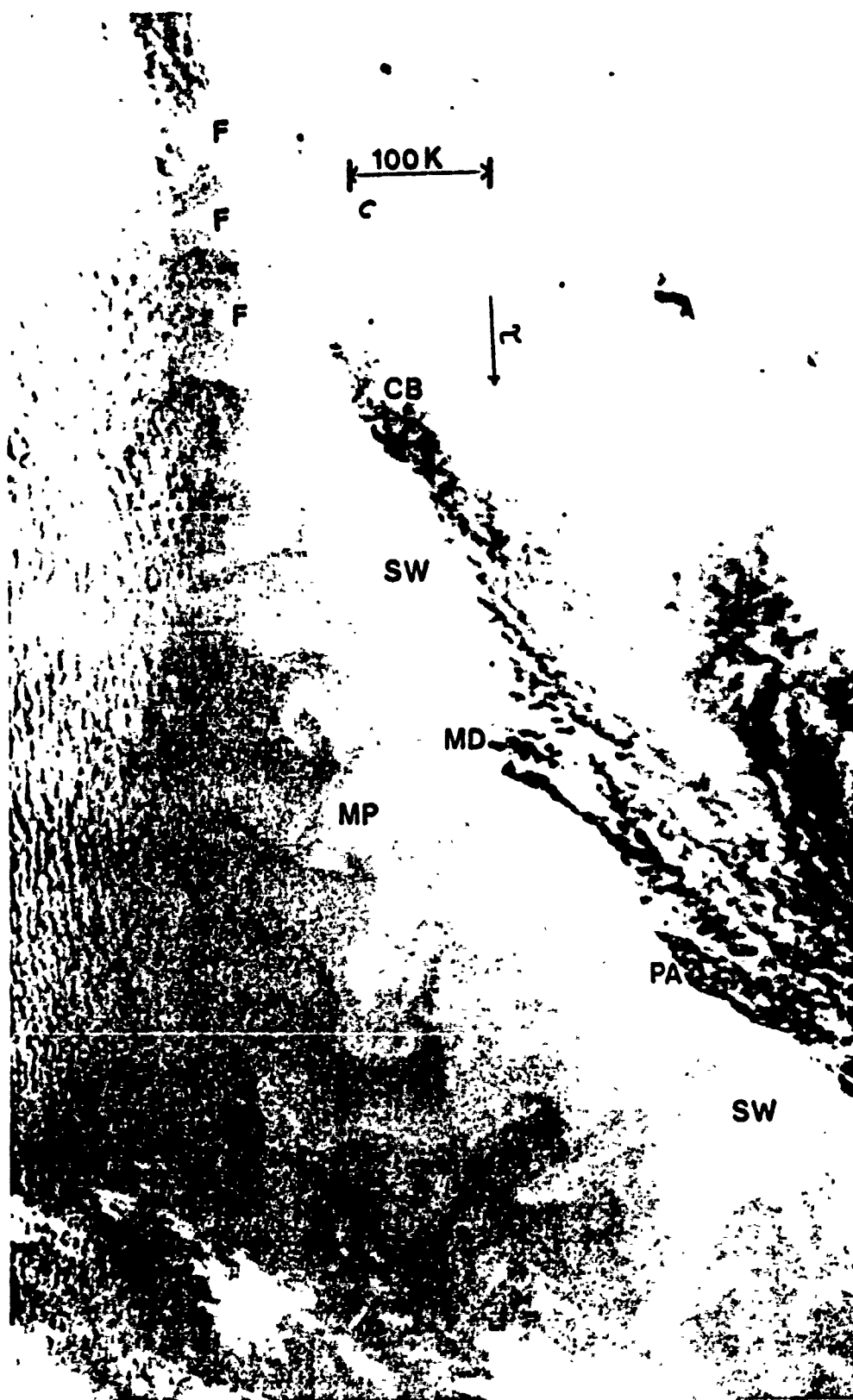


Fig. 23. A satellite (IR) image from the west coast of the U.S.A. showing the standing features to the south of Cape Blanco and a uniform upwelled front with associated frontal eddies to the north of Cape Blanco. The frontal eddies have a wavelength  $L_w \approx 2\lambda_w \approx 100$  km, and the uniform upwelled front has a width  $\lambda_w \approx 100$  km. In this image the uniform upwelled front is far enough from the coast to allow the frontal eddies to pass Cape Blanco without being seriously distorted.

Measurements of the average diameter of the frontal eddies ( $\lambda_w$ ) in the laboratory (NM1) yields

$$\lambda_w/\lambda_s \approx 0.1\theta^* \quad (2)$$

This result was in agreement with wavelengths  $L_w = 2\lambda_w$  measured in experiments of Griffiths and Linden (1982) and Chia et al. (1982), and predicted by theories of Killworth et al. (1984) and Phillips (1954). Application of eqn. (2) to the above field data gives  $L_w = 2\lambda_w \approx 100$  km, which is in excellent agreement with the wavelengths measured from the satellite (IR) images near and upstream of Cape Blanco (e.g., Figs. 9, 22 and 23).

In NM3 (see also section 3) when we introduced a positive off-shore curl in the surface stress, a field of off-shore eddies was produced with average diameter ( $\lambda_o$ )

$$\lambda_o/\lambda_s \approx 0.22\theta^* \quad (3)$$

Applications of eqn. (3) to the above field data gives  $\lambda_o \approx 110$  km. Huyer et al. [1983] reported an off-shored eddy with a diameter of  $\sim 100$  km off the coast of Oregon. Bernstein et al. [1977] also reported an off-shore eddy with a size of  $\sim 100$  km upstream of Point Conception. Measurements of  $\lambda_o$  from IR images, Figs. 20 and 23, give an average value of  $\sim 100$  km, which is in agreement with that predicted by eqn. (3).

In NM4 (also section 3) we demonstrated that capes usually produced stable downstream standing waves. Only at values of  $\theta^* < 6$ , and after about 50  $f$ , did the standing waves often become unstable and their amplitude grow in the off-shore direction. Measurements of amplitude of the stable standing waves  $A_{sw}$  for all values of  $\theta^*$  yields

$$A_{sw}/R_c \approx 3.5 \quad (4)$$

where  $R_c$  is the mean radius of a given cape measured from a mean coastline. Here we apply eqn. (4) to major capes like Blanco and Point Arena. For capes Blanco and Point Arena we have  $R_c \approx 25$  km, giving  $A_{sw} \approx 90$  km. These values of  $A_{sw}$  for the above capes are estimated for when the standing waves are stable. We should emphasize here that since we have estimated a value  $\theta^* \approx 5$  for the west coast of the U.S.A., then according to the model the standing waves caused by the capes should become unstable and their amplitude should grow in the off-shore direction. The growing wave will eventually allow a cyclonic eddy to be pinched-off from its trough. Under such circumstances, the maximum value of  $A_{sw}$  for the unstable wave, before total detachment of the cyclonic eddy, is about twice that given above by eqn. (4) for the case when the wave is stable (see Fig. 19).

Also, we have measured the distance  $D_{sw}$  between the tip of a given cape and the center of the generated downstream standing wave. The result was consistent with (see NM4)

$$D_{sw}/R_c \approx 2\theta *^{0.4} (\lambda_s/R_c)^{0.2} \quad (5)$$

which is applicable to any cape. Application of eqn. (5) to the above capes gives  $D_{sw} \approx 125$  km. for the distance of the downstream standing wave from Cape Blanco and Point Arena. Average values of  $D_{sw}$  measured from satellite (IR) images for the above capes are in agreement with that predicted by eqn. (5).

For the purpose of the present study, as mentioned in section 2, we performed experiments where we placed a variety of ridges (different widths, height and shapes) into the experiment tank. Measurements of the distance between the mean position of the generated downstream standing wave and the ridge  $D_{sw}$ , for 35 different cases and to within an error of  $\sim 10\%$ , was consistent with

$$D_{sw}/\lambda_s \approx 0.3((wh_r)^{0.5}/H)^{-0.25} \theta * \quad (6)$$

where  $w$  is the average width of the ridge,  $h_r$  is the average height of the ridge and  $H$  is the average depth of the water column adjacent to the ridge. Equation (6) is applicable to any ridge which is nearly symmetric. Owing to this, it is difficult to apply eqn. (6) to Mendocino Ridge because it is highly non-symmetric. Difficulty also arises in estimating a value of  $w$  for Mendocino Ridge from an actual contour map of bottom topography off the west coast of the U.S.A. Nevertheless, from the much simplified contour map, Fig. 19, one can estimate a value of  $w \approx 70$  km for the average width of the Mendocino Ridge with  $h_r \approx 1$  km and  $H \approx 2$  km. Application of eqn. (6) to this case gives a value of about  $D_{sw} \approx 105$  km. for the distance of the downstream standing wave from the ridge. Satellite (IR) images presented in this paper give  $110 \leq D_{sw} \leq 150$  km for the standing wave associated with Mendocino, which has a lower bound in agreement with that predicted by the model. However, experiments with the non-symmetric ridges give larger values for  $D_{sw}$  owing to the slower relaxation to the upstream depth, downstream of the non-symmetric ridge.

Applications of eqn. (6) to the ridge at Point Sur with  $h_r \approx 0.5$  km,  $w \approx 40$  km and  $H \approx 1$  km, gives  $D_{sw} \approx 100$  km. for the distance of the downstream standing wave from the ridge.

Measurements of the amplitude of the stable downstream standing wave caused by ridges in the laboratory was consistent with

$$A_{sw} \approx 1.2(h_r/H)^{-1/3} W \quad (7)$$

Application of eqn (7) to Mendocino Ridge gives a value of  $A_{sw} \approx 105$  km, and to the ridge at Point Sur, gives a value of  $A_{sw} \approx 60$  km.

The other important parameter measured in the laboratory was the amplitude of the stable standing wave or plume  $A_{sp}$ , which formed over the ridge itself. Measurement of  $A_{sp}$  in the laboratory was consistent with

$$A_{sp}/\lambda_s = 1.5(h_i/H)^{0.25}(\theta^*)^{1/3} \quad (8)$$

Application of eqn. (8) to Mendocino Ridge gives a value of  $A_{sp} \approx 215$  km.

We should emphasize here that eqn. (8) was obtained for ridges which extend very far off-shore, like Mendocino Ridge which extends over 200 km off-shore. Under these circumstances, the standing plume has the opportunity to develop fully. Since Point Sur extends a short distance, about 80 km, off-shore, then the amplitude of the induced plume should be confined to values around 80 km, unless the plume is unstable. Then, as far as the value of  $A_{sp}$  is concerned, relationship (8) is probably not applicable to short ridges like that at Point Sur.

#### *4.2. To the west coast of Baja California, Mexico*

##### *4.2.1. Qualitative*

The Pacific coast of Baja California is among the regions where intense coastal upwelling has been reported by field and satellite observations (see Fig. 24). Coastline irregularity off Baja consists of two major capes. One occurs at Point Eugenia (PE) centered approximately at  $27^\circ$ S and the other occurs at Cape San Lazaro (SL) near  $25^\circ$ S. Point Eugenia, with its awkward shape, is the largest of all the capes mentioned in this study and its effect on upwelling should be substantial. Cape San Lazaro is about half the size of Point Eugenia, yet it is larger than those discussed above. As a result, one would suspect that it should have a significant effect on coastal upwelling also. Contour maps of bottom topography (Fig. 25) shows no major off-shore ridge extending from either of the indicated large capes. However, there does exist an along-shore ridge near  $29^\circ$ S which is parallel to the mean flow and is so shallow that it probably acts to enhance the effect of Point Eugenia, making it appear bigger to the flow than it appears on the map.

In order to investigate the effects of such coastline irregularities on the upwelling system we have produced a nearly similar situation in the laboratory model. Three capes of small, large and medium size, respectively, were introduced at the wall of the tank as shown in Fig. 26. A typical flow pattern and frontal behavior are shown in Fig. 26. Here the front, which is identified by the off-shore limit of the particle streaks, was far from the small cape so that the associated induced features caused by the cape were buried within



Fig. 24. A satellite (IR) image taken in May 1979, from the west coast of Baja California, off the west coast of Mexico (courtesy of NASA). There are at least four large off-shore-extending standing features on this IR image. The model suggests that these features are associated with the large coastline perturbances off Baja (see Fig. 26). Also notice the indicated filaments.

the upwelled water. That is, the upwelled front was almost undisturbed by the small cape. At the same time the large and medium capes have strongly influenced the upwelling front and each has produced the types of standing feature already discussed in NM4 and the previous sections for a single cape. As shown on Fig. 26 the large and the medium cape have each caused

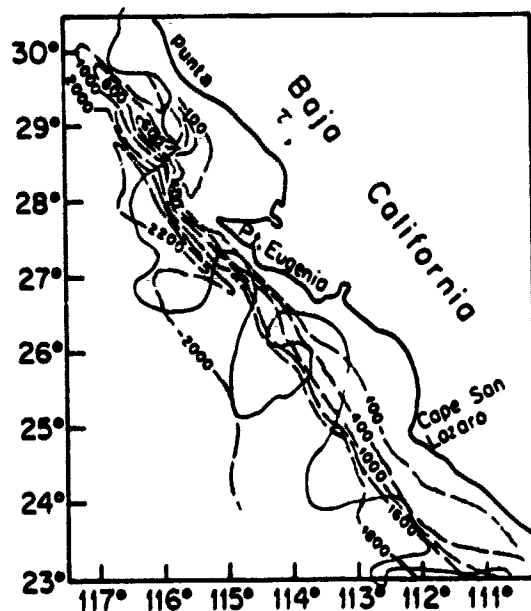


Fig. 25. Coastline variations ( — ) and contour map of bottom topography ( — — ) off Pacific coast of Baja. Superimposed ( — — — ) is the interface between cold upwelled water and warmer surface water drawn according to the IR image, Fig. 24. Descriptions of the upwelling features are as in Fig. 24, only here their relations with coastal perturbances are shown clearly.

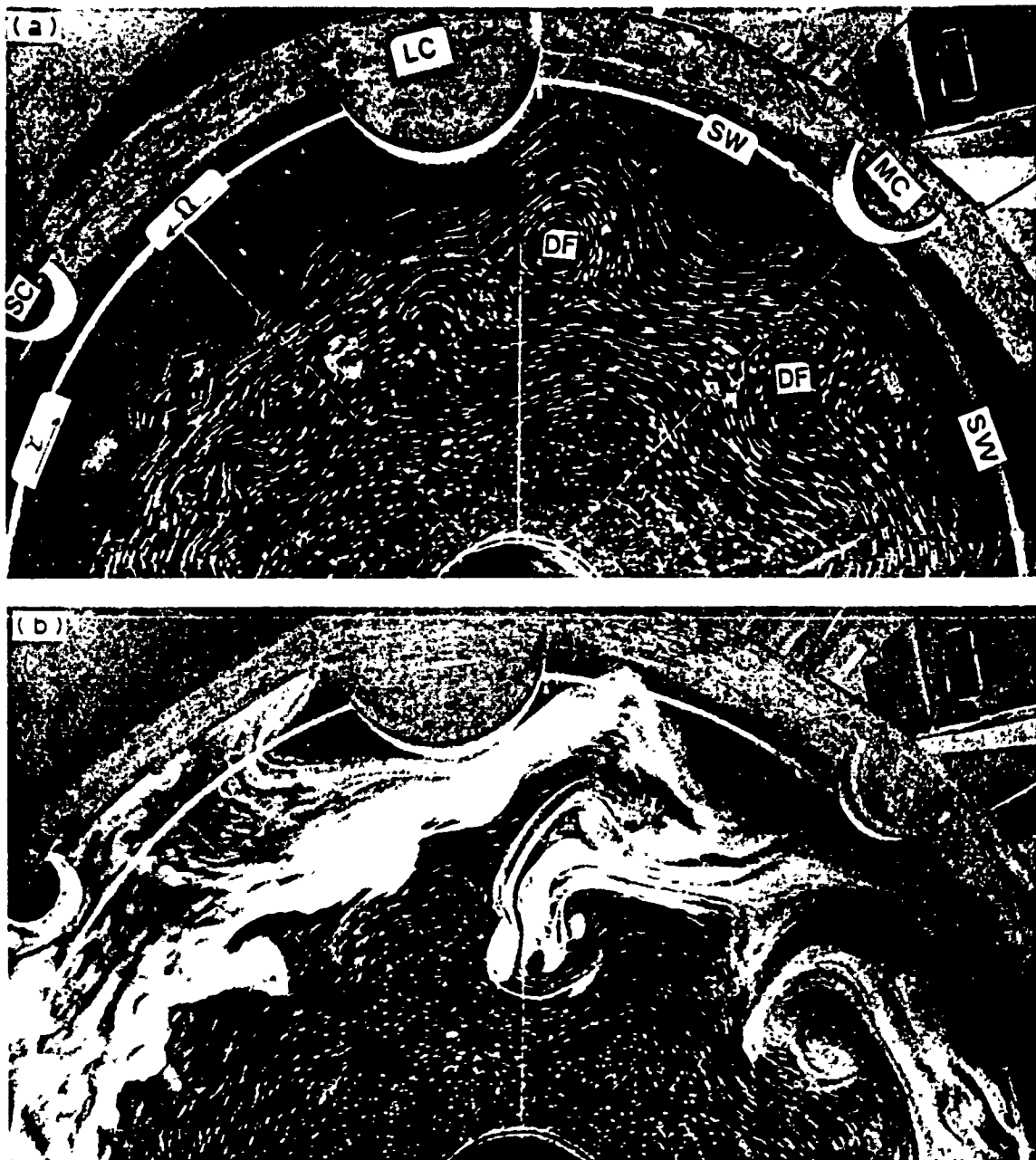


Fig. 26. Streak and dye photographs with a 0.5 s time exposure, showing interaction of the upwelling system with small (SC), large (LC) and medium (MC) capes, respectively. Experimental conditions are:  $h_0 = 2.5$  cm,  $g' = 27$  cm s<sup>-2</sup>,  $f = 4.1$  s<sup>-1</sup>,  $\Delta\Omega = 0.16$  s<sup>-1</sup>,  $u_* \approx 13.5$  cm s<sup>-1</sup> and  $\theta_* \approx 4$  (a) Rotary type of diverging flow pattern and downstream standing wave associated with the large and medium capes are indicated. The small cape should also produce similar features, but since the upwell front is far from it, they are not shown by the streaks. (b) When dye was released into the system near the surface it was transported off-shore abruptly by the diverging flow and the standing wave of the large and medium capes. Upstream baroclinic frontal waves passed the small cape undisturbed.

a large downstream standing wave and a rotary diverging-flow configuration between the cape and the indicated standing wave. These standing features, which were clearly associated with the capes, played a significant role in the

off-shore transportation of coastal upwelled water. To demonstrate this, we released dye into the upwelled water near the surface. When it reached the indicated standing features, it was abruptly transported off-shore, as shown on Fig. 26.

Application of the laboratory observation to the flows shown in Figs. 24 and 25 suggests that the large disturbance at Cape San Lazaro is really part of the standing wave regime generated by the larger cape at Point Eugenia. This possibility is suggested by the earlier observation that capes do not produce upwelling maximum, nor a standing wave, over the cape itself. When a standing wave (upwelling maximum) is observed at a cape, as in this case and at Point Arena, the wave must almost certainly be associated mainly with the presence of the upstream perturbation. The upstream perturbation, in the case of Point Arena, is the Mendocino Ridge (see section 4.1), and in the case of Cape San Lazaro, as mentioned above, it is Point Eugenia. The satellite image, Fig. 24, shows a large off-shore extending feature near  $26^{\circ}\text{S}$ , between Point Eugenia and the associated standing wave at Cape San Lazaro. According to the laboratory model a diverging rotary-type flow should occur at this location. In NM4 we showed that such flow configuration produced long, off-shore-extending filaments of the upwelled water, and in Fig. 26 we saw that a large quantity of the upwelled water was transported off-shore by the induced flow. The observed feature

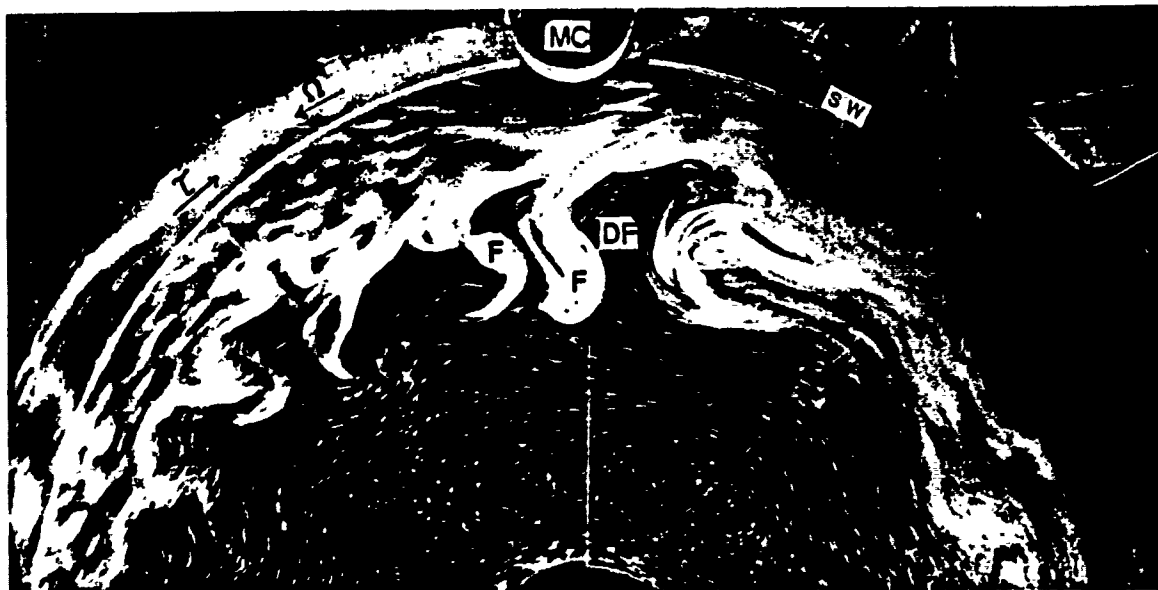


Fig. 27. Streak and dye photographs with a 0.5 s time exposure and a value of  $\theta \approx 3$  of flow past a cape. Notice the frontal baroclinic eddy which has been deformed and pulled off-shore upon reaching the location of the diverging flow. The upwelled water within the wave will eventually become a thin filament as shown in detail in NM4. Also, notice the downstream standing wave, where a large quantity of upwelled water is forced off-shore.

near  $26^{\circ}\text{S}$  consists of a filament similar to that observed in NM4, and a large quantity of mixed upwelled water, as in Fig. 26.

The IR image, Fig. 24, shows the presence of yet another standing wave downstream of Cape San Lazaro, as predicted by the laboratory model. The upwelled water within the standing wave is transported off-shore by the diverging flow to produce filaments similar to those shown downstream of the medium cape (Fig. 26) in the laboratory and that shown on the IR image (Fig. 24) downstream of Cape San Lazaro.

A small cape exists upstream of Point Eugenia near  $29^{\circ}30'\text{S}$  (PB), about half the size of San Lazaro. This small cape, as shown on the IR image, Fig. 24, has produced features similar to the ones described above. There are two baroclinic waves, one upstream and one just past the small cape. The one which passed the cape is deformed by the induced diverging flow similar to that observed in the laboratory (Fig. 27). The downstream standing wave associated with the small cape is shown just downstream of the deformed baroclinic wave, which is consistent with that in Fig. 27.

As mentioned above, the bottom topography near  $29^{\circ}\text{S}$  consists of a ridge which runs parallel to the coastline in the direction of Point Eugenia. This ridge should produce a cyclonic circulation over the ridge similar to the one described for an off-shore extending ridge. The presence of the ridge should produce downstream standing waves also. The IR image, Fig. 24, shows the presence of a standing wave near the tip of Point Eugenia, which we believe is induced by the indicated upstream ridge. Although Fig. 24 does not reveal the presence of the cyclonic circulation over the ridge, field measurements have indicated the presence of a strong cyclonic circulation at that location over the ridge, during an upwelling event (Bernstein et al., 1977; Hickey, 1979).

#### 4.2.2. Quantitative

In quantitative application of the laboratory model to upwelling events measured from the satellite image, Fig. 24, we use the data reported by Hickey (1979) and Morales et al. (1978) to estimate  $h_0 = 5 \times 10^{-3}$  cm,  $g' = 1.2$  cm  $\text{s}^{-2}$ ,  $U = 20$  cm  $\text{s}^{-1}$ ,  $f = 0.6 \times 10^{-4} \text{s}^{-1}$ ,  $\lambda_c \approx 100$  km and  $\theta^* \approx 5$ .

Application of eqn. (5) to capes at Punta Baja, Point Eugenia and Cape San Lazaro with  $R_c \approx 22, 80$  and  $40$  km gives  $D_{sw} \approx 110, 315$  and  $180$  km, for the distance of the downstream standing wave from the mean position of the indicated capes, respectively. Measurements from the satellite (IR) image, Fig. 24, gives  $D_{sw} \approx 110, 320$  and  $170$  km for above capes, respectively, which are in agreement with those predicted by the model.

Application of eqn. (4) to the amplitude of the stable standing wave downstream of the above-mentioned capes gives  $A_{sw} \approx 77, 280$  and  $140$  km.



respectively. Measurements from Fig. 24 give  $A_w \approx 70, 260$  and  $150$  km for the above capes, respectively, which are in agreement with that predicted by the model.

#### 4.3. To the west coast of Peru

The coast of Peru is another region where active coastal upwelling has been recorded. The coast is free of major coastline perturbations and the contour map of bottom topography indicates the presence of two ridges between  $15^\circ\text{S}$  and  $15^\circ 30'\text{S}$ . The larger ridge occurs near  $15^\circ 30'\text{S}$  and the much smaller one occurs near  $15^\circ 15'\text{S}$  (Fig. 28). Because the two ridges are very close to each other, the larger ridge should dominate and initiate the type of standing features discussed in detail in previous sections. However, the larger ridge is actually quite small, since it is about half the size of that of Point Sur. The much smaller ridge near  $15^\circ 15'\text{S}$ , which extends  $\sim 15$  km off-shore, should have only a local effect on the upwelling system, but as shown in Fig. 28, its small effect would be buried by the large-scale standing wave caused by the larger ridge.

At this time we are unaware of the existence of any satellite (IR) images for the upwelling system off the coast of Peru. This of course makes it difficult for us to make extensive comparison between the results of our laboratory model and upwelling events off Peru. Since we have the information about bottom topography and coastline variation, we should be able to predict the general form of the upwelling system off Peru. As observed in the laboratory, the larger ridge should produce an upwelling maximum at

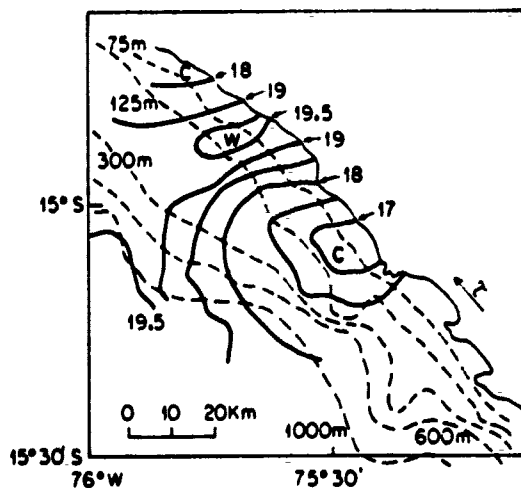


Fig. 28. Contour map of bottom topography off the west coast of Peru. Superimposed is the sea-surface temperature for upwelling structures as recorded by Brink et al. (1979). Notice the presence of a well-developed standing wave downstream of the larger ridge. There is also a second standing wave downstream of the first, but only a small part of it has been recorded.

the ridge and at least one large standing wave downstream. Sea-surface temperature measurements reported by Brink et al. (1981) indicate the existence of a well-developed standing wave at a distance of  $\sim 50$  km. downstream of the ridge, i.e.,  $15^{\circ}10'S$ , which is consistent with observations in the laboratory. Their temperature measurements indicate the presence of a weaker, second, downstream standing wave at a distance of  $\sim 100$  km from the ridge, i.e., at  $14^{\circ}30'S$ , which is consistent with laboratory observation also. Although measurements of Brink et al. (1981) did not cover the ridge itself, a standing wave or upwelling maximum should form over the ridge, just as observed in the laboratory. Further downstream of these standing features, the absence of major coastal perturbations should allow a uniform upwelled front with associated frontal eddies to develop. A similar situation, that is the formation of a uniform upwelled front, should also occur upstream of the main ridge.

Considering the data reported by Brink et al. (1980, 1981) and Guillen and Galienes (1981), Maxworthy and Narimousa (1985) estimated  $u^* \approx 1$   $\text{cm s}^{-1}$ ,  $h_0 \approx 18$  m,  $g' \approx 0.6$   $\text{cm s}^{-2}$ ,  $f = 0.4 \times 10^{-4}$ ,  $\text{s}^{-1}$ ,  $\lambda_s \approx 50$  km and  $\theta^* \approx 5.4$ . Applications of eqn. (6) to the ridge near  $15^{\circ}30'S$ , with  $w \approx 20$  km,  $h_r \approx 0.25$  and  $H \approx 1$  km, gives  $D_{sw} \approx 55$  km for the distance of the mean position of the first downstream standing wave from the indicated ridge off Peru. The laboratory model predicts the formation of a second downstream standing wave at a distance of  $\sim 110$  km from the ridge near  $15^{\circ}30'S$ . These estimates are in agreement with the field measurements (see Fig. 28) reported by Brink et al. (1981).

Applications of eqn. (5) to the above ridge gives  $A_{sw} \approx 30$  km for the amplitude of the first downstream standing wave. On Fig. 28 the wave amplitude to the  $18^{\circ}\text{C}$  isotherm is  $\sim 30$  km.

## 5. SUMMARY AND CONCLUSIONS

Application of the characteristics of coastal upwelling, either observed or measured in the laboratory, to similar events off the west coast of the U.S.A., Peru and Mexico have revealed the following:

(1) In general, bottom topography (a ridge) produces standing off-shore intrusions or waves at the ridge and downstream. Capes do not produce an upwelling maximum at the cape itself, but, they do produce downstream standing waves. Upwelling maxima observed at capes are not caused by the capes themselves, they are associated with an upstream perturbation. For example, upwelling centers observed at Point Arena (U.S.A.) and Cape San Lazaro (Baja) are most likely the standing wave associated with Mendocino and Point Eugenia, respectively. Capes produce a diverging, rotary type of flow configuration between the cape and downstream standing wave. This

flow configuration produces off-shore extending filaments. In general, coastal perturbations produce standing features which tend to dominate the upwelling system. When major coastal perturbations are absent, the standing features are absent too, instead a uniform upwelled front with associated baroclinic eddies should appear at the sea surface. At values of  $\theta^* < 6$ , the baroclinic eddies should grow to such an amplitude that they allow cyclones to pinch-off from the front to form propagating cyclonic gyres. Collections of pinched-off eddies from the upwelling system, together with those at the upwelled front and those that pre-existed off-shore should produce a field of geostrophic or two-dimensional turbulence. Turbulent jets associated with such eddy fields are mainly responsible for transportation of the coastal upwelling off-shore, in the form of filaments seen in the laboratory and satellite (IR) images.

(2) The west coast of the U.S.A. starting from Cape Blanco and proceeding southwards, consists of many capes and ridges. The largest ridge occurs at Mendocino and this plays an important role in the initiation of standing waves at the ridge and downstream. At values of  $\theta^* \approx 5$  the intrusions caused by the Mendocino Ridge eventually become unstable and allow cyclonic eddies to pinch-off from their heads and propagate off-shore and downstream. Smaller ridges like that at Point Sur should initiate intrusions similar to that produced by Mendocino Ridge, but relatively smaller, as seen repeatedly on IR images and measured in the laboratory model. Cape Blanco and Point Arena should produce downstream standing waves, which at values of  $\theta^* \approx 5$  should eventually become unstable to allow cyclonic eddies to pinch-off from their troughs, as shown on different IR images. The standing waves associated with these coastal perturbations tend to dominate the upwelling system to the south of Cape Blanco. The absence of major capes and ridges to the north of Cape Blanco should allow formation of a uniform off-shore migrating upwelled front and associated frontal eddies. The satellite (IR) images which show the upwelling events to the north of Cape Blanco do, in fact, display the presence of a uniform upwelled front and associated frontal eddies. At values of  $\theta^* \approx 5$ , which are typical of the upwelling regime in this area, the uniform upwelled front upstream of Cape Blanco should become unstable to allow cyclonic eddies to pinch-off from the upwelled front. Turbulent jets associated with the pinched-off eddies from the upwelling system and the interaction with the California current system should transport coastal water far off-shore in the form of filaments as observed in the laboratory and seen on a variety of IR images. From quantitative applications of the relations found in the laboratory to upwelling events off the west coast of the U.S.A., we estimate  $L_w \approx \lambda_w = 100$  km, for the wavelength of frontal eddies at the upwelled front upstream of Cape Blanco, and a value of  $\lambda_o \approx 110$  km for the mean diameter of the off-shore

TABLE I

Comparison of estimated and measured values of upwelling characteristics. In each row the top data are produced by the model and the bottom data are averaged over the values measured from IR images presented in this paper (lengths are in km). For abbreviations CB, MD, PC and PS, see Figs. 8 and 9

	CB	MD	PC	PS
$A_{sw}$	87	105	87	65
	80	100	80	55
$D_{sw}$	105	110	105	90
	100	125	100	90
$A_{sp}$		215		
		200		

eddies off the west coast of the U.S.A., both are in agreement with those measured from satellite (IR) images. Table I shows a summary of the comparisons between the model and the field for different capes and ridges off the west coast of the U.S.A.

(3) A model of Point conception gives a flow field which has much in common with that observed in satellite images, including a relatively stagnant region downstream of the cape, a field with energetic eddying motion and with a complex frontal structure separating the stagnant zone from the region further off-shore.

(4) The contour map of bottom topography off the Pacific coast of Baja, California indicates the presence of a ridge centered at  $\sim 29^\circ\text{S}$ , which runs parallel to the coast. This ridge should produce cyclonic circulation above it and standing waves downstream. There are three major capes off Baja, a small one near  $29^\circ 30'\text{S}$  at Punta Baja (PB), a very large one centered at  $\sim 27^\circ\text{S}$  at Point Eugenia (PE) and the one near  $25^\circ\text{S}$  (San Lazaro (SL)) with a size about half that of Point Eugenia. Since the value of  $\theta^*$  is approximately 5.4 and the capes are well separated, then a diverging, rotary-type flow configuration and the associated downstream standing wave should be formed distinguishably by each cape. A detailed comparison (section 4.2) of observations in the laboratory and the features seen on the satellite (IR) image, Fig. 24, indicated that the features seen on the IR image resemble those observed in the laboratory. Table II shows a summary of the comparisons between the model and the field for different capes off Baja California.

(5) The major coastal perturbation off the coast of Peru occurs in the form of a ridge near  $15^\circ 30'\text{S}$ , while the rest of the coast is free of major disturbances. Because of this, a uniform upwelled front should occur up-

TABLE II

Comparison of estimated and measured values of upwelling characteristics. In each row the top data are produced by the model and the bottom data are averaged over the values measured from IR images presented in this paper (lengths are in km). For abbreviations of PB, PE and SL, see text

	PB	PE	SL
$A_{sw}$	77	280	140
	70	250	125
$D_{sw}$	110	315	180
	120	330	165

stream of the indicated ridge. At the ridge and some distance downstream, associated standing features should form. Downstream from these standing waves, again a uniform upwelled front should occur. The field measurements of Brink et al. (1981), indicated the presence of the standing waves downstream of the above ridge, at distances (55 and 110 km) as predicted by the laboratory model. It would be of interest to see if a major upwelling center is associated with the ridge itself since existing field observations have not yet explored this region.

#### ACKNOWLEDGEMENTS

The authors wish to thank Dr Lawrence C. Breaker of Naval Post Graduate School, Department of Oceanography, who kindly supplied us with all of the satellite (IR) images presented in this paper (unless otherwise mentioned) and Mrs. Jacqueline Givens for her expertise in typing the manuscript. Financial support was from the Office of Naval Research under Grant No. N00014-87-K-0809.

#### REFERENCES

- Batchelor, C.K., 1969. Computation of the energy spectrum in homogeneous two-dimensional turbulence. High-speed computing in fluid dynamics. Phys. Fluids Suppl., II: 233-239.
- Bernstein, R.L., Breaker, L. and Whrtner, R., 1977. California current eddy formation: ship, air and satellite results. Science, 195: 353-359.
- Breaker, L.C., 1985. The Space-time Scales of Variability in Oceanic Thermal Structure off the Central California Coast. Ph.D. Thesis, Naval Post Graduate School.
- Breaker, L.C. and Mooers, C.N.K., 1986. Oceanic variability off the central California coast. Prog. Oceanogr., 17: 61-135.
- Brink, K.H., Halpern, D. and Smith, R.L., 1980. Circulation in the Peruvian upwelling system near 15°S. J. Geophys. Res., 85: 4036-4048.

- Brink, K.H., Jones, B.H., Van Leer, J.C., Mooers, C.N.K., Stuart, D.W., Stevenson, M.R., Dugdale, R.C. and Heburn, G.W., 1981. Physical biological structure and variability in an upwelling center off Peru near  $15^{\circ}\text{S}$  during March 1977. In: F.A. Richards (Editor), Coastal Upwelling. American Geophysical Union, Washington, DC, pp. 473-495.
- Chia, F., Griffiths, R.W. and Linden, P.F., 1982. Laboratory experiments in fronts. Part II. The formation of cyclonic eddies at upwelling fronts. *Geophys. Astrophys. Fluid Dyn.*, 19: 198-206.
- Flament, P., Armi, L. and Washburn, L., 1985. The evolving structure of an upwelling filament. *J. Geophys. Res.*, 90: 11783-11798.
- Griffiths, R.W. and Linden, P.F., 1982. Laboratory experiments on fronts. Part 1. Density driven boundary currents. *Geophys. Astrophys. Fluid Dyn.*, 19: 159-187.
- Guillen, O. and Galienes, R., 1981. Upwelling off Chimbote. In: F.A. Richards (Editor), Coastal Upwelling. American Geophysical Union, Washington, DC, pp. 312-326.
- Hickey, B.M., 1979. The California current system—hypothesis and facts. *Prog. Oceanogr.*, 8: 191-279.
- Huyer, A., Smith, R.L. and Hickey, B.M., 1984. Observation of a warm-core eddy off Oregon, January to March, 1978. *Deep Sea Res.*, 31: 97-117.
- Ikeda, M. and Emery, W.J., 1984. Satellite observation and modeling of meanders in the California current system off Oregon and northern California. *J. Phys. Oceanogr.*, 14: 1-17.
- Kelley, K., 1985. The influence of winds and topography on the sea surface temperature patterns over the Northern California Slope. *J. Geophys. Res.*, 90: 11783-11798.
- Killworth, P.D., Paldor, N. and Stren, M., 1984. Wave propagation and growth on a surface front in a two-layer geostrophic current. *J. Mar. Res.*, 42: 761-785.
- Kraichnan, R., 1967. Inertial ranges in two-dimensional turbulence. *Phys. Fluids*, 10: 1417-1423.
- Leith, C.E., 1968. Diffusion approximation for two-dimensional turbulence. *Phys. Fluids*, 11: 671-674.
- Maxworthy, T., 1977. Topographic effects in rapidly rotating fluids: flow over a transverse ridge. *Z. Angew. Math. Phys.*, 28: 853-864.
- Maxworthy, T. and Narimousa, S., 1985. Experiments and observations on the effects of bottom topography on coastal upwelling. Symposium on Vertical Motion in the Equatorial Upper Ocean and Its Effects Upon Living Resources and the Atmosphere. UNESCO, Paris, 6-10 May, Paris.
- Mooers, C.N.K. and Robinson, A.R., 1984. Turbulent jets and eddies in the California current and inferred cross-shore transports. *Science*, 223: 51-53.
- Mooers, C.N.K., Collins, C.A. and Smith, R.S., 1976. The dynamic structure of the frontal zone in the coastal upwelling region off Oregon. *J. Phys. Oceanogr.*, 6: 3-21.
- Morales, Z.C., Argote, E.M.L., Amador, B.A. and Barton, E.D., 1978. Mediciones de vientos, corrientes e hidrografia frente a Punto Colonet, B.C. En Junio 1976. CICESI.
- Narimousa, S. and Maxworthy, T., 1985. Two-layer model of shear driven coastal upwelling in the presence of bottom topography. *J. Fluid Mech.*, 159: 503-531.
- Narimousa, S. and Maxworthy, T., 1986a. Laboratory modeling of coastal upwelling. *EOS Trans. Am. Geophys. Union*, 67: 2-3.
- Narimousa, S. and Maxworthy, T., 1986b. Effects of a discontinuous surface stress on a model of coastal upwelling. *J. Phys. Oceanogr.*, 16: 2071-2083.
- Narimousa, S. and Maxworthy, T., 1987a. Coastal upwelling on a sloping bottom. The formation of plumes, jets and pinched-off cyclones. *J. Fluid Mech.*, 176: 169-190.
- Narimousa, S. and Maxworthy, T., 1987b. A note on the effects of coastline perturbations on coastal currents and fronts. *J. Phys. Oceanogr.*, 17: 1296-1303.

- Narimousa, S., Long, R.R. and Kitaigorodskii, S.A., 1986. Entrainment due to turbulent shear flow at the interface of a stably stratified fluid. *Tellus*, 38A: 76-87.
- Narimousa, S., Maxworthy, T. and Spedding, G.R., 1987. Structure of meso-scale baroclinic turbulence. Sixth Symposium on Turbulent Shear Flows, Toulouse, September 7-9.
- Nelson, C.S., 1977. Wind stress and wind stress curl over the California Current. NOAA Tech. Rep. NMFS SSRF-714, U.S. Dept. of Commerce, 89 pp.
- Peffley, M.B. and O'Brien, J.J., 1976. A three dimensional simulation of coastal upwelling off Oregon. *J. Phys. Oceanogr.*, 6: 164-180.
- Pelaez, J. and McGowan, J.A., 1976. Phytoplankton pigment pattern in the California current as determined by satellite. *Limnol. Oceanogr.*, 31 (5): 927-950.
- Phillips, N.A., 1954. Energy transformations and meridional circulations associated with simple baroclinic waves in a two-level, quasi-geostrophic model. *Tellus*, 6: 273-286.
- Preller, R. and O'Brien, J.J., 1980. The influence of bottom topography on upwelling off Peru. *J. Phys. Oceanogr.*, 10: 1377-1398.
- Thomson, R.e. and Papadakis, J.E., 1987. Upwelling filaments and motion of a satellite-tracked drifter along the West Coast of North America. *J. Geophys. Res.*, 92: 6445-6461.

# Experiments on the structure and dynamics of forced, quasi-two-dimensional turbulence

By S. NARIMOUSA<sup>1</sup>, T. MAXWORTHY<sup>2†</sup>  
AND G. R. SPEDDING<sup>2</sup>

<sup>1</sup> University of Southern California, Department of Mechanical Engineering,  
Los Angeles, CA 90089-1453, USA

<sup>2</sup> University of Southern California, Departments of Aerospace and Mechanical Engineering,  
Los Angeles, CA 90089-1191, USA

(Received 25 December 1989 and in revised form 18 May 1990)

Simulated upwelling fronts have been generated around the outer edge of a cylindrical tank filled with a two-layer fluid system and driven by a surface stress. Initially, an axisymmetric front was observed which subsequently became unstable to small baroclinic eddies. These eddies continued to grow until they reached an equilibrium size. Under some circumstances, cyclonic eddies pinched-off from the fully developed front and moved away from the mean position of the front into the fluid interior. Streak photographs of the fully developed flow field were digitized to generate a velocity field interpolated on to a regular grid. A direct two-dimensional Fourier transform was performed on the turbulent kinetic energy field deduced from such images and one-dimensional energy  $E(k)$  spectra were extracted. Consistent  $k^{-\frac{2}{3}}$  energy spectra were found at lower wavenumber,  $k$ , and approximately  $k^{-5.5}$  spectra at higher  $k$ . In any given experiment, the two spectral slopes meet close to a wavenumber  $k_w = 2\pi/\lambda_w$  (where  $\lambda_w$  is the mean diameter of a frontal eddy and  $k_w$  is the associated wavenumber). According to classical theories,  $k_w$  would be the input wavenumber, and the range of  $k$  with a  $k^{-\frac{2}{3}}$  spectrum would correspond to an inverse energy cascade range; this yielded a Kolmogorov constant ( $C$ ) that varied within the limits  $2.8 \leq C \leq 3.8$ . The approximately  $k^{-5.5}$  range, which is much steeper than that predicted by the original statistical theories, is nevertheless consistent with those found frequently in numerical experiments.

The spectral slopes inferred from particle dispersion methods and from one-dimensional Fourier transforms of the longitudinal velocity correlations were compared with the results obtained above and in previous laboratory experiments. In general, the global energy spectra are consistent with an interpretation of the fluid dynamics as being that of two-dimensional turbulence. This in turn implies that known properties of such flows may be invoked to explain the appearance of a number of naturally occurring phenomena in coastal upwelling fronts.

---

## 1. Introduction

Satellite (IR) images have revealed meso-scale eddy structures at and in the vicinity of oceanic fronts (upwelling fronts), oceanic currents (the Gulf Stream), and more recently in the open ocean. As in the ocean, sharp-surfaced density fronts have

† Also Earth & Space Sciences Division, Jet Propulsion Laboratory, Pasadena, California, USA.



been produced and investigated in the laboratory (Griffiths & Linden 1981, 1982; Narimousa & Maxworthy 1987*a*). It has been found that soon after they form, the fronts become unstable to short baroclinic instabilities (waves), which grow in time until they reach a saturated size. Further development of these instabilities cause the fully developed frontal eddies to pinch off and produce isolated coherent vortices in the vicinity of the main front. This collection of frontal eddies combined gives rise to a velocity field that might be described in the language of two-dimensional or geostrophic turbulence.

### 1.1. *Upwelling phenomena in the laboratory and in the ocean*

One important motivation that triggered this study were observations of thin, long offshore-extending, cold filaments in satellite (IR) images taken off the west coast of the USA during coastal upwelling episodes (Narimousa & Maxworthy 1989). Intense turbulent jets or rivers, which are believed to transport the cold upwelled water far offshore, have been recognized as a possible source for generating these filaments. Narimousa & Maxworthy (1985, 1986, 1987*a, b*) observed in the laboratory that the turbulent jets were often associated with offshore eddies which could be generated in a variety of ways: (a) large-amplitude instability of standing waves generated by coastal perturbations; (b) large-amplitude baroclinic instability of the front itself and (c) production of eddies due to the presence of an offshore curl in the surface stress. In all cases interaction between the offshore eddies produced the offshore jets, which then transported the upwelled water offshore. If the structure of such an eddy field obeys the laws of two-dimensional or geostrophic turbulence, then the intense turbulent rivers which seem to thread through such eddy fields are responsible for transport of material across it and must be characteristics of such fields.

### 1.2. *Statistical theories of two-dimensional turbulence*

The early studies of two-dimensional turbulence were concerned with the dynamics of atmospheric meso- and large-scale eddies, which were thought to have two-dimensional structure. In the case of three-dimensional turbulence, Kolmogorov's (1941) cascade hypothesis indicated an equilibrium inertial subrange in which kinetic energy cascaded from low to higher wavenumber ( $k$ ), and the energy spectra took the form  $E \sim k^{-5/3}$ . In the case of two-dimensional turbulence there is a second constant of motion, called the enstrophy, which was defined as half of the squared vorticity  $\frac{1}{2}\omega^2$ . This led Kraichnan (1967) and Leith (1968) to propose both a direct enstrophy and an inverse energy cascade inertial range for the case of forced two-dimensional turbulence. They found that  $E \sim k^{-5/3}$  in the inertial range in which energy was transferred to lower  $k$  (an inverse cascade), and an  $E \sim k^{-3}$  inertial range in which enstrophy moved to higher  $k$ . Batchelor (1969) found the  $k^{-3}$  range for the case of a freely decaying two-dimensional turbulence, consistent with Kraichnan's and Leith's energy spectrum for the enstrophy cascade range. Studies of three-dimensional, quasi-geostrophic turbulence (Charney 1971; Salmon 1978; Herring 1980; Heyer & Sadourny 1982) indicated the existence of two inertial ranges,  $k^{-3}$  and  $k^{-5/3}$ , which was similar to the spectral characteristics of two-dimensional turbulence. (See also Lesieur 1987 for a comprehensive review.)

### 1.3. *Numerical simulations*

Besides the early computations of Lilly (1969, 1971, 1972), other numerical simulations of two-dimensional isotropic turbulence have frequently produced energy spectra considerably steeper than  $k^{-3}$  in the so-called enstrophy cascade range

(see Deem & Zabusky 1971; Fox & Orszag 1972; Herring *et al.* 1974; Fornberg 1977; Basdevant *et al.* 1981; Bennett & Haidvogel 1983; Haidvogel & Keffer 1984; McWilliams 1984). Herring *et al.* (1974), however, have recognized that very high resolution is required in numerical simulations in order to obtain a proper inertial range at higher wavenumbers. For grid resolutions respectively of  $1024^2$  and  $2048^2$  Brachet, Meneguzzi & Sulem (1986) and Brachet *et al.* (1988), observed a  $k^{-4}$  slope for a short time, which then rapidly changed to a  $k^{-3}$  slope for a more mature flow. Based on the isovorticity contours, they identified the initial regime ( $k^{-4}$  slope) to be associated with isolated, discontinuous vorticity-gradient sheets in the turbulent field, as hypothesized by Saffman (1971), who predicted such a spectral slope. The second regime ( $k^{-3}$  slope) corresponded to a maximum enstrophy dissipation period, which was the basis for the classical enstrophy cascade hypothesis resulting in the  $k^{-3}$  slope. Brachet *et al.* (1988) showed that at later times the vorticity-gradient layers would dissipate and coherent vortices associated with isolated concentrations of vorticity which last for a long time would dominate. This later case was investigated by McWilliams (1984) where such coherent vortex structure was associated with an energy spectrum closer to  $k^{-5}$ . More recent numerical simulations (Santangelo, Benzi & Legras 1989) have shown, however, that the value of the final spectral slope is quite sensitive to the shape of the initial energy spectrum.

#### 1.4. Quantitative experiments

Field measurements of large-scale atmospheric turbulence have tended to produce energy spectra scaling closer to the  $k^{-3}$  law (e.g. Julian *et al.* 1970; Kao, Jenne & Sagendorf 1970; Morel & Larcheveque 1974; Dubois 1975), while others have reported  $k^{-\frac{5}{3}}$  inertia range (e.g. Brown & Robinson 1979; Gage 1979; Nastrom & Gage 1983). Measurements of freely decaying two-dimensional turbulence in the laboratory produced an energy spectra with slopes close to  $\sim k^{-2.5}$  (Griffiths & Hopfinger 1984; Mory & Hopfinger 1986; Maxworthy, Caperan & Spedding 1987) at higher  $k$ , when the dispersion of particle pairs was used as the diagnostic tool. However, recent studies (summarized in Maxworthy 1989) have shown that such methods are in error when the actual spectral slope is larger than  $-3$ . In this case Babiano, Basdevant & Sadourny (1985) and Bennett (1984) argue that the lower spectral slopes found by particle dispersion methods were due to non-locality of the particle dynamics while the arguments which lead to the classical relationship between particle diffusion and spectral slope is based on local dynamics.

#### 1.5. A laboratory model for forced, two-dimensional turbulence

In the present study, the experiments of Narimousa & Maxworthy (1987*a*) were employed to investigate the structure of mesoscale turbulence generated via baroclinic instabilities at upwelling fronts. Since the flow field was maintained by a constant supply of energy (see §3), the turbulent flow was forced. As mentioned above, when Mory & Hopfinger (1986), Maxworthy *et al.* (1987) and Narimousa, Maxworthy & Spedding (1987) employed the same particle dispersion methods as Griffiths & Hopfinger (1984), the spectral slopes at higher  $k$  were almost identical. It appeared that, independent of the two-dimensional turbulence generation mechanism in the laboratory, the measured spectral slope was always close to  $\sim k^{-2.5}$ , if particle dispersion methods were used. This result was found to be independent of the number of particles, and considerable changes in values of turbulent Reynolds number or rotation rate (Maxworthy *et al.* 1987; Narimousa *et al.* 1987). Here, alternative attempts to measure the energy spectra  $E(k)$  in the instantaneous flow

Experiment	$\Omega$ (s <sup>-1</sup> )	$\Delta\Omega$ (s <sup>-1</sup> )	$h_0$ (cm)	$\partial\rho$ (g/cm <sup>3</sup> )	$u_*$ (cm/s)	$\lambda_s$ (cm)	$\theta_*$	$\delta t$ (s)
a	2.27	0.185	2.60	0.018	0.36	17.0	1.7	0.5
b	1.50	0.170	2.60	0.020	0.35	11.8	4.0	0.5
c	1.20	0.143	2.35	0.020	0.33	8.5	7.5	0.5
d	0.97	0.130	2.55	0.020	0.35	6.7	11.0	1.0
e	0.85	0.114	2.35	0.020	0.32	4.4	20.0	1.0

TABLE 1. Parameter values for the experiment of Narimousa & Maxworthy (1987*a*). Here  $\Omega$  is the tank rotation rate,  $\Delta\Omega$  is the differential rotation of the top disc,  $h_0$  is the depth of the top layer,  $\partial\rho$  is the density difference between the two layers,  $u_*$  is the applied friction velocity,  $\lambda_s$  is the final width of the upwelled water at the surface,  $\theta_* = (g'h_0)/(u_*f\lambda_s)$  (where  $g' = g\partial\rho$  and  $f = 2\Omega$  is the Coriolis parameter) is the fundamental controlling parameter of this system and  $\delta t$  is the exposure time for the streak photograph.

field are reported. Fourier transforms of either the two-point velocity correlations or directly on the two-dimensional kinetic energy fields provided two measures of  $E(k)$  which could be compared with theoretical, numerical and experimental values previously reported in the literature and with each other.

## 2. The experiment

Since the present study employs the experiments of Narimousa & Maxworthy (1987*a*), the reader is referred to that paper for a detailed discussion of the apparatus and the range of parameters used, and only a brief description will be given here.

Two layers of salt water of slightly different densities were brought to solid-body rotation inside a cylindrical tank (90 cm in diameter and 20 cm in depth) having a conical bottom with a slope of about 0.27. The surface of the upper fluid was in contact with a circular, smooth disk, which, as it rotated, applied a stress to this surface producing an alongshore shear flow and an offshore Ekman flux in the top layer. As a result, an upwelling front was formed around the outer edge of the tank. The velocity vectors of the current and the upwelling frontal movement were observed by placing small neutrally buoyant particles in the front and recording their motion by steak photography. The direction of motion of these particles were found by firing an electronic flash at the beginning of the time exposure. To reveal the structure of the eddies, the camera was set to rotate at a rate close to the drift velocity of the eddies. In this way a frozen velocity field was recorded and the resulting streaks represented the turbulent velocities.

In the present study, five experiments with parameter values shown in table 1 below are subject to spectral analysis.

## 3. Evolution of forced mesoscale turbulence

When the system was in solid-body rotation, the top disk was set to rotate anticyclonically, thus applying a stress to the top surface of the lighter fluid. The resulting Ekman flux caused the top layer to spin down and the interface to rise near the wall and to descend at the centre of the tank. The interface continued to rise near the wall until it intersected the top disk and a surface front was formed. This front then migrated away from the wall and allowed bottom water to appear at the surface around the outer edge of the tank. Eventually, the horizontal pressure gradient

caused by front deformation balanced the Coriolis force and the front became stationary at a distance  $\lambda_s$  from the wall of the tank. Prior to this, at a distance  $\lambda_1 < \lambda_s$  the upwelling front became unstable to small baroclinic instabilities. During migration of the front, the small disturbances continued to grow until they reached a saturated size  $\lambda_w$ . In this way intense baroclinic eddies of the form of cyclone-anticyclone pairs dominated the sharp-surfaced density front. The distance where the waves first appeared at the front  $\lambda_1 \approx 0.7\lambda_s\theta_*^{-0.5}$ , and the mean diameter of the saturated waves  $\lambda_w \approx 0.15gh_0/u_*f$  were given by Narimousa & Maxworthy (1987*a*).

At large values of  $\theta_*$ , the frontal eddies were large, and they tended to remain at the front and consequently no pinch-off process was observed. Later, however, less intense eddies were formed in the upper layer adjacent to the more intense frontal eddies (figure 1*a*). At moderate values of  $\theta_*$ , frontal eddies were of a smaller size and they were more intense, yet no eddy escaped from the front. Here again, less intense eddies were formed in the upper layer (figure 1*b*) just as those seen in flows with large  $\theta_*$ .

At low values of  $\theta_*$ , frontal instabilities were much more intense and the upwelling front itself displayed strong unsteadiness. This eventually initiated large-amplitude wave instabilities which usually started at the wave troughs (i.e. the location of the cyclonic eddies) and then grew into the fluid interior. Later, cyclonic eddies were detached from such intrusions to form intense, isolated coherent cyclonic eddies in the top layer (figure 1*c*) away from the mean position of the front. Initially, the mean diameter of a pinched-off cyclone was about the same as that of frontal eddies  $\lambda_w$  but they subsequently continued to grow to a large value of about 3–4 times greater than  $\lambda_w$ , (i.e. an inverse energy cascade). Detachment of the cyclonic eddies occurred randomly at different locations of the front. Interactions of the pinched-off cyclones forced intense anticyclones to develop in between them. The pinched-off eddies, in particular, are of special interest in the present study because of their importance in the transport of the material across the turbulent flow field. To illustrate this Narimousa & Maxworthy (1987*a*) released a passive marker within the upwelled water near the wall of the tank. The radial Ekman flow transported the marker toward the front where it interacted with the frontal eddies. At the pinched-off eddy, the marker was transported abruptly into the fluid interior by the induced flow. Such demonstrations in the laboratory led to the conclusion that the presence of eddies adjacent to an upwelled water front, for example, can be responsible for the transport of the upwelled water into the eddy field, in the form of long filaments.

We proceed to investigate such flows by means of statistical tools to measure their energy spectra. Such measurements should provide us with the information to show whether or not our model has at least some of the characteristics of two-dimensional turbulence as determined from theoretical and numerical studies.

## 4. Particle image analysis

### 4.1. Procedure

A variety of statistical methods may be applied to the frozen turbulent flow represented by streak photographs such as figure 1(*a–c*). In these photographs, the beginning of each streak is composed of a bright spot followed by a less bright tail. Provided that particles do not move out of the illuminated region, their length is proportional to their velocity integrated over the exposure time,  $\delta t$ . The practical choice of  $\delta t$  reflects a compromise between upper bounds due to excessive curvature

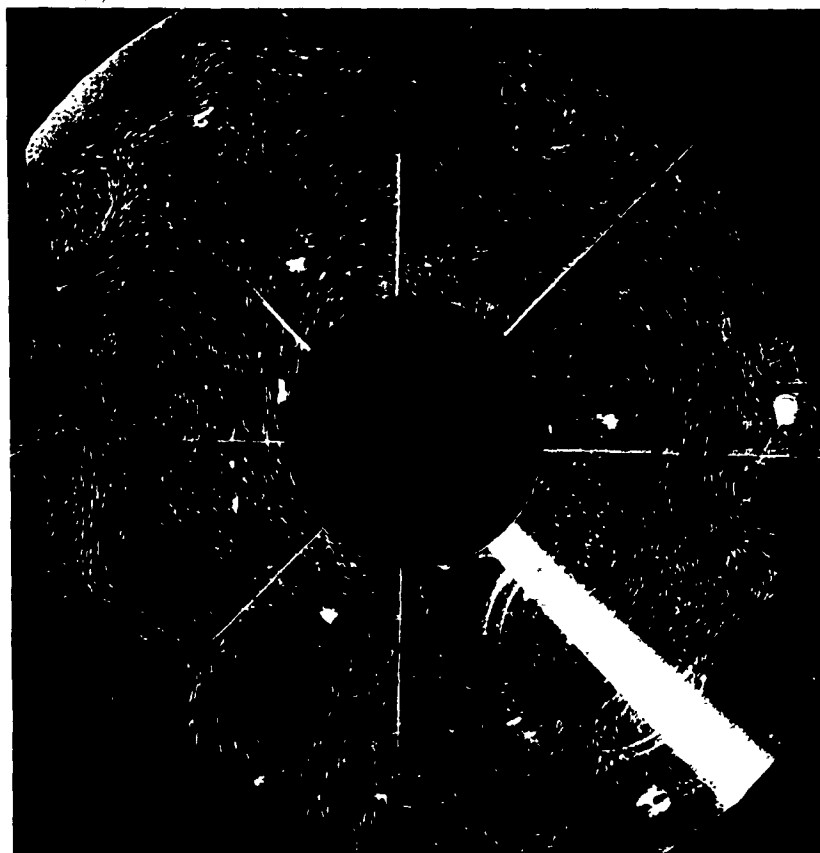
*(a)**(b)*

FIGURE 1(a,b). For caption see facing page

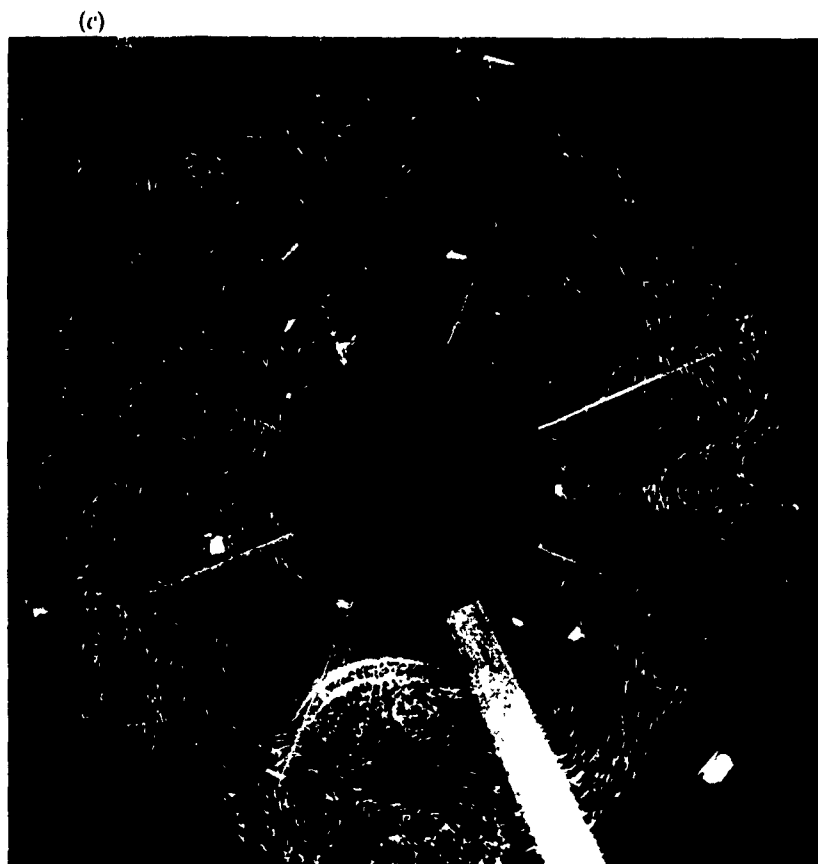


FIGURE 1. Streak photographs of frozen fields showing examples of the long-time behaviour of meso-scale eddy structures at upwelling fronts and their immediate vicinity. Photographs (a-c) correspond to experiments e, c and a, respectively.

of the particle tracks and lower limits on the detectability of motion in low-speed regions. The exposure times (0.5, 1 s) were determined by the internal timer of a Nikon F2 camera. At these shutter speeds the uncertainty in  $\delta t$  is less than 1%. In each digitized photograph, the end points of 2000–4000 particle streaks were digitized. The irregularly spaced particle velocity data were interpolated on to a  $32^2$  grid by convolution with an adaptive Gaussian window, as described by Agüí & Jimenez (1987).

#### 4.2. Error estimates

The likely sources and magnitudes of the errors in both of these processes have been considered in some detail by Imaichi & Ohmi (1983), Agüí & Jimenez (1987) and Rignot & Spedding (1988). A reasonable error estimate for image digitization is 5%, which is likely to be significantly below the errors introduced by the subsequent interpolation. Rignot & Spedding (1988) presented a detailed comparison between smoothing window-based (adaptive Gaussian window, AGW) interpolations and a thin shell spline (STS) method for the particular case of particle tracking in fluid flows. The magnitude of these errors may be expressed as a function of the characteristic lengthscale of the flow,  $L$ , the mean nearest-neighbour distance between particles,  $\delta$ , and the grid spacing,  $h$ . These may be written as the dimensionless ratios  $L/h$  and  $h/\delta$ , which take the values 5 and 2.5 respectively on average in this case. Thus, one might expect *a priori* errors in  $u$  and  $\omega$  of the order of 5 and 10% respectively, according to the simulations of Rignot & Spedding. Bootstrap error estimates on the interpolated  $u$ - and  $\omega$ -fields support this prediction. Clearly the interpolated grid results need to be interpreted with caution. The

accuracy of the AGW technique is not sufficient to determine the details of the shapes of the  $\omega$ -distributions and the satisfactory  $h/\delta$  ratio is achieved at the expense of  $L/h$ ; in other words the resolution at small scales is poor. The highest accessible wavenumber  $k \approx \pi$ , but values for  $k$  several times smaller than this may be suspect. Since values of  $k > 1$  are of some interest in this study, an extensive range of grid interpolations were performed, varying the relative grid size, implicit and explicit smoothing parameters and differencing schemes for the AGW interpolation. Comparisons were also made with selected STS and local linear least-squares interpolators. The shape of the global  $E(k)$  spectrum below  $k \approx 2$  was not affected by changes in the interpolation scheme, nor by small changes in  $h$  around the actual values used for the AGW interpolations reported here. By contrast, the tail of the  $E(k)$  distribution, for  $k > 2$ , could be moved almost at will by altering the interpolation parameters. The distributions plotted here appear to lie on linear extrapolations of the data inside  $k = 2$ , but these values are extremely sensitive to the analysis techniques, and should not be taken as accurate. The estimate of spectral slopes in the enstrophy cascade range must be made from the rather small range of  $1 \leq k \leq 2$ . From the comparative and parametric studies of the grid interpolation techniques, the contribution to the uncertainty in assigning an exponent to the energy decay in this region from the interpolation process is approximately  $\pm 0.5$ .

The seeding particles themselves are neutrally buoyant, and have a mean diameter of approximately 0.83 mm. The minimum resolvable lengthscale, dictated first by the particle density, and second by the grid mesh size,  $h$ , is more than an order of magnitude larger than this.

#### 4.3. Measurements

The global energy spectrum of each flow field image was estimated in three different ways: (a) relative particle dispersion measurements, (b) two-dimensional Fourier transform of the turbulent kinetic energy field ( $\frac{1}{2}u'^2$ ) on the grid data, and (c) Fourier transforms of the longitudinal two-point turbulent velocity correlation coefficients. There are different assumptions, implicit or explicit, behind each of these techniques which will be discussed in turn. One may note that technique (b) uses the grid-interpolated data, while techniques (a) and (c) do not.

### 5. Results

#### 5.1. Method (a)

Particle dispersion methods were introduced by Morel & Larcheveque (1974) to calculate the energy spectrum of large-scale atmospheric turbulence by observing the relative motion of balloon pairs. Griffiths & Hopfinger (1984) extended this dispersion method, based on a suggestion by one of the present authors, to calculate  $E$  from an analysis of streak photographs similar to those of the present study. Briefly, they related the mean-square relative velocities of the particle pairs (or the structure function, Mory & Hopfinger 1986)  $\langle (dD/dt)^2 \rangle$ , to their separation ( $D$ ) to find

$$\left\langle \left( \frac{dD}{dt} \right)^2 \right\rangle \sim D^{\alpha-1}, \quad (1)$$

where  $D$  is the mean separation of the particle pairs,  $t$  is the time and the angle brackets indicate an average over all particle pairs. In (1) the turbulence is assumed

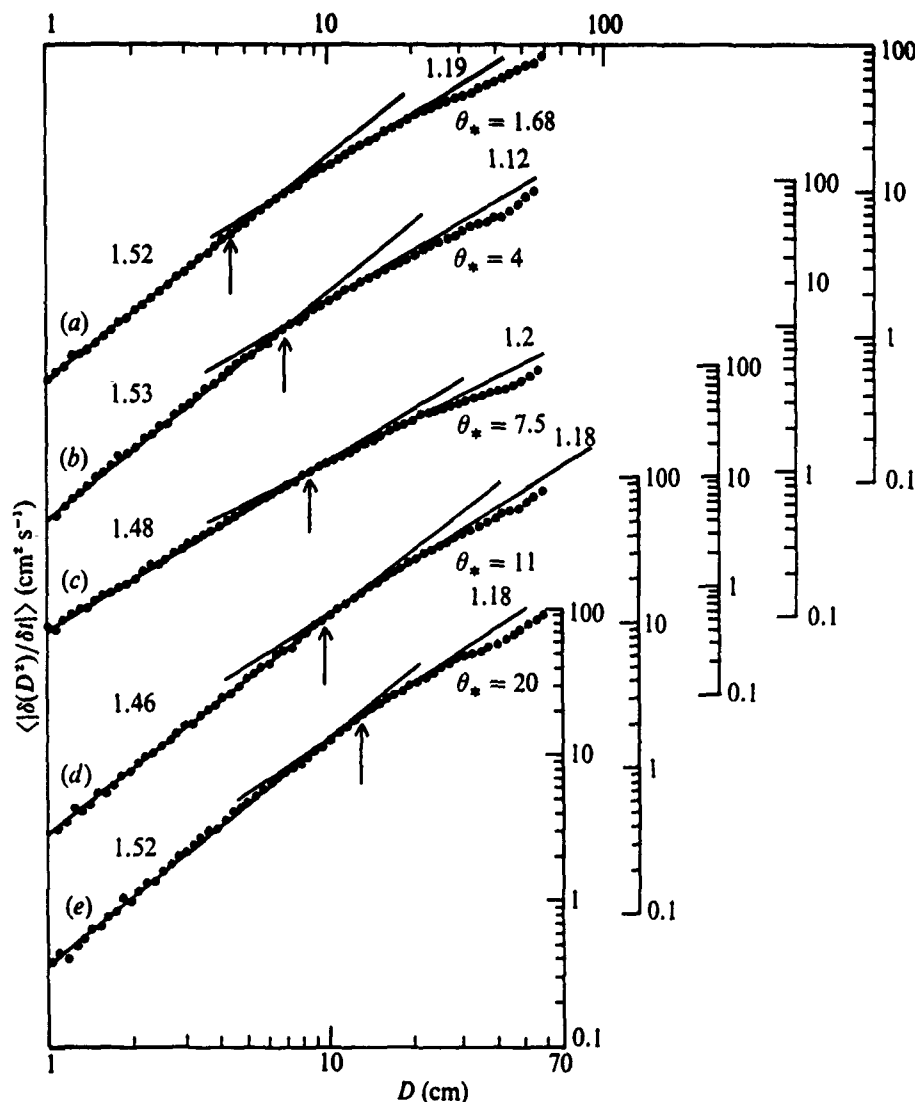


FIGURE 2. Variation of particle dispersion  $\langle |\delta D^2 / \delta t| \rangle$  with separation  $D$ ; (a–e) correspond to experiments a–e, respectively. The vertical arrows indicate the wavelength of the frontal eddies. Values of the slopes are indicated.

to be stationary and homogeneous and the energy spectrum takes the form of a simple power law,  $E \sim k^{-\alpha}$ , where  $\alpha$  is an unknown constant to be determined experimentally. A sharp cut-off at some energy dissipation wavenumber and local particle dynamics are assumed in the analysis leading to (1).

The same authors also considered the dissipation rate, or diffusivity of particle pairs  $\langle dD^2/dt \rangle$ , and since the mean Eulerian value of this quantity over a large number of particle pairs in a two-dimensional flow should be zero, Griffiths & Hopfinger (1984) defined a quadratic diffusivity  $\langle |dD^2/dt| \rangle$  and related it to  $(D)$  to find

$$\left\langle \left| \frac{dD^2}{dt} \right| \right\rangle \sim D^{1/2(\alpha+1)}. \quad (2)$$

Note that (2) was obtained using the same assumptions used to obtain (1).

In order to obtain  $\alpha$  and therefore the form of  $E$ , we adopt the data collection technique introduced by Griffiths & Hopfinger (1984). Consider two particles located at initial positions  $r_1$  and  $r_2$  at the beginning of a photographic exposure, and at  $r'_1$  and  $r'_2$  after time  $\delta t$ , and define the mean separation  $D = \frac{1}{2}((r'_2 - r'_1) + (r_2 - r_1))$ , the



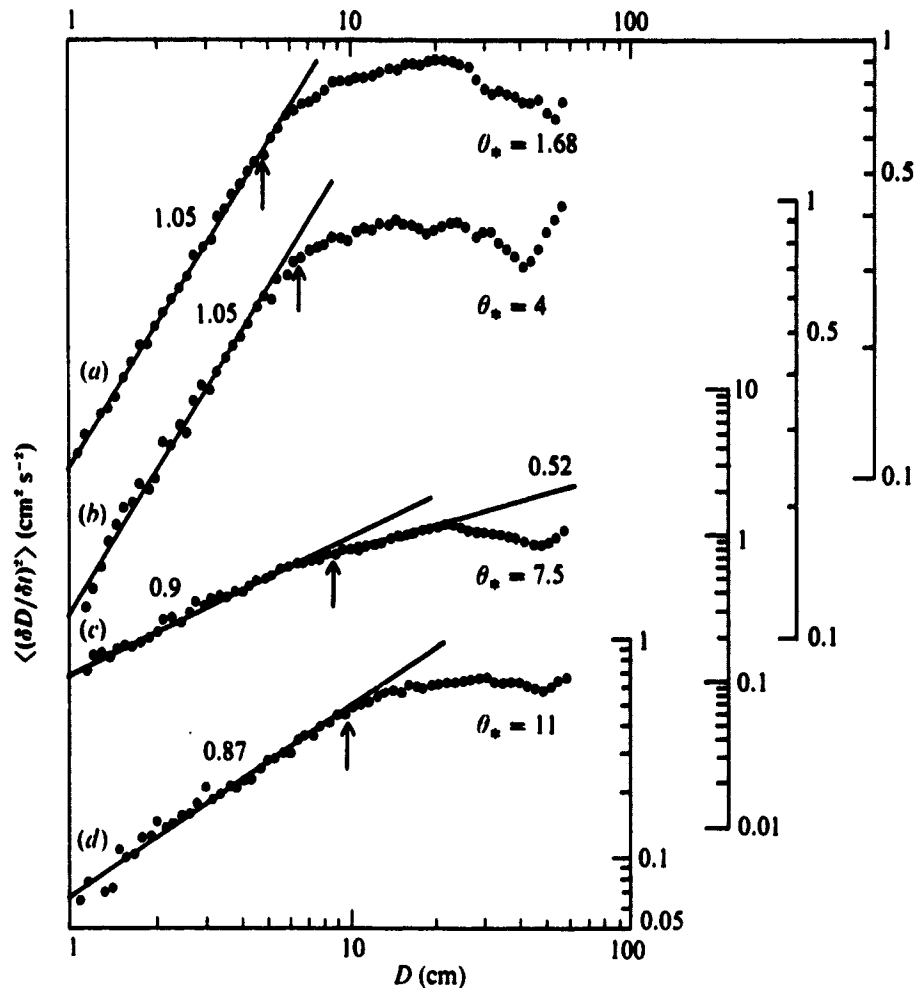


FIGURE 3. Variation to the mean square relative velocity  $\langle (\delta D / \delta t)^2 \rangle$  with separation  $D$ ; (a-d) correspond to experiments a-d respectively. The arrows are as in figure 2 and values of the spectral slopes are indicated. Note the different vertical scales for (a, b) and (c, d) respectively.

change  $\delta D = (r'_2 - r'_1) - (r_2 - r_1)$  and  $\delta(D^2) = 2D\delta(D) = (r'_2 - r'_1)^2 - (r_2 - r_1)^2$ . These quantities may be calculated directly for every particle pair in a given digitized photograph and, given  $\delta t$ , then the left-hand side of (1) and (2) can be calculated for all particle pairs for given separations.

To compute  $\alpha$ , the quadratic diffusivity  $\langle |dD^2/dt| \rangle$  and the structure function  $\langle (dD/dt)^2 \rangle$  are plotted as a function of the separations  $D$  in figures 2 and 3 for the five experiments. In general, for each experiment, there appear to be two ranges of  $D$  where straight lines may be fitted to the data, and these two lines intersect at a value of  $D \approx \lambda_w$ . The slopes of these lines, which were fitted by eye, do not vary significantly with  $\theta_*$ . For  $D < \lambda_w$ ,  $\alpha \approx +2$ , considerably smaller than the value of  $+3$  of classical turbulence results, and smaller still than typical numerical simulation results. When Babiano *et al.* (1985) substituted non-local energy spectra steeper than  $k^{-3}$  into the analysis leading to (1), they found that the structure function  $\langle (dD/dt)^2 \rangle$  saturated at  $D^2$ , and became independent of the true exponent,  $\alpha$ . Their results indicated that (1) is valid only for  $1 < \alpha < 3$ , and the use of (1) for measurements in the laboratory flows should always give a spectral slope within that range. This may explain why spectral slopes  $\alpha \leq 3$  were obtained in the present and previous laboratory studies when particle dispersion methods were used.

For wavelengths greater than  $\lambda_w$ , figures 2 and 3 imply that  $\alpha \approx +\frac{3}{2}$ , less than the  $+\frac{3}{2}$  predicted by classical theories for the inverse energy cascade inertia range.

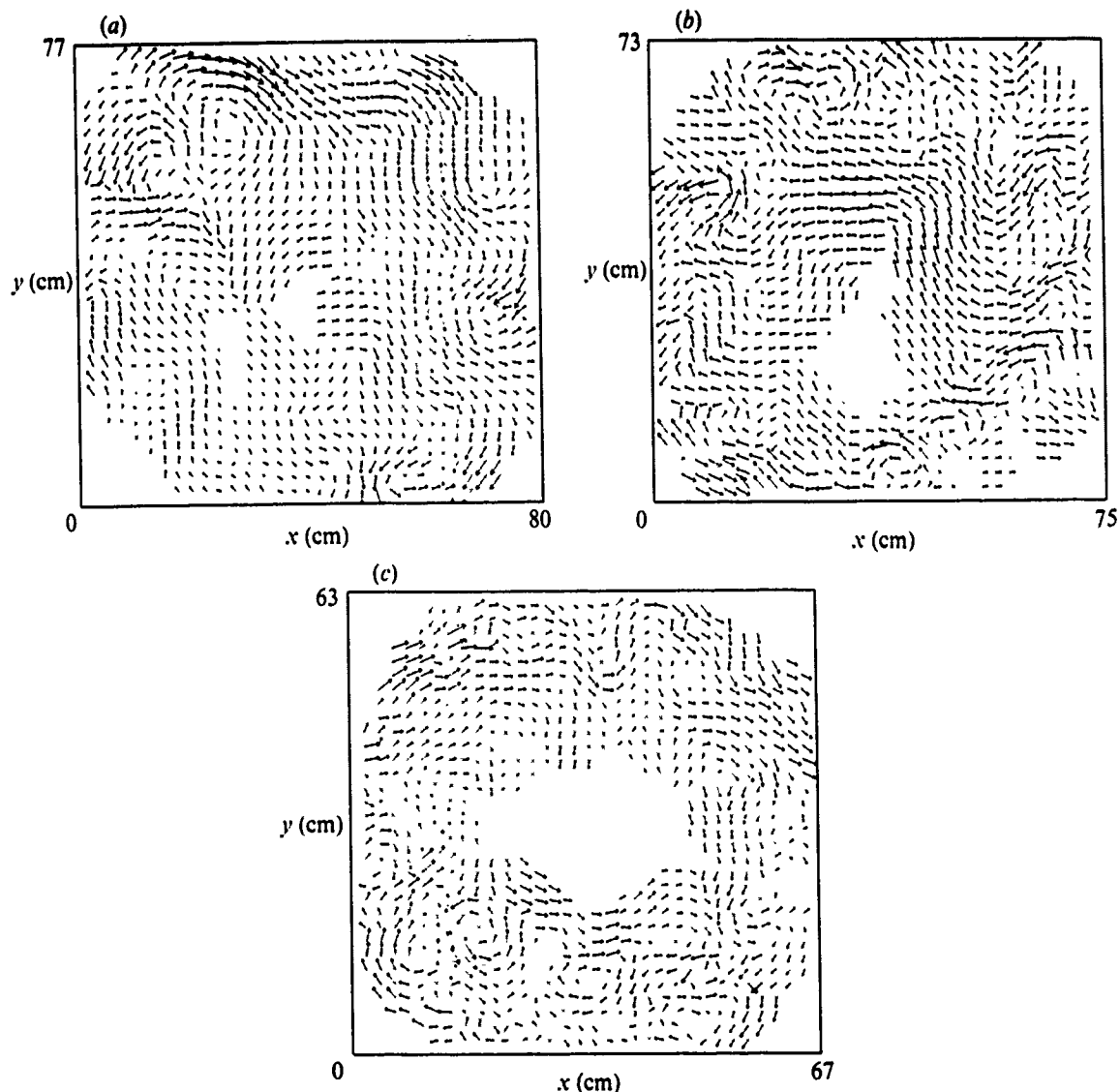


FIGURE 4. The original particle streak data as interpolated on to a regular  $32^2$  grid by convolution with an adaptive Gaussian window. Here (a-c) correspond to figure 1 (a-c) respectively.

Although this method did not produce the spectral slopes obtained in theories and numerical simulations, it does suggest that the input wavelength is about the same as the mean diameter of the frontal eddies  $\lambda_w$ .

### 5.2. Method (b)

Here, one computes a two-dimensional FFT on the square-grid-interpolated  $u'^2$  field (figure 4). With only a  $32 \times 32$  resolution in  $x$  and  $y$ , only a limited range of Fourier coefficients are calculated, and great care must be taken in windowing the data at the edges and centre of the square grid, which has been superimposed on data occupying an annulus-shaped region within its borders. The two-dimensional spectra were collapsed on a one-dimensional transect by adding values around circular shells centred at the origin  $(kx_0, ky_0)$ . The procedure was similar to that described by Armi & Flament (1985) and their cautionary remarks concerning the interpretation of power spectra should be borne in mind here. Particular care should be taken for the higher values of  $k$ , where details of the interpolation, smoothing and windowing techniques may have a significant influence, as discussed in §4.

Once again the  $E(k)$  curves (figure 5) appear to be divisible into two regions, each

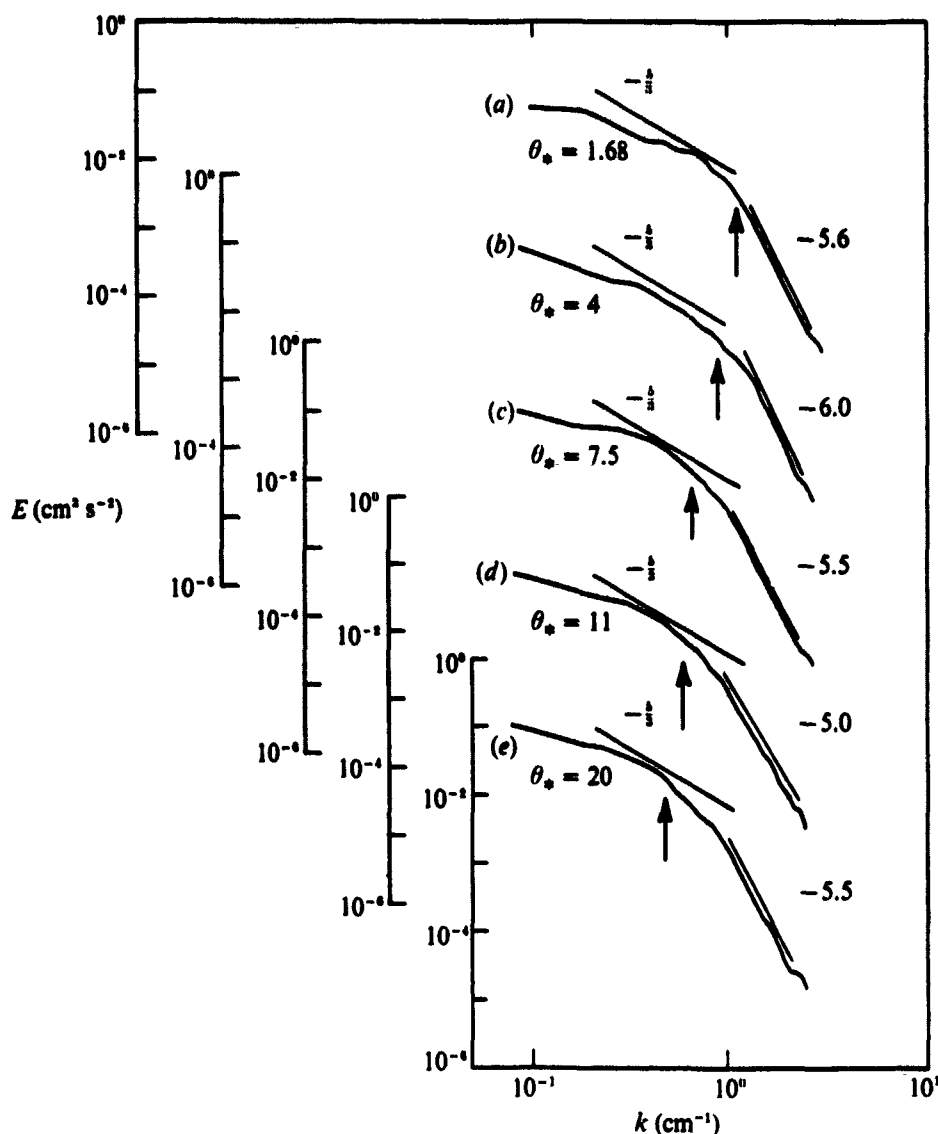


FIGURE 5. One-dimensional energy spectra ( $e$ ) as a function of wavenumber ( $k$ ), inferred from a direct two-dimensional, FFT of the  $u'^2$  velocities deduced from the interpolated data such as those shown in figure 4. The labels (a-e) correspond to those in figure 2. Rough estimates of spectral slopes are indicated for each experiment. The vertical arrows indicate the wavenumber of the frontal eddies.

of which may be approximated by a straight line fit (by eye). At low  $k$ , the slopes are consistent with a  $-\frac{5}{3}$  law; above a relatively well-defined value of  $k$ , however, all spectra show a much steeper drop-off, having values of approximately  $-5.5$  for a wide range of values of  $\theta_*$ .

While the  $-\frac{5}{3}$  slopes are quite consistent with the inverse energy cascade described by statistical theory of forced two-dimensional turbulence, the high-wavenumber behaviour differs from the predicted  $-3$  law, in common with results from a number of numerical experiments for both the constant-forcing and the freely decaying cases (e.g. McWilliams 1984; Frisch & Sulem 1984; Herring & McWilliams 1985; Brachet *et al.* 1988) and as found also by Sommeria (1986) for mercury in a closed box in the presence of a strong magnetic field. In general, attention has been focused on the development and subsequent evolution of isolated patches of vorticity which persist for long times and seem to be responsible for exponents steeper than  $-3$ . Santangelo *et al.* (1989) have shown that the value of  $\alpha$  is actually quite sensitive to the shape of the initial energy spectrum in the freely decaying case and it is reasonable to

suppose that this role might be assumed by the nature of the forcing in the stationary case. Under these circumstances the many different values of spectral slopes reported in the literature are not so surprising. As these authors noted, this sensitivity to initial conditions casts some doubt as to the truly universal nature of two-dimensional turbulence, or at least numerical simulations of it.

In the present study, the recorded turbulent velocity field represents the fully developed, long-time behaviour of the flow (see §3). Figure 6(a-c) shows examples of contour maps of the vorticity field in which many coherent vortex structures can be seen. These structures are closely packed as in Brachet *et al.* (1988) and Santangelo *et al.* (1989) for example, and not isolated as found by McWilliams (1984). Given the nature of the interpolation technique, one is almost guaranteed that the higher-order statistical moments have not converged and only the most general remarks may be made. Having said that, the kurtosis of the vorticity field,

$$k_\omega = \frac{1}{M \times N} \sum_{j=1}^N \sum_{i=1}^M \left[ \frac{\omega_{ij} - \bar{\omega}}{\sigma} \right]^4. \quad (3)$$

is a measure of the flatness of the vorticity distribution  $\omega_{ij}$  on the  $M \times N$  grid array. The mean value was 4.0 over experiments a-e and the maximum value was 4.6. This is far below the values of 10-30 reported by McWilliams (1984) and is more comparable to the value of a Gaussian distribution where  $k = 3$ . We can make no more precise statements on the shape of the vortices except that they are not isolated and strongly peaked. Nevertheless, we found that such coherent vortex structures can actually produce an approximately  $k^{-5.5}$  energy spectrum. This implies that, so far as the long-time behaviour of the flow is concerned, the slope of energy spectra at higher  $k$  is always steeper than  $k^{-3}$ , regardless of the degree of isolation of the coherent vortices. The fact that the turbulent flow in our laboratory model is forced, rather than freely decaying, may reduce the degree of isolation, as vortices of size  $\lambda_w$  are constantly generated at the front and injected into the system.

If the wavenumber  $k_w = 2\pi/\lambda_w$  corresponds to the frequency at which most energy is injected into the flow field then the two spectral slopes for each experiment should meet at this point on the  $k$ -axis. Figure 5 shows that this is a plausible interpretation of the data for each of the five different values of  $\theta_*$ . Since  $\lambda_w \sim (g'h_0)/(u_*f)$  is a function of both the Rossby deformation radius  $Ro = (g'h_0)^{0.5}/f$  and the Richardson number  $Ri = (g'h_0)/u_*^2$ , we can write

$$k_w = \frac{2\pi}{\lambda_w} \sim 2\pi \left( \frac{u_*f}{g'h_0} \right) \sim 2\pi Ri^{-0.5} Ro^{-1}. \quad (4)$$

Table 2 shows the values of  $\lambda_w$ ,  $Ro$ ,  $Ri$ ,  $\alpha$  (at large  $k$ ) and  $\theta_*$  for experiments a-e of figure 5, respectively. This table shows that in any given experiment  $\lambda_w$  is about 3 times greater than  $Ro$ . Initially, when the eddies first appear at the front they have a size comparable with  $Ro$ , but they continue to grow to a final size  $\lambda_w$ , controlled by  $\theta_*$ . When the values of  $\lambda_w$  obtained in the present study were compared with those obtained in previous studies of baroclinic turbulence (Phillips 1954; Griffiths & Linden 1982, Chia, Griffiths & Linden 1982; and Killworth, Paldor & Stern 1984) a good agreement was achieved. Under circumstances (figure 1c) when eddies are pinched-off from the front (see §3), their scale increases to values of  $\sim 4\lambda_w$  and/or  $\sim 12Ro$ . At this stage such eddies could be of equivalent-barotropic type (McWilliams 1984). However, Griffiths & Linden (1981) showed that at values of  $h_0/H \geq 0.25$  ( $H$  is the average total depth of the water), which is the case in the present experiments, the generated instabilities are of baroclinic type.

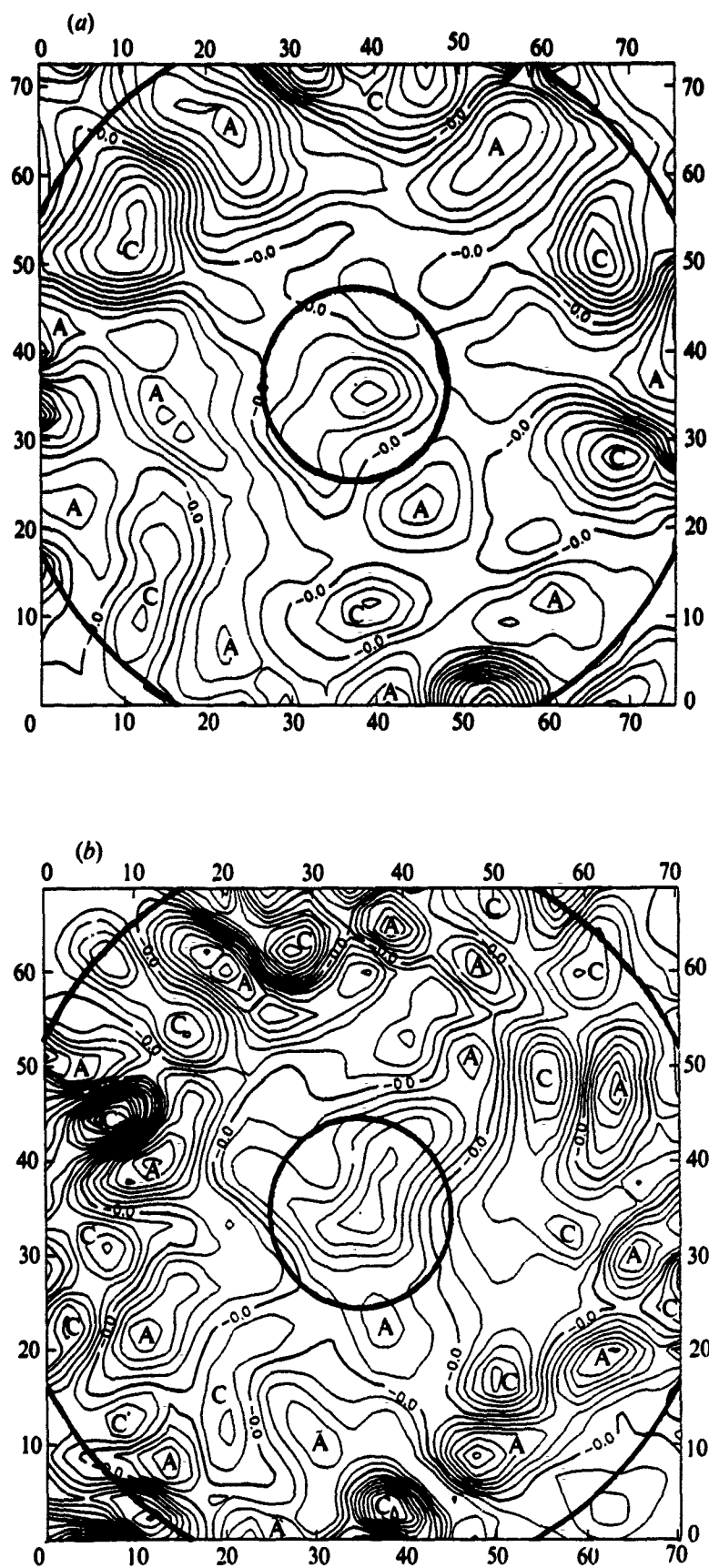


FIGURE 6(a,b). For caption see facing page.

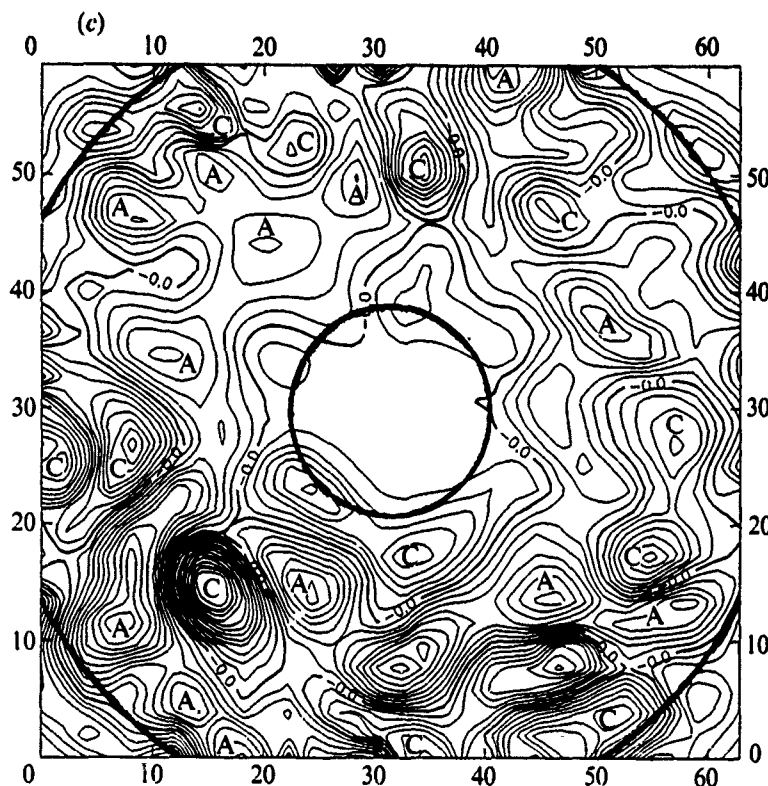


FIGURE 6. Isovorticity contours for the grids of figure 4. There are 16 contour levels, linearly spaced between  $\omega_{\min}$  and  $\omega_{\max}$ . Contour levels drawn outside the boundaries of the tank (heavy lines) are artifacts of the contouring routine which insists on data on a rectangular grid. The cyclones are indicated by C, while the anticyclones by A.

	$\lambda_w$ (cm)	$Ro$	$Ri$	$\alpha$	$\theta_*$
a	4.3	1.5	355	-5.6	1.7
b	7.0	2.4	416	-6.0	4.0
c	9.6	2.8	422	-5.5	7.5
d	11.0	3.6	408	-5.0	11.0
e	13.2	4.0	449	-5.5	20.0

TABLE 2.

### 5.3 Method (c)

This method is used widely in calculating one-dimensional energy spectra in three-dimensional isotropic turbulence. Assuming the turbulence to be isotropic, the values of the longitudinal velocity correlation coefficients  $F(r)$ , are defined by

$$F(r) = \frac{\overline{u_1(x)u_1(x+r)}}{\overline{u^2}}, \quad (5)$$

where  $u_1$  denotes the velocity components parallel to the vector separation  $r$ . The velocity components  $u(x)$  and  $u(x+r)$  were obtained directly from projection of the particle streaks at  $x$  and  $x+r$  on  $r$ . Here,  $\overline{u^2}$  is defined by

$$\overline{u^2} = \frac{1}{N} \sum_{i=1}^N u_i^2, \quad (6)$$

for  $N$  particles.  $F(r)$  was calculated for each particle pair in a given streak

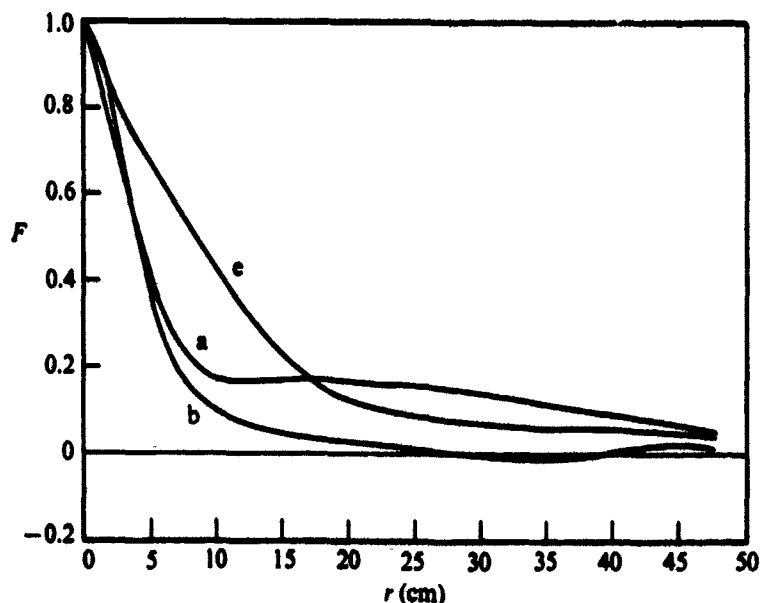


FIGURE 7. Variation of the longitudinal velocity correlation function  $F$  as a function of separation  $r$ , for experiments a, b and e.

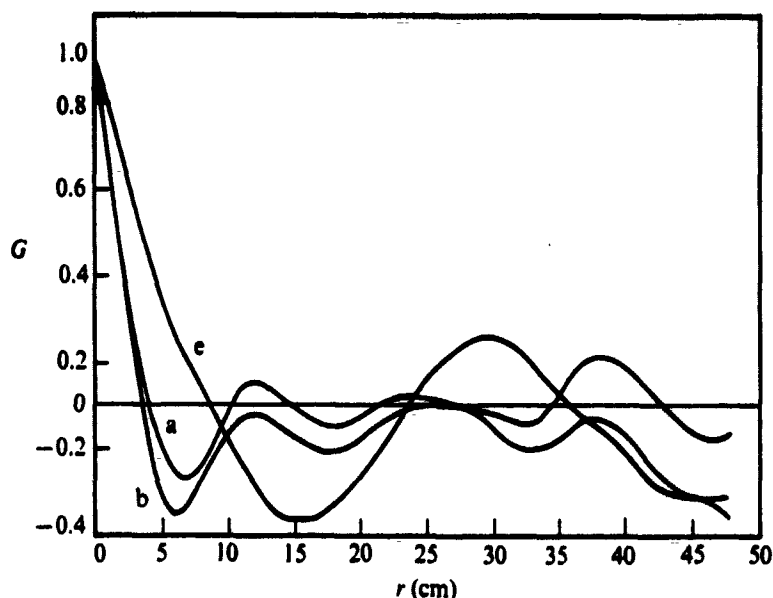


FIGURE 8. Variation of the lateral velocity correlation function  $G$  as a function of separation  $r$ , for experiments a, b and e.

photograph, and the results were averaged for a number of discrete bins in  $r$ .  $F(r)$  is plotted for experiments a, b, and e in figure 7. Similarly, the values of lateral correlation coefficients  $G(r)$  were calculated and plotted in figure 8.  $G(r)$  is defined by

$$G(r) = \frac{\overline{u_z(x) u_z(x+r)}}{\overline{u_z^2}}, \quad (7)$$

where  $u_z$  denotes velocity components perpendicular to vector separation  $r$ . Figures 7 and 8 indicate that the form of the functions  $F(r)$  and  $G(r)$  is typical of that predicted theoretically for two-dimensional turbulence (for example, see Townsend 1976, pp. 1-6).

The Fourier transform of the longitudinal correlation function  $F(r)$  allows the  $E(k)$  spectrum to be estimated and two examples appear in figures 9 and 10, for  $\theta_* = 4$  and

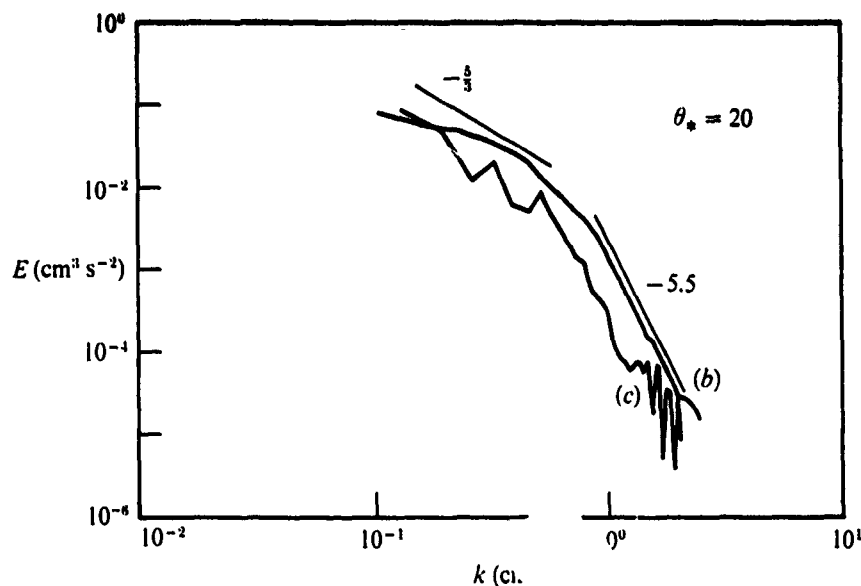


FIGURE 9. One-dimensional energy spectra  $E$  as a function of wavenumber  $k$ , calculated by (b) method (b), and (c) method (c) for experiment e.

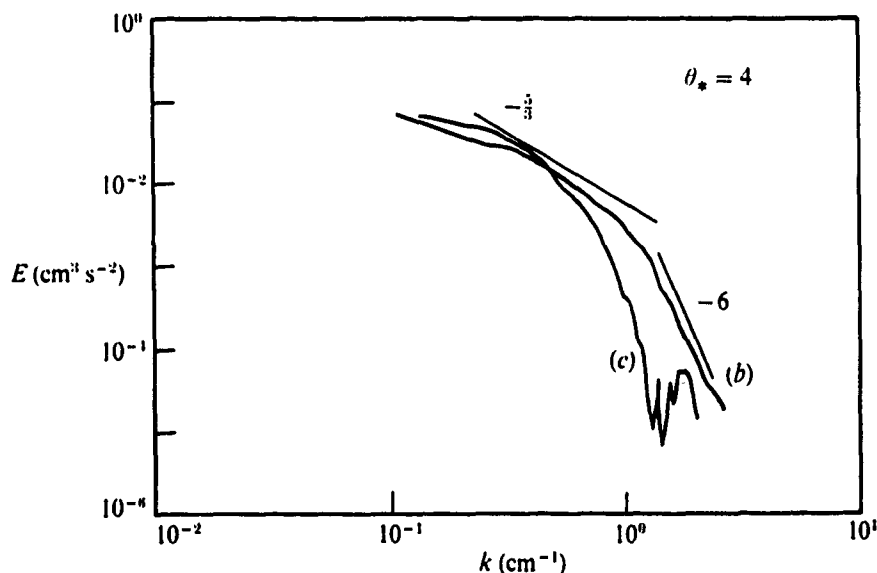


FIGURE 10. As in figure 9, but for experiment b.

20 (experiments b and e). The ringing of the data derived from the transformed correlation functions is a consequence of the spline interpolation of  $F(r)$  preceding the transform operation and is hard to remove, but the upper envelope of this curve corresponds quite closely to the results from method (b). Hence, at wavenumbers  $k < k_w$ , the spectral slope generated using method (c) is consistent with  $k^{-5/3}$ , the inverse cascade inertia range. At wavenumbers  $k > k_w$ , method (c) did not produce well-correlated energy spectra when compared with the results generated by method (b), but in an average sense the spectral slopes are close to those that ( $\sim k^{-5.5}$ ) given by method (b). The fact that methods (b) and (c) give similar decay laws to within experimental accuracy lends a degree of support for the interpolation procedures required for (b).

#### 5.4 The Kolmogorov constant

It is possible to estimate the two-dimensional Kolmogorov constant ( $C$ ) in the equation

$$E(k) = C\epsilon^{2/3}(k)^{-5/3}, \quad (8)$$



	$A$	$\epsilon$	$C$	$\theta_*$	$R_t$
a	$0.5 \times 10^{-3}$	$0.75 \times 10^{-4}$	2.8	1.7	340
b	$0.5 \times 10^{-3}$	$0.73 \times 10^{-4}$	2.86	4.0	460
c	$0.52 \times 10^{-3}$	$0.6 \times 10^{-4}$	3.4	7.5	660
d	$0.5 \times 10^{-3}$	$0.48 \times 10^{-4}$	3.8	11.0	511
e	$0.5 \times 10^{-3}$	$0.48 \times 10^{-4}$	3.8	20.0	830

TABLE 3.

where  $\epsilon$  is the rate of energy injection to large scales. For the inverse cascade range, figure 5 gives an energy spectrum of the form

$$E(k) = A(k)^{-\frac{1}{2}}, \quad (9)$$

where the constant  $A$  can be determined directly from figure 5. Comparing (8) and (9) we find

$$C = \frac{A}{\epsilon^{\frac{1}{2}}}. \quad (10)$$

If the bottom layer is stationary (Narimousa & Maxworthy 1985), and the dissipation driving the Ekman layer is small compared with the dissipation at the interface, then the injected kinetic energy is dissipated mostly due to the action of molecular viscosity, and  $\epsilon$  can be estimated from

$$\epsilon = 2\nu \int_0^\infty k^2 E(k) dk \quad (11)$$

(see Batchelor 1953, §6.4 and Lesieur 1987, §5.3). Substituting (9) for  $E(k)$  and integrating (11) within the range of wavenumbers in which figure 5 indicates the  $k^{-\frac{1}{2}}$  inertia range, we find the value of  $\epsilon$  and then from (10) the value of  $C$ . Table 3 shows the estimated values of  $A$ ,  $\epsilon$  and  $C$  for experiments a–e of figure 5, respectively. These values of  $C$  are within the range of those estimated by Lilly (1969), 4.3–6.2; Herring & Kraichnan (1975), 6.5; Herring & McWilliams (1985), 2.9–4.8; and Sommeria (1986), 3–7; but smaller than those of Frisch & Sulem (1984), 9; and much smaller than those of Siggia & Aref (1981), 14. The above table shows also the values of  $\theta_*$  and  $R_t = ul_1/\nu$ , where  $l_1 \approx \lambda_w$  is the input wavelength,  $\nu$  is the kinematic viscosity and  $u$  is the r.m.s. turbulent velocity.

## 6. Summary and conclusions

Fully developed, forced upwelling fronts and their associated frontal and pinched-off eddies were produced in a laboratory tank. Streak photographs of such a flow fields were digitized and recorded. To obtain the spectral distribution of kinetic energy a variety of statistical techniques were performed on the recorded data. The results of the computations are as follows:

(i) When particle dispersion methods were employed, both the relative velocity and the quadratic diffusivity measurements indicated energy spectra of the form  $E \sim k^{-2 \pm 0.05}$  at higher wavenumbers. This spectral slope is much smaller than predicted by both the classical statistical theories and numerical simulations of two-dimensional turbulence, for the enstrophy cascade inertia range. The slope of energy spectra at lower  $k$  was consistent with  $k^{-\frac{1}{2}}$ , which was slightly less steep than predictions ( $k^{-\frac{1}{2}}$ ) given by these same theories. Although these methods produced less steep spectral slopes, it appears that two inertial subranges were generated and more

importantly suggested that the input wavenumber was close to the wavenumber of the frontal eddies ( $k_w$ ).

(ii) Direct two-dimensional Fourier transforms of the  $u'^2(x, y)$ -field were reduced to one-dimensional  $E(k)$  spectra and produced two distinct inertial ranges also; a  $k^{-\frac{2}{3}}$  spectrum at lower  $k$  and one approximately varying as  $k^{-5.5}$  at higher  $k$ . The  $k^{-\frac{2}{3}}$  result is consistent with that predicted for the inverse energy cascade inertia range, and the  $k^{-5.5}$  is similar to those obtained in numerical simulations for the enstrophy cascade in stationary flows. The two inertial ranges meet close to a wavenumber that is associated with the wavenumber of the frontal eddies ( $k_w \sim 2\pi(u_* f/g'h_0)$ ) so that  $k_w$  acts as the input wavenumber. However, these remarks should be judged cautiously since inspection of the vorticity and kinetic energy fields suggests that the high-wavenumber energy is associated with the relatively small-scale peaks of the vortex structures and probably not with any filamentary structures on the flanks of the vortices, which we cannot resolve, and which are usually thought to be responsible for the small-scale portion of the energy spectrum which evolves. By the same token, this further suggests that the usual notion of an enstrophy cascade in the fine filamentary structure around the flanks of the vortices should be viewed with some care.

(iii)  $E(k)$  distributions derived from Fourier transforms of the one-dimensional longitudinal turbulent velocity correlations revealed spectra varying like  $k^{-\frac{2}{3}}$  at lower  $k$ , which was in agreement with that obtained above. At higher values of  $k > k_w$  the slope is consistent with the results shown in §5.2.

(iv) According to classical theories and numerical simulations of two-dimensional or geostrophic turbulence, the spectral slopes ( $k^{-\frac{2}{3}}$  at  $k < k_w$  and  $k^{-5.5}$  at  $k > k_w$ ) found in the present study suggest that turbulence in our model is two-dimensional. This in turn suggests that the prototype system that we are attempting to model can also be considered to be a two-dimensional turbulent field. Since jet-like structures evolve in such a field in the laboratory then presumably they do also in the natural flow: this helps to explain the filamentary structures which transport passive markers, e.g. heat, as observed in satellite images.

(v) We have estimated the two-dimensional Kolmogorov constant ( $C$ ), within the  $k^{-\frac{2}{3}}$  inertia range. The values of  $C$  varied within the range  $2.8 < C < 3.8$ , for a rather wide range of values  $\theta_*$  and  $R_i$ . It appeared that slight increases in the value of  $C$  corresponded to an increase in the values of both  $\theta_*$  and/or  $R_0$ .

This work was supported by the ONR under the ARI on the Coastal Transition Zone. Contract No. N.00014-87-K-0809 to USC.

## REFERENCES

- AGÜÍ, J. C. & JIMENEZ, J. 1987 On the performance of particle tracking. *J. Fluid Mech.* **185**, 447–468.
- ARMÍ, L. & FLAMENT, P. 1985 Cautionary remarks on the spectral interpretation of turbulent flows. *J. Geophys. Res.* **90**, 11779–11782.
- BABIANO, A., BASDEVANT, C. & SADOURNY, R. 1985 Structure functions and dispersion laws in two-dimensional turbulence. *J. Atmos. Sci.* **42**, 941–949.
- BASDEVANT, C., LEGRAS, B., SADOURNY, R. & BELAND, M. 1981 A study of barotropic model flows: intermittency waves and predictability. *J. Atmos. Sci.* **38**, 2305–2326.
- BATCHELOR, G. K. 1953 *The Theory of Homogeneous Turbulence*. Cambridge University Press.
- BATCHELOR, G. K. 1969 Computation of energy spectrum in homogeneous two-dimensional turbulence. *Phys. Fluids Suppl.* **12**, II 233.

- BENNETT, A. F. 1984 Relative dispersions: local and nonlocal dynamics. *J. Atmos. Sci.* **41**, 1881-1886.
- BENNETT, A. F. & HAIDVOGEL, D. B. 1983 Low-resolution numerical simulation of decaying two-dimensional turbulence. *J. Atmos. Sci.* **40**, 738-748.
- BRACHET, M. E., MENEGUZZI, M., POLITANO, H. & SULEM, P. L. 1988 The dynamics of freely decaying two-dimensional turbulence. *J. Fluid Mech.* **194**, 333-349.
- BRACHET, M. E., MENEGUZZI, M. & SULEM, P. L. 1986 Small-scale dynamics of the high Reynolds number two-dimensional turbulence. *Phys. Rev. Lett.* **57**, 683-686.
- BROWN, P. S. & ROBINSON, G. D. 1979 The variance spectrum of tropospheric winds over Eastern Europe. *J. Atmos. Sci.* **36**, 270-286.
- CHARNEY, J. G. 1971 Geostrophic turbulence. *J. Atmos. Sci.* **28**, 1087-1095.
- CHIA, F. R., GRIFFITHS, R. W. & LINDEN, P. F. 1982 Laboratory experiments on fronts. Part II. The formulation of cyclonic eddies at upwelling fronts. *Geophys. Astrophys. Fluid Dyn.* **19**, 189-206.
- DEEM, G. S. & ZABUSKY, N. J. 1971 Ergodic boundary in numerical simulations of two-dimensional turbulence. *Phys. Rev. Lett.* **27**, 396-399.
- DUBOIS, M. 1975 Large-scale kinetic energy spectra from Eulerian analysis of Eole wind data. *J. Atmos. Sci.* **32**, 1838-1847.
- FOERNBERG, B. 1977 A numerical study of two-dimensional turbulence. *J. Comput. Phys.* **25**, 1-31.
- FOX, D. G. & ORSZAG, S. A. 1972 Inviscid dynamics of two-dimensional turbulence. *Natl Center Atmos. Res. MS.* 72-80.
- FRISCH, U. & SULEM, P. L. 1984 Numerical simulation of inverse cascade in two-dimensional turbulence. *Phys. Fluids* **27**, 1921-1923.
- GAGE, K. S. 1979 Evidence for a  $K^{-1}$  law inertial range in a mesoscale two-dimensional turbulence. *J. Atmos. Sci.* **36**, 1950-1954.
- GRIFFITHS, R. W. & HOPFINGER, E. J. 1984 The structure of mesoscale turbulence and horizontal spreading at ocean fronts. *Deep-Sea Res.* **31**, 245-269.
- GRIFFITHS, R. W. & LINDEN, P. F. 1981 The stability of vortices in a rotating stratified fluid. *J. Fluid Mech.* **195**, 283-316.
- GRIFFITHS, R. W. & LINDEN, P. F. 1982 Laboratory experiments on fronts. Part I: Density driven boundary currents. *Geophys. Astrophys. Fluid Dyn.* **19**, 159-187.
- HAIDVOGEL, D. B. & KEFFER, T. 1984 Tracer dispersal by midocean mesoscale eddies. I: Ensemble statistics. *Dyn. Atmos. Oceans* **8**, 1-40.
- HERRING, J. R. 1980 Statistical theory of quasi-geostrophic turbulence. *J. Atmos. Sci.* **37**, 969-977.
- HERRING, J. R. & McWILLIAMS, J. C. 1985 Comparison of direct numerical simulation of two-dimensional turbulence with two-joint closure: the effects of intermittency. *J. Fluid Mech.* **153**, 229-242.
- HERRING, J. R., ORSZAG, S. A., KRAICHNAN, R. H. & FOX, D. G. 1974 Decay of two-dimensional homogeneous turbulence. *J. Fluid Mech.* **66**, 417-444.
- HEYER, J. M. & SADOURNY, R. 1982 Closure modeling of fully developed baroclinic instabilities. *J. Atmos. Sci.* **39**, 707-721.
- IMAICHI, K. & OHMI, K. 1983 Numerical processing of flow-visualization pictures - measurement of two-dimensional vortex flow. *J. Fluid Mech.* **129**, 283-311.
- JULIAN, P. R., WASHINGTON, W. M., HEMBRE, L. & RIDLEY, C. 1970 On the spectral distribution of large-scale atmospheric kinetic energy. *J. Atmos. Sci.* **27**, 376-387.
- KAO, S. K., JENNE, R. L. & SAGENDOLF, J. F. 1970 The kinetic energy of large-scale atmospheric motion in wavenumber-frequency space: II. Mid-Troposphere of the southern Hemisphere. *J. Atmos. Sci.* **27**, 1008-1020.
- KILLWORTH, P. D., PALDOR, N. & STERN, M. 1984 Wave propagation and growth on a surface front in a two-layer geostrophic current. *J. Mar. Res.* **42**, 761-785.
- KOLMOGOROV, A. N. 1941 Dispersion of energy in locally isotropic turbulence. *CR Acad. Sci. URSS* **32**, 16.

- KRAICHNAN, R. H. 1967 Inertial ranges in two-dimensional turbulence. *Phys. Fluids* **10**, 1417-1423.
- KRAICHNAN, R. H. 1975 Statistical dynamics of two-dimensional flow. *J. Fluid Mech.* **67**, 155.
- LEITH, C. E. 1968 Diffusion approximation for two-dimensional turbulence. *Phys. Fluids* **11**, 671-673.
- LESIEUR, M. 1987 *Turbulence in Fluids*. Martinus Nijhoff.
- LILLY, D. K. 1969 Numerical simulation of two-dimensional turbulence. High-speed computing in fluid dynamics. *Phys. Fluid Suppl.* **12**, II 240.
- LILLY, D. K. 1971 Numerical simulation of developing and decaying two-dimensional turbulence. *J. Fluid Mech.* **45**, 395-415.
- LILLY, D. K. 1972 Numerical simulation studies of two-dimensional turbulence. I. *Geophys. Fluid. Dyn.* **3**, 289.
- MAXWORTHY, T. 1989 The dynamics of two-dimensional turbulence. In *Proc. Conf. on the Oceanography of Sea Straits, les Arcs, France*.
- MAXWORTHY, T., CAPERAN, P. & SPEDDING, G. R. 1987 Two-dimensional turbulence and vortex dynamics in a stratified fluid. In *Proc. Third Intl. Conf. on Stratified Flows, Pasadena, California*.
- MCWILLIAMS, J. C. 1984 The emergence of isolated coherent vortices in turbulent flow. *J. Fluid Mech.* **146**, 21-43.
- MOREL, P. & LARCHEVEQUE, M. 1974 Relative dispersion for constant-level balloons in the 200 mb general circulation. *J. Atmos. Sci.* **31**, 2189-2196.
- MORY, M. & HOPFINGER, E. J. 1986 Structure functions in a rotationally dominated turbulent flow. *Phys. Fluids* **29**, 2140-2146.
- NARIMOUSA, S. & MAXWORTHY, T. 1985 Two-layer model of shear driven coastal upwelling in the presence of bottom topography. *J. Fluid Mech.* **159**, 503-531.
- NARIMOUSA, S. & MAXWORTHY, T. 1986 Effects of a discontinuous surface stress on a model of coastal upwelling. *J. Phys. Oceanogr.* **16**, 2071-2083.
- NARIMOUSA, S. & MAXWORTHY, T. 1987a Coastal upwelling on a sloping bottom: The formation of plumes, jets and pinched-off cyclones. *J. Fluid Mech.* **176**, 169-190.
- NARIMOUSA, S. & MAXWORTHY, T. 1987b Effects of coastline perturbations on coastal currents and fronts. *J. Phys. Oceanogr.* **17**, 1296-1303.
- NARIMOUSA, S. & MAXWORTHY, T. 1989 Application of a laboratory model to the interpretation of satellite and field observations of coastal upwelling. *Dyn. Atmos. Oceans* **13**, 1-46.
- NARIMOUSA, S., MAXWORTHY, T. & SPEDDING, G. R. 1987 Structure of meso-scale baroclinic turbulence. *Sixth Symp. on Turbulent Shear Flows, Toulouse, France, September 7-9*.
- NASTROM, G. D. & GAGE, K. S. 1983 A first look at wavenumber spectra from GASP data. *Tellus* **35**, 383-388.
- PHILLIPS, N. A. 1954 Energy transformations and meridional circulations associated with simple baroclinic waves in a two-level, quasi-geostrophic model. *Tellus* **6**, 273-286.
- RIGNOT, E. J. M. & SPEDDING, G. R. 1988 Performance analysis of automated image processing and grid interpolation techniques for fluid flows. *University of Southern California, Department of Aerospace Engineering Internal Rep.* USCAE 143.
- SAFFMAN, P. G. 1971 On the spectrum and decay of random two-dimensional vorticity distributions at large Reynolds numbers. *Stud. Appl. Maths* **50**, 377-383.
- SALMON, R. 1978 Two-layer quasi-geostrophic turbulence in a simple case. *Geophys. Astrophys. Fluid Dyn.* **10**, 25-51.
- SANTANGELO, P., BENZI, R. & LEGRAS, B. 1989 The generation of vortices in high-resolution, two-dimensional decaying turbulence and the influence of initial conditions on the breaking of self-similarity. *Phys. Fluids A1*, 1027-1034.
- SIGGIA, E. D. & AREF, H. 1981 Point vortex simulation of the inverse cascade in two-dimensional turbulence. *Phys. Fluids* **24**, 171-173.
- SOMMERIA, J. 1986 Experimental study of the two-dimensional inverse energy cascade in a square box. *J. Fluid Mech.* **170**, 139-168.
- TOWNSEND, A. A. 1976 *Structure of turbulent Shear Flow*. Cambridge University Press.

## EFFECTS OF COASTLINE PERTURBATIONS ON COASTAL CURRENTS AND FRONTS

S. Narimousa & T. Maxworthy<sup>1</sup>

Department of Mechanical Engineering  
University of Southern California  
Los Angeles, CA 90089-1453

### ABSTRACT

Surface-stress driven coastal currents and upwelling were produced around the outer edge of a cylindrical tank having a conical bottom and protuberance representing a cape. A large standing wave formed at a distance  $D_{sw} \approx 2R_c \theta_*^{-4} (\lambda_s/R_c)^{-2}$  downstream of the cape, where  $R_c$  is the radius of the cape, and  $\theta_* = gh_0/u_*f\lambda_s$  (where  $g' = g\delta\rho$  is the reduced gravity,  $h_0$  is the initial depth of the top layer,  $u_*$  is the friction velocity,  $f$  is the Coriolis parameter and  $\lambda_s$  is the final width of the upwelling front at the surface). The extreme offshore extent of this stable wave was  $A_{sw} \approx 3.4 R_c$ . The presence of the cape caused the flow downstream to diverge horizontally. When the upwelled fluid reached this divergence it was distorted by it and formed a thin filament extending a considerable distance offshore.

### INTRODUCTION

Routine satellite infrared (I.R.) images of the west coast of North America have revealed some very interesting evolving structures and fronts in the surface waters associated with wind driven coastal upwelling. Coastline perturbations, bottom topography and an off-shore curl in the surface wind-stress are among the important factors which are thought to influence these wind driven coastal currents and fronts, and may produce some of the features which are seen in many of these satellite I.R.-images. It is known that the presence of bottom topography (a ridge) is one of the primary causes of stationary, upwelling maxima (see Preller and O'Brien (1980), Brink et al. (1980), Narimousa and Maxworthy (1985 and 1986a) [hereafter NM1 and NM2, respectively]). In NM2 we showed also that when a field of off-shore eddies interacted with the upwelling front it caused upwelled water to be transported off-shore in the form of jets between the eddies. In Narimousa and Maxworthy (1986b), hereafter NM3, we demonstrated that, even in the absence of bottom topography and a field of off-shore eddies large amplitude frontal instabilities could spawn off-shore propagating cyclones which when they interacted with the frontal anticyclones could produce meandering jets which also transported the bottom upwelled water far off-shore.

In the present paper we study yet another possible cause for the appearance

<sup>1</sup>Also Department of Aerospace Engineering, USC, Los Angeles, CA 90089-0192 and Earth & Space Sciences Division, Jet Propulsion Lab, Pasadena, CA

of strongly meandering flow, that is the effect of coastline perturbations or capes. Peffley and O'Brien (1976) investigated this possibility and suggested that the observed upwelling maximum at a cape was not due to the presence of the cape itself, but it was a result of the interaction of the associated bottom topography with the upwelling circulation. In NM1, we noted that the results of our preliminary experiments with capes were in agreement with Peffley and O'Brien's (1976) calculations. In the present paper, we now make a more complete and detailed study of the effects of the capes on upwelling circulation and find some similarities and some differences from the results of NM1 and NM2. Although in our present experiments the upwelling maximum no longer occurs at the cape, the influence of the cape on the flow field near and downstream of it is very interesting and may help to answer some of the important questions raised by several investigators. As in the experiments with bottom topography, here also we find that there is a direct relationship between presence of a cape and the observed offshore jets, either due to the instability of the downstream standing waves, or to a flow divergence created in the neighborhood of the cape. In order to investigate how large a cape should be before it can significantly influence the coastal current and front, we varied the size of the cape. In NM1 we found that the distance of the maximum of a large downstream standing wave from the ridge,  $D_{sw}$  could be estimated from  $D_{sw}/\lambda_w \approx 0.2 \theta_*$  where  $\theta_* = g h_0 / u_* f \lambda_s$ . In the present case also a large standing wave was formed downstream of the cape, and we found that  $D_{sw}/\lambda_s$  not only depended on  $\theta_*$ , but that it was smaller, the smaller the size of the cape. We also give an experimental estimate for the amplitude of the first stable, large, downstream standing wave from the coastline,  $A_{sw}$ , and for of the velocities within the jet flow in front of and downstream of the cape.

#### THE EXPERIMENT

For the present study we use the same basic apparatus as that of NM1, NM2 and NM3 to study the effects of coastline perturbations on coastal currents and fronts. For a detailed discussion of the experimental apparatus the reader is referred to NM1, only a brief description need be given here.

Two layers of salt water of slightly different densities were brought to solid-body counter-clockwise rotation inside a cylindrical tank (90 cm in diameter and 22 cm in depth) having a conical bottom (figure 1). An obstacle manufactured by cutting a cylinder of radius  $R_c$  in half through its vertical axis, was placed vertically at the wall to produce a cape (figure 1). For the purpose of this study we used three different sized capes, called L, M and S, the radii of which were  $R_c = 8.25, 4.5$  and  $3$  cm, respectively. The surface of the upper fluid was in contact with a circular, smooth disc, which as it rotated applied a stress to this surface in order to model the wind stress at the air-sea interface. In order to produce upwelling, the disc was rotated in a clockwise direction, i.e., in a direction opposite to that of the basic rotation of the tank. The direction of the current and the upwelling frontal movement were observed by placing small neutrally buoyant particles in the front and recording their motion by streak photography. The direction of motion of these particles was found by firing an electronic flash at the beginning of the time exposure.

around  
erance  
 $D_{sw} =$   
e, and  
pth of  
is the  
extent  
e flow  
rgence  
istance

America  
surface  
bations,  
ng the  
currents  
any of  
ography  
Preller  
1986a)  
a field  
water  
rimousa  
absence  
frontal  
eracted  
ported

earance

89-0192

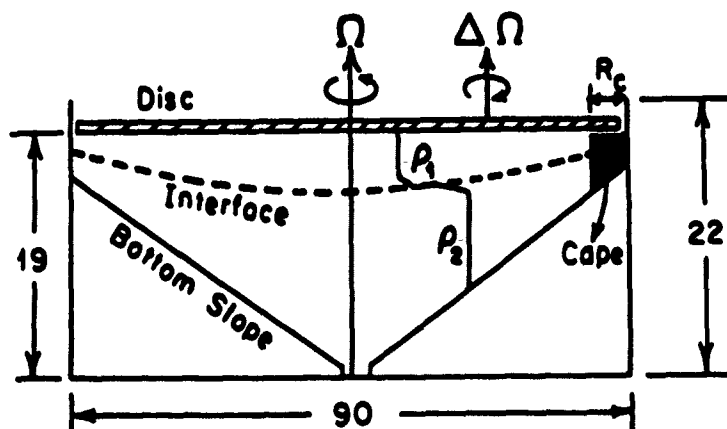


Figure 1. Cross section of the experimental apparatus at the cape (lengths measured in centimeters).

In our previous work (NM1, NM2 and NM3) the presence of offshore jets was clearly shown by this technique. However, since we believed that these jets were responsible for carrying upwelled water far offshore, we demonstrated this by marking the upwelled water using a white, liquid, Titanium dye. The dye was usually released near the wall of the tank within the upwelled water, so that after one or two rotation periods it reached the upwelled front some distance away from the wall. The interaction of the dye (presenting upwelled flow near the surface) with the upwelling front, revealed the offshore jets and eddies clearly so they could be recorded photographically. In all cases density of the dye was chosen so that it remained in the surface layer.

The ranges of parameters were as follows; initial depth of the top layer  $2.5 \leq h_0 \leq 2.95$  cm; density difference between the two layer ( $\delta\rho = \rho_2 - \rho_1$ ),  $.02 \leq \delta\rho_0 \leq .035$  gcm<sup>-3</sup>; reduced gravity between the two layer  $19.6 \leq g' \leq 4$  cms<sup>-2</sup> (where  $g' = g\delta\rho_0$ , and  $g = 981$  cms<sup>-2</sup>, is the acceleration of gravity); the Coriolis parameter  $1.67 \leq f \leq 5$  s<sup>-1</sup>; the friction velocity  $.28 \leq u_* \leq .62$  cm/s; the final width of the upwelled water at surface.  $2.7 \leq \lambda_s \leq 17$  cms and the control parameter  $2.2 \leq \theta_* \leq 37$ .

#### A GENERAL DESCRIPTION OF THE FLOW FIELD

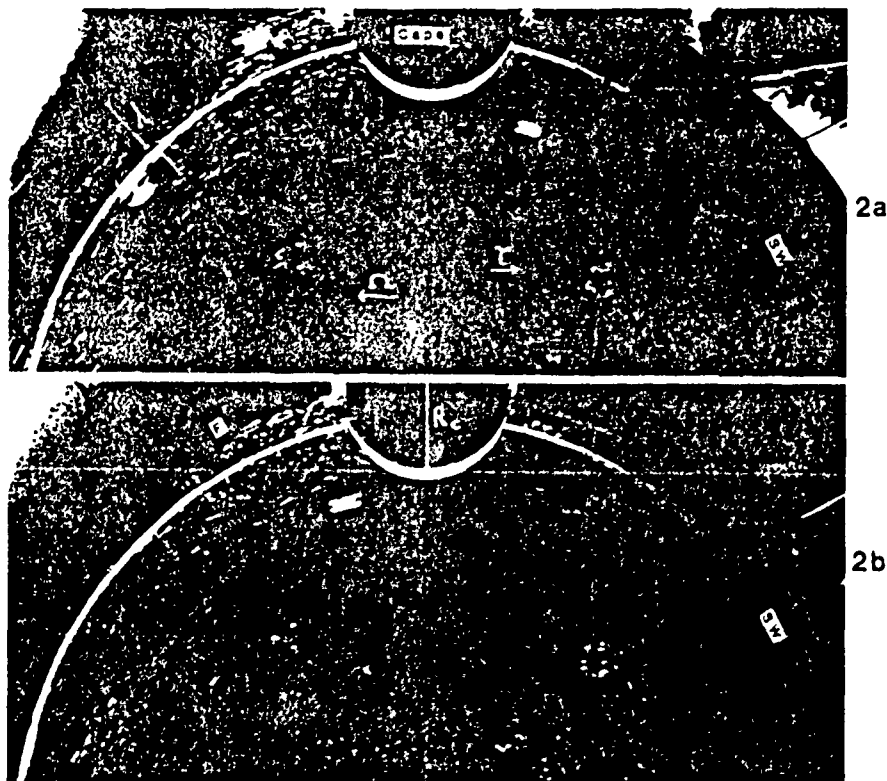
In the present experiments the observations of the flow upstream of the capes has some similarity to those already described in NM1 and NM3. Here, however, the first sign of upwelled water at surface always occurred at the upstream side of the capes in the form of a narrow band of width  $\lambda$ . This is different from the observations of NM1 and NM2 where the first sign of the upwelled water at the surface always occurred at the bottom topography itself (see NM1). However, at a later time of a given experiment, when the width  $\lambda$  increased to values greater than  $R_c$ , the bottom water also appeared at the surface near the cape (see figure 2). Unlike NM1 and NM2, where an upwelling maximum always occurred at the bottom topography (see NM1). The presence of a cape did not produce a clear-cut upwelling maximum (see also Peffley and O'Brien (1976)). The reason for this is that the variable bottom topography is not included in front of the cape in the present experiments, since here we are dealing with the effects of a cape alone. Here when the upstream fluid columns reached the cape they

were  
veloci  
consi  
As th  
The f  
later  
off-sh  
wave  
a div  
we sh  
the u  
limitat  
greate  
a nun  
still i  
instea  
smalle  
the ar  
from t  
the up  
they  
within  
only t  
becam  
be abli

were forced off-shore toward deeper water, where they were stretched and their velocity increased. This stretching produced a jet flow which extended a considerable distance downstream in the form of standing waves (see figure 5). As the value of  $\theta_0$  was increased the standing waves formed farther downstream. The first standing wave was the largest and the most significant one which, at later time of the experiments for low values of  $\theta_0$ , became unstable and grew off-shore to form a closed cyclone. This cyclone sometimes detached from the wave crest and propagated further off-shore (see figure 5). The capes also produced a diverging flow which generated long, off-shore filaments of upwelled water, as we shall see in detail later.

In the discussion above we considered the largest cape (L) and we allowed the upwelled front to migrate as far from the tank wall as our experimental limitations allowed. For this cape the maximum value of  $\lambda = \lambda_s$  was slightly greater than twice the radius of the cape  $R_c$ . In nature the width  $\lambda$  is sometimes a number of times greater than  $R_c$ , and it is important to know if the cape can still influence the front. Since we were limited in our choice of  $\lambda_s$ , we chose instead to use smaller capes. The flow field upstream, on and downstream of the smaller cape is similar to that already discussed above for the L-cape, only here the amplitude, the wavelength and the distance of the downstream standing waves from the cape were considerably smaller.

As in our previous experiment, travelling baroclinic waves also appeared at the upwelled front upstream of the capes. When these waves reached the cape they were usually absorbed by the jet flow created by the cape and the fluid within them originally was distorted by the flow-field created by the cape. The only time that the baroclinic waves were able to pass the cape was when they became pinched-off from the upstream front and they were far enough from it to be able to pass the cape undisturbed.





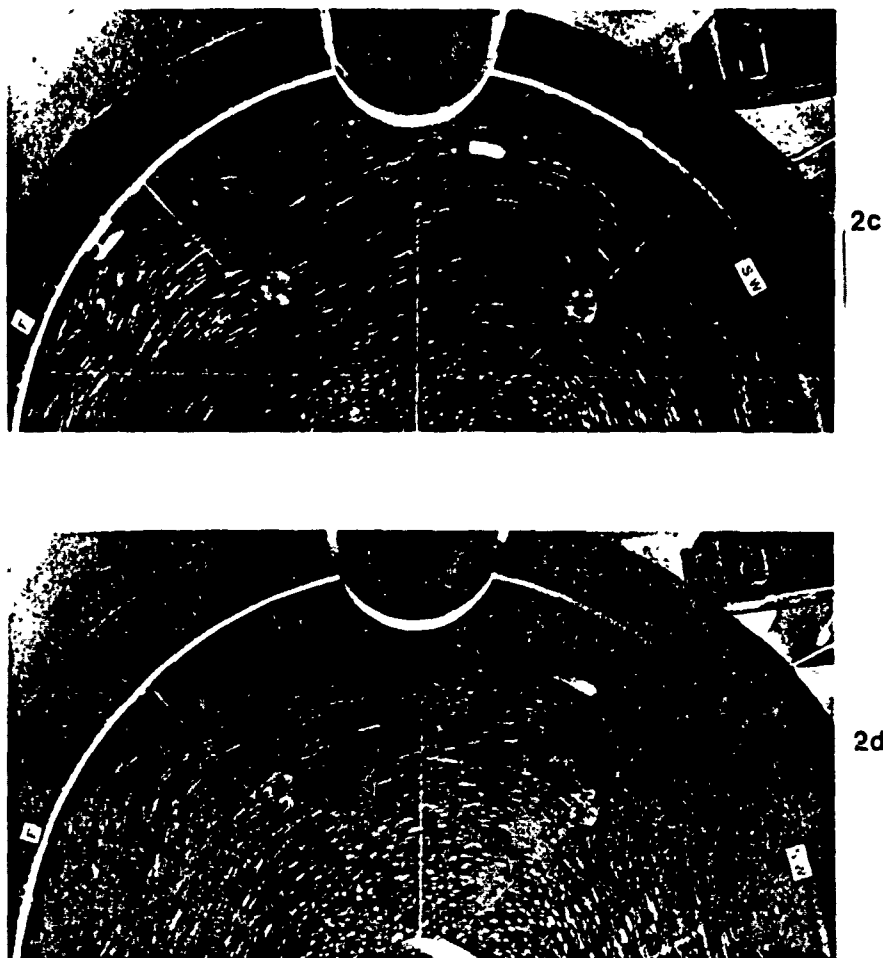


**Figure 2.** A set of streak photographs with a 0.5 sec time exposure for parameter values of  $R_c = 8.25$  cm,  $h_0 = 2.75$  cm,  $\delta\rho_0 = .035$  g/cm<sup>3</sup>,  $f = 2.28$  rad/sec,  $\Delta\Omega = .21$  rad/sec,  $\lambda_s = 9.3$  cm,  $u_* = .52$  cm/sec and  $\theta_* = 8.6$ . Photograph (a) taken after  $t \approx 133$  sec,  $R_c > \lambda_s$ , shows no upwelling at front of the cape, while there is upwelling immediately adjacent to the upstream and downstream sides of the cape. Also notice the position of the downstream standing wave caused by the cape and the width of the upwelling upstream of the cape  $\lambda$ . Photograph (b) taken after  $t \approx 233$ ,  $R_c > \lambda_s$ , shows an upwelling at front of the cape. This photograph shows a collision of an upstream frontal wave (F) with the cape. Photograph (c) taken after  $t \approx 409$  sec.,  $R_c = \lambda_s$ , shows no upwelling at the cape yet. Photograph (d) taken after  $t \approx 770$  sec,  $R_c < \lambda_s$ , now shows upwelling at the cape.

M  
the fr  
barocli  
when i  
from t  
the det  
Ir  
metho  
waves  
as a  
for gi  
be se  
approx  
data  
follow

Fig  
down  
(2, 1)

## RESULTS

Measurements from the present study show that the speed of migration of the front upstream of the cape  $u_f$  is  $u_f/u_* \sim \theta_*^{-0.5}$ , the diameter of the circular baroclinic waves  $\lambda_w$  is  $\lambda_w/\lambda_s \sim \theta_*$  and that these waves first appear at the front when it has moved a distance  $\lambda_f$  given by  $\lambda_f/\lambda_s \sim \theta_*^{-0.5}$ . Since these measurements from upstream are the same as those given already in NM3, we will not repeat the details here, but refer the reader to that paper.

In order to describe the wave field downstream of the cape we use the same method as NM1 in which the distance of the peak of the downstream standing waves  $D_{sw}$  from the ridge was measured. In figure 3 we show a plot of  $D_{sw}/\lambda_s$  as a function of  $\theta_*$  for our S, M and L capes. These results clearly show that for given value of  $\theta_*$  the value of  $D_{sw}$  depends on the size of the cape. It can be seen in figure 4, that independent of the size of the cape, the values of  $D_{sw}/\lambda_s$  approximately follow the same power law behavior with  $\theta_*$ . That is, although the data on figure 3 did not collapse for all size capes, but for each individual cape follows the relationship

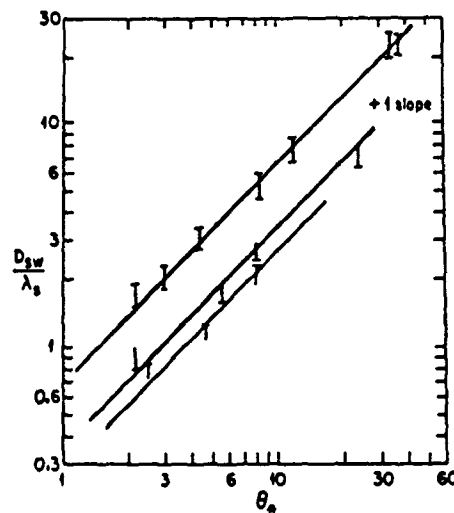


Figure 3. The variation of  $D_{sw}/\lambda_s$  with  $\theta_*$ , where  $D_{sw}$  is the distance of the downstream standing wave from the head of the cape. In this figure the symbols ( $\Delta$ ,  $\square$ ,  $\circ$ ) indicate the data for L, M and S-cape respectively.

$$\frac{D_{sw}}{R_c} \sim \theta_* \quad (1)$$

Cross plotting these data indicated a functional dependence of  $D_{sw}/R_c$  on  $\theta_*$  and  $\lambda_s/R_c$  as shown in figure 4 for all capes, which allows us to write, to within experimental accuracy:

$$\frac{D_{sw}}{R_c} = 2\theta_*^4 \left( \frac{\lambda_s}{R_c} \right)^{.2} \quad (2)$$

The other important quantity to measure is the amplitude of the standing waves before they become unstable and grow off-shore. We defined this stable amplitude,  $A_{sw}$  to be the extreme off-shore distance of the standing wave crest from the coast as shown by particle streaks. Our measurements of the values of  $A_{sw}$  for different capes indicate that  $A_{sw}$  is independent of the values of  $\theta_*$  and to within an error of about 10% to 15% all experiments agree with:

$$\frac{A_{sw}}{R_c} = 3.4 , \quad (3)$$

Once again we should mention that (3) is only good for when the waves are stable, because at lower values of  $\theta_* < 6$  these waves at later time of the experiments (100  $\Omega$ ) usually grew off-shore to sometimes eject a cyclone.

We also measured the mean velocity ( $V$ ) within the meandering jet flow which was created by the cape. For all capes and with an error of about 10% we found,

$$\frac{V}{U} = 1.2 , \quad (4)$$

where  $U$  is the mean velocity of the top layer measured at the upwelled front.

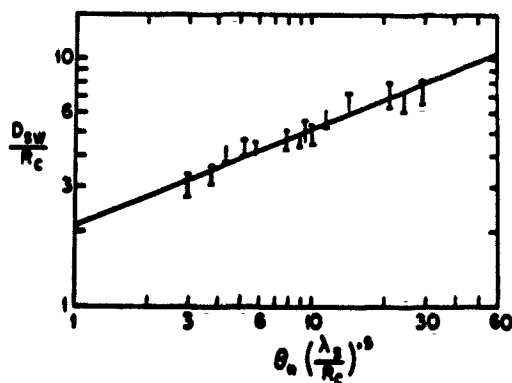


Figure 4. The variation of  $D_{sw}/R_c$  with  $\theta_* (\lambda_s/R_c)^{.5}$ . The symbols (L, M, S) indicate the data for L, M and S-cape respectively.

In this created by a demonstrate injection me view also an

At valu one is remin After reachi was complet However, w streaks show the same tir carried by t continued, t while it drift of the upwe the downste such filame the standing for short tir standing w

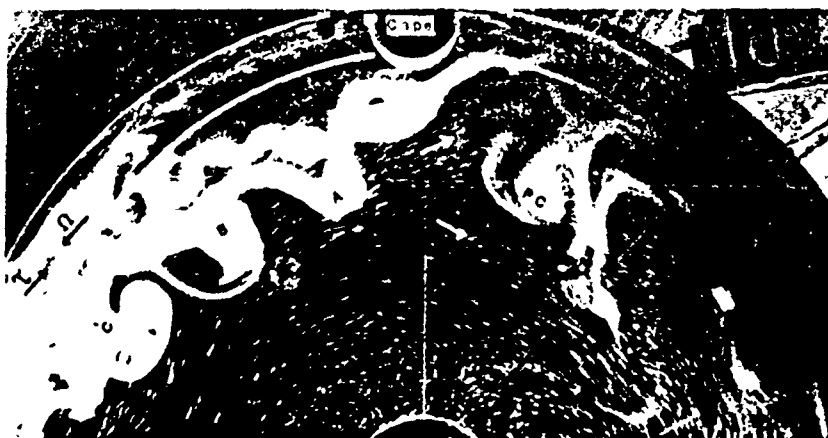
The d During the usually bec cyclone co This pinche to produce detached fr off-shore a pinched-of attached to downstre upwelled v

## OFFSHORE MOVEMENT OF UPWELLED FLUID

In this section, we look for those conditions for which the flow field created by a cape, can transfer the bottom upwelled water off-shore. In order to demonstrate such transportation of the coastal water off-shore, we used the dye injection method as described in §1. The photographs of this section are plain view also and the dye is released near the surface from the sources at the wall.

At values of  $\theta_* < 6$  a diverging flow was produced downstream of a cape. Here one is reminded of similar rotor-types of flow in a stratified fluid (Long 1953). After reaching a maximum width, the flow began to converge and this convergence was completed near the crest of the downstream standing wave (see figure 5). However, when the upstream travelling baroclinic waves reached a cape, the particle streaks showed that the waves were absorbed by the jet flow of the cape. At the same time the flow divergence caused the upwelled surface water originally carried by the waves to advect in the off-shore direction. As this advection continued, the upwelled water extended farther off-shore and became thinner, while it drifted downstream. Eventually, thin, long off-shore-extending filaments of the upwelled water were produced (see figure 5). When these filaments reached the downstream standing wave, they became distorted by it. At high values of  $\theta_*$  such filaments did not occur. On the other hand, at very low values of  $\theta_*$  when the standing waves were formed very close to the cape the filaments were observed for short time only, because they were quickly absorbed by the nearby, downstream standing wave.

The downstream standing wave itself can transport upwelled fluid offshore. During the late times of a given experiment and at low values of  $\theta_*$  this wave usually became unstable and propagated in the off-shore direction. Eventually a cyclone containing bottom water pinched-off from the crest of the standing wave. This pinched-off cyclone sometimes remained attached to the standing wave crest to produce a permanent cyclone off-shore. Under other circumstances it sometimes detached from the crest of the standing wave to transport the coastal water off-shore and at the same time allowing the standing wave to produce a new pinched-off cyclone. During the time when the pinched-off cyclone remained attached to the wave crest, it interacted with the anti-cyclone adjacent to the downstream edge of the cape to produce an off-shore jet flow, which carried the upwelled water off-shore also.



5a

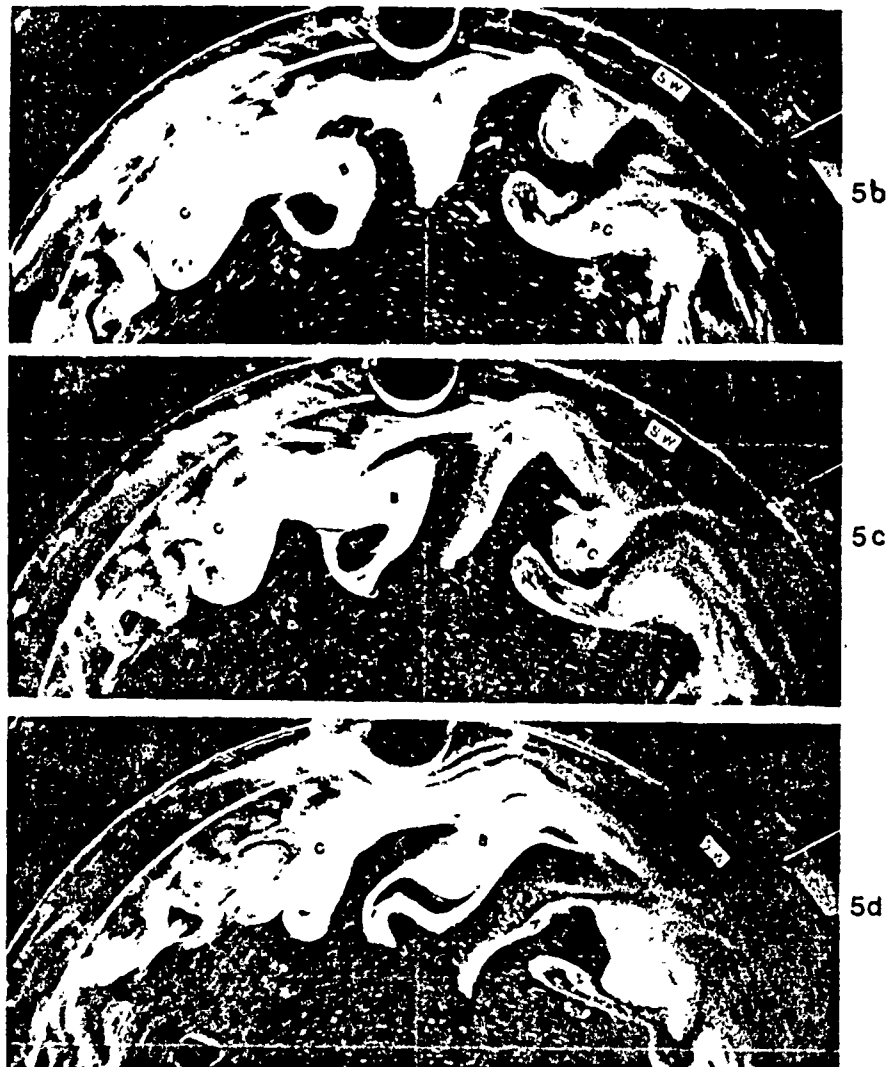


Figure 5. A set of streak and dye photographs with a 0.5 time exposure, for parameter values of  $R_c = 4.5$  cm,  $h_0 = 2.55$  cm,  $f = 3.52$  rad/sec.,  $\Delta\Omega = .137$  rad/sec.,  $\lambda_s \approx 12$  cm,  $u_* \approx .32$  cm/sec. and  $\theta_* \approx 5.5$ . Photograph (a) taken after  $t \approx 615$  sec., shows the upstream waves (A,B,C) as they are revealed by both particle streaks and dye. Also notice the downstream standing (SW) or upwelling center. The flow divergence in this photograph is clearly shown just downstream of the cape, as indicated by white arrows. Photograph (b) taken 2 rotation periods after (a), shows (A) at the cape being stretched in the off-shore direction by the flow divergence. Photograph (c) taken one rotation period later than (b) shows that (A) has become thinner with a sharp head, while (B) is at the cape. Photograph (d) taken 2 rotation periods later shows that (A) is much thinner and has formed a filament extending a considerable distance off-shore. The same process that acted upon (A) is now affecting (B).

Here  
our labor  
have a sig

I.  
side of th

II.  
distance  
amplitude  
 $A_{sw} = 3.4$   
estimated

III. A  
standing  
stationary  
detached  
off-shore

IV.  
flow just  
parcels to

Long, R. I.  
investiga

Narimous  
in the pr

Narimous  
model of

Narimous  
formation

Peffley, M.  
off Orego

Preller, R.  
Peru\*, J.

## SUMMARY and CONCLUSIONS

Here we have examined the effect of capes on coastal currents and fronts in our laboratory tank and we found that capes, like bottom topography (NM1), can have a significant effect. Our results can be summarized as follows.

I. The first sign of upwelling always occurred adjacent to the upstream side of the cape.

II. A large standing wave was produced downstream of the capes, and its distance from the capes  $D_{sw}$ , can be estimated from  $D_{sw} = R_c \theta_*^4 (\lambda_s / R_c)^2$ . The amplitude of the stable standing wave  $A_{sw}$  for any cape can be estimated from  $A_{sw} = 3.4 R_c$ , while the typical velocities within these standing waves can be estimated from  $V = 1.2 U$ .

III. At low  $\theta_*$  values of  $\theta_*$ , after many rotation periods, the stable downstream standing wave became unstable and propagated in off-shore direction to produce a stationary off-shore cyclone, which sometimes (at small value of  $\theta_*$ ) this cyclone detached from the standing wave and transported the upwelled water farther off-shore.

IV. A significant feature of the present study is the creation of a diverging flow just downstream of the cape, which was able to distort approaching water parcels to produce long, thin off-shore filaments of upwelled water.

## REFERENCES

- Long, R. R., "Some aspects of the flow of stratified fluids I. A theoretical investigation", Tellus, 5, 42, 1953.
- Narimousa, S. and Maxworthy, T., "Two-layer model of shear driven coastal upwelling in the presence of bottom topography", J. Fluid Mech., 159, 503-531, 1985.
- Narimousa, S. and Maxworthy, T., "Effects of a discontinuous surface stress on a model of coastal upwelling", J. P. O. (in press), 1986a.
- Narimousa, S. and Maxworthy, T., "Coastal upwelling on a sloping bottom: the formation of plumes, jets and pinched-off cyclones", J.F.M. (in press), 1986b.
- Peffley, M. B. and O'Brien, J. J., "A three dimensional simulation of coastal upwelling off Oregon", J. Phys. Oceanogr., 6, 164-180, 1976.
- Preller, R., O'Brien, J. J., "The influence of bottom topography on upwelling off Peru", J. Phys. Oceanogr., 10, 1377-1398, 1980.

**Experiments On Forced, Quasi-Two-Dimensional Turbulence at Upwelling Fronts**

**S. NARIMOUSA<sup>a</sup>, T. MAXWORTHY<sup>β</sup>, and G. R. SPEDDING<sup>γ</sup>**

<sup>a</sup> *University of Southern California  
Los Angeles, California 90089-1453, USA*

<sup>β</sup> *University of Southern California  
Los Angeles, California 90089-1453, USA*

<sup>γ</sup> *University of Southern California  
Los Angeles, California 90089-1453, USA*

*Turbulence and coherent structures  
M. Lesieur and O. Métais, eds.  
Selected papers from "Turbulence 89: organized structures  
and turbulence in fluid mechanics"  
Grenoble, 18-21 September 1989  
© Kluwer academic publishers, 1989*

### 1. Abstract

Coastal upwelling fronts have been generated around the outer edge of a cylindrical tank, filled with a two-layer fluid system and driven by a surface stress. Initially, an axisymmetric front was observed which subsequently became unstable to small baroclinic eddies. These eddies continued to grow until, eventually, they reached an equilibrium size. Under some circumstances, cyclonic eddies pinched-off from the fully developed front and moved away from the mean position of the front into the fluid interior. Streak photographs of the fully-developed, flow field were digitized to generate a velocity field interpolated onto a regular grid. A direct two-dimensional FFT was performed on the turbulent kinetic energy deduced from such images and one-dimensional energy ( $E$ ) wavenumber ( $K$ ) spectra were extracted. Consistently,  $K^{-5/3}$  energy spectra were found at lower  $K$  and approximately  $K^{-5}$  spectra at higher  $K$ . In any given experiment, the two spectral slopes meet close to a wavenumber  $K_w = 2\pi/\lambda_w$  (where  $\lambda_w$  is the mean diameter of a frontal eddy). According to classical theories,  $K_w$  would be the input wavenumber and the range of  $K$  with a  $K^{-5/3}$  spectrum the inverse energy cascade which yielded a Kolmogorov constant ( $C$ ) that varied within the limits  $3.6 \leq C \leq 6.3$ . The approximately  $K^{-5}$  range, which is much steeper than that predicted by the theories, is consistent with those found frequently in numerical experiments.

### 2. Introduction

The pioneering studies of 2D turbulence were concerned with the structure of atmospheric meso and large scale eddies, which were thought to have 2D structure. In the case of three-dimensional turbulence, Kolmogorov's (1941) cascade hypothesis indicated an equilibrium inertial subrange in which kinetic energy cascaded from low to higher wavenumber ( $K$ ), and the energy spectra took the form  $E \sim K^{-5/3}$ . In case of 2D turbulence there is a second invariant of motion, the enstrophy, which is defined as half of the squared vorticity  $\omega^2/2$ . This led Kraichnan (1967) and Leith (1968) to propose, both a direct enstrophy and an inverse energy cascade inertial range for the case of forced 2D turbulence. They found, that  $E \sim K^{-5/3}$  in the inertia range in which energy cascaded to lower  $K$  (an inverse cascade) and an  $E \sim K^{-3}$  inertial range in which enstrophy cascaded to higher  $K$ . Batchelor (1969) found the  $K^{-3}$  range for the case of a freely-decaying 2D turbulence, which was consistent



with Kraichnan's and Leith's energy spectrum for the enstrophy cascade range. Studies of three-dimensional, quasi-geostrophic turbulence (Charney 1971, Salmon 1978, Herring 1980 and Heyer and Sadourny 1982) indicated the existence of two inertial ranges  $K^{-3}$  and  $K^{-5/3}$ , which was similar to spectral characteristics of 2D turbulence (also see Lesieur (1987) section 5.5).

One important motivation that triggered this study were observations of thin, long off-shore extending, cold filaments in satellite (IR) images taken of the west coast of the USA during coastal upwelling episodes (Narimousa and Maxworthy (1989)). Intense turbulent jets or rivers which are believed to transport the cold upwelled water far off-shore, have been recognized as a possible source for generating these filaments. Narimousa and Maxworthy (1985, 1986 and 1987a,b) observed, in the laboratory, that the turbulent jets were often associated with off-shore eddies which could be generated in a variety of ways: (a) large amplitude instability of standing waves generated by coastal perturbations; (b) large amplitude baroclinic instability of the front itself; and (c) production of eddies due to the presence of an off-shore curl in the surface stress. In all cases, interaction between the off-shore eddies produced the off-shore jets, which then transported the upwelled water off-shore. If the structure of such eddy fields obey the laws of 2D or geostrophic turbulence, then the intense turbulent rivers which seem to thread through such eddy fields, and are responsible for transport of material across the eddy field, would seem to be an important characteristic of such flows.

In the present study we employed the experiments of Narimousa and Maxworthy (1987a) to investigate the structure of mesoscale turbulence generated via baroclinic instabilities at upwelling fronts. Since the flow field was maintained by a constant supply of energy (see section 3), the turbulent flow produced was forced and statistically steady. The case of freely-decaying mesoscale turbulence generated at a sharp density front in the laboratory has already been reported by Griffiths and Hopfinger (1984). From measurements of the dispersion of neutrally buoyant particles they obtained an energy spectrum of the form  $\sim K^{-2.5}$ . Their measured spectral slope was smaller than the classical  $K^{-3}$  law, and much less than those found in numerical simulations of 2D turbulence. Later Mory and Hopfinger (1986), Maxworthy et al. (1987) and Narimousa et al. (1987) employed the same particle dispersion methods and again they found energy slopes close to those reported by Griffiths and Hopfinger (1984) for the enstrophy cascade range. It appeared that independently of how one generated 2D turbulence in the laboratory, the measured spectral slope was always close to  $\sim K^{-2.5}$ , if particle dispersion methods were used. The value of the slope did not change as a result of dramatic increase in the number of particles, considerable changes in values of turbulent Reynolds number or rotation rate (Max-

worthy *et al.* (1987), Narimousa *et al.* (1987c)). However, recent studies (summarized in Maxworthy 1989) have shown that such methods are in error when the actual spectral slope is larger than -3. In this case Babiano *et al.* (1985) and Bennet (1984) argue that the lower spectral slopes found by particle dispersion methods were due to nonlocality of the particle dynamics while the arguments which lead to the classical relationship between particle diffusion and spectral slope are based on local dynamics. As in Maxworthy (1989) we decided to employ other means to calculate the energy spectra. In (section 4) we show graphs of  $E$ - $K$  inferred from taking a direct 2D, FFT of mean square turbulent velocities.

### 3. The Experiment

Since the present study employs the experiments of Narimousa and Maxworthy (1987a), the reader is referred to that paper for a detail discussion of the apparatus and the range of parameters used, only a brief description will be given here.

Two layers of salt water of slightly different densities were brought to solid body rotation inside a cylindrical tank (90 cm in diameter and 20 cm in depth) having a conical bottom with a slope of about 0.27. The surface of the upper fluid was in contact with a circular, smooth disc, which, as it rotated, applied a stress to this surface producing an along-shore shear flow and an offshore Ekman flux in the top layer. As a result, an upwelling front was formed around the outer edge of the tank. The velocity vectors of the current and the upwelling frontal movement were observed by placing small neutrally buoyant particles in the front and recording their motion by streak photography. The direction of motion of these particles was found by firing an electronic flash at the beginning of the time exposure. To reveal the structure of the eddies, the camera was set to rotate at a rate close to the drift velocity of the eddies. In this way a frozen flow field was recorded (figure 1) and the resulting streaks represented the turbulent velocities.

### 4. Results

The digitized turbulent velocity data of a given flow field (figure 1) was interpolated into a regular  $32^2$  grid (see figure 2). Then a direct 2D, FFT was performed on the mean squared turbulent velocities deduced from the interpolated data. This resulted in a 2D energy spectra, which consisted of surfaces of constant  $K$  that are centered at the origin of a rectangular ( $k_x$ ,  $k_y$ ) coordinate system ( $k_x$  is the wavenumber in the  $x$ -direction,  $k_y$  is the wavenumber in the  $y$ -direction and  $K = (k_x^2 + k_y^2)^{1/2}$ ). In order to extract a 1D energy spectra, the energy was averaged around each surface of the associated wavenumber.

In this way an average energy level was calculated for each  $K$  and a 1D wavenumber-energy spectra was obtained (see figure 3).

At lower values of  $K$ , figure 3 shows a consistent  $K^{-5/3}$  spectra slope for a rather wide range of values of  $\theta_*$ , where,  $\theta_* = (g'h_0)/(u_*f\lambda_*)$  (here  $g' = g\delta\rho$ ,  $\delta\rho$  is the density difference between the two layers,  $f$  is the Coriolis parameter,  $h_0$  depth of the top layer,  $u_*$  is the friction velocity and  $\lambda_*$  is the width of the upwelled water at the surface). At higher values of  $K$ , the direct method, however, produces a second spectral range with a slope much steeper than that obtained at lower  $K$ . This spectral form changed from  $K^{-5.4}$  at values of  $\theta_* \approx 1.7$ , to  $K^{-4.32}$  at values of  $\theta_* \approx 20$ , indicating a noticeable decrease in value of the slope  $\alpha$  as the value of  $\theta_*$  increased.

The most important result is that the energy spectra consists of two distinct ranges. The  $K^{-5/3}$  range at lower values of  $K$ , and the range with much steeper slope ( $\sim K^{-5}$ ) at higher values of  $K$ . According to the classical theories of forced 2D turbulence (see section 1), the  $K^{-5/3}$  is the inverse energy cascade inertial range. This result is consistent also with numerical simulations of Herring and McWilliams (1985) and Frisch and Sulem (1984) and experimental results of Sommeria (1986). Classical theories predict the  $K^{-3}$  for the enstrophy cascade inertial range at higher  $K$ , also. At such wavenumbers the slope of kinetic energy ( $\sim K^{-5}$ ) is considerably steeper than the ( $K^{-3}$ ) predicted by the theories. The much steeper slope found in the present study is consistent with those predicted frequently by numerical experiments. High resolution numerical experiments of Brachet et al. (1988) showed that energy spectra is not unique at  $K^{-3}$  in the so called enstrophy cascade range. They observed a  $K^{-4}$  range for a short time which changed sharply to the  $K^{-3}$  when the enstrophy dissipation was maximum and at a later time, due to isolated concentration of vorticity, coherent vortices dominated the flow field. McWilliams (1984) showed that such coherent structures last for a long time and he identified them with an approximate  $K^{-5}$  energy spectrum. His isovorticity contours clearly revealed the structure of these isolated, coherent vortices.

In the present study, the recorded turbulent velocity field represents the fully developed, long time behavior of the flow. Figure (4) shows an example of contour map of the vorticity field in which many coherent vortex structure can be seen. These structures are closely packed as in Brachet et al. (1988) and Santangelo et al. (1989) for example, and not isolated as found by McWilliams (1984). However, we have found that such coherent vortex structures produce an approximate  $K^{-5}$  energy spectra also.

In addition, figure (2) shows that in any given experiment, the two spectral slopes meet close to the wavenumber  $K_w = 2\pi\lambda_w$  where, according to the classical theories,  $K_w$  (the wavenumber of the frontal

eddies), is the input wavenumber. Since  $\lambda_w \sim (g'h_0)/(u_*f)$  is a function of both the Rossby deformation radius  $R_0 = (g'h_0)^{1/2}/f$  and the Richardson number  $R_0 = (g'h_0)/u_*^2$ , we can write

$$K_w = \frac{2\pi}{\lambda_w} \sim 2\pi \left( \frac{u_*f}{g'h_0} \right) \sim 2\pi R_0^{-1/2} R_0^{-1}.$$

Furthermore it is possible to estimate the two-dimensional Kolmogorov constant ( $C$ ) according to

$$E(k) = C\epsilon^{2/3}(k)^{-5/3},$$

The calculated values of  $3.6 < C < 6.3$  are within the range of those estimated by Lilly (1969), 4.3-6.2 Herring and Kraichnan (1975), 6.5, Herring and McWilliams (1985), 2.9-4.8 and Sommeria (1986), 3-7, but smaller than those of Frisch and Salem (1984), 9, and much smaller than those of Siggia & Aref (1981), 14.

### 5. Summary and Conclusions

When we performed a direct 2D, FFT on the mean square turbulent velocities, the induced 1D energy spectra produced two distinct inertia ranges also; a  $K^{-5/3}$  spectrum at lower  $K$  and one approximately varying as  $K^{-5}$  at higher  $K$ . The  $K^{-5/3}$  result is consistent with that predicted for the inverse energy cascade inertia range and the  $K^{-5}$  is in agreement with those obtained in numerical simulations for the enstrophy cascade in stationary flow. The two inertia ranges meet close to a wavenumber that is associated with the wavenumber of the frontal eddies ( $K_w \sim 2\pi(u_*f)/(g'h_0)$ ) and therefore according to classical theories  $K_w$  is the input wavenumber. We have estimated the 2D Kolmogorov constant ( $C$ ), within the  $K^{-5/3}$  inertia range. The values of  $C$  varied within the range  $3.6 < C < 6.3$ .

According to classical theories and numerical simulations of 2D or geostrophic turbulence, the spectral slopes ( $K^{-5/3}$  at lower  $K < K_w$  and  $K^{-5}$  at higher  $K > K_w$ ) found in the present study suggest that turbulence in our model is two dimensional. This in turn suggests that the prototype system we are attempting to model can also be considered to be a 2D turbulent field. Since jet-like structures or rivers evolve in such a field in the laboratory then presumably they do also in the natural flow, this helps to explain the filamentary structures which transport passive markers, e.g. heat, as observed in satellite images.

### 6. Acknowledgment

The authors wish to thank the Office of Naval Research for supporting this research under Grant No. N00014-87-K-0809.

## 7. References

- BABIANO, A., BASDEVANT, C. & SADOURNY, R. 1985 Structure functions and dispersion laws in two-dimensional turbulence. *J. Atmos. Sci.* **42**, 941-949.
- BATCHELOR, G. K. 1969 Computation of energy spectrum in homogeneous two-dimensional turbulence. *Phys. Fluid Suppl.* **12**, II 233.
- BRACHET, M. E., MENEGUZZI, M., POLITANO, H. & SULEM, P. L. 1988 The dynamics of freely decaying two-dimensional turbulence. *J. Fluid Mech.* **194**, 333-349.
- CHARNEY, J. G. 1971 Geostrophic turbulence. *J. Atmos. Sci.* **28**, 1087-1095.
- FRISCH, U. & SULEM, P. L. 1984 Numerical simulation of inverse cascade in two-dimensional turbulence. *Phys. Fluids* **27**, 1921-1923.
- GRIFFITHS, R. W. & HOPFINGER, E. J. 1986 The structure of mesoscale turbulence and horizontal spreading at ocean fronts. *Deep-Sea Research* **31**, 245-269.
- HERRING, J. R. 1980 Statistical theory of quasi-geostrophic turbulence. *J. Atmos. Sci.* **37**, 969-977.
- HERRING, J. R. & McWILLIAMS, J. C. 1985 Comparison of direct numerical simulation of two-dimensional turbulence with two-joint closure: the effects of intermittency. *J. Fluid Mech.* **153**, 229-242.
- HEYER, J. M. & SADOURNY, R. 1982 Closure modeling of fully developed baroclinic instabilities. *J. Atmos. Sci.* **39**, 707-721.
- KOLMOGOROV, A. N. 1941 Dispersion of energy in locally isotropic turbulence. *C. R. Acad. Sci. URSS*, **32**, 16.
- KRAICHNAN, R. H. 1967 Inertial ranges in two-dimensional turbulence. *Phys. Fluids* **10**, 1417-1423.
- KRAICHNAN, R. H. 1975 Statistical dynamics of two-dimensional flow. *J. Fluid Mech.* **67**, 155.
- LEITH, C. E. 1968 Diffusion approximation for two-dimensional turbulence. *Phys. Fluids* **11**, 671-673.
- LESIEUR, M. 1987 *Turbulence in fluids*. Martinus Nijhoff Publishers.
- LILLY, D. K. 1969 Numerical simulation of two-dimensional turbulence. High-speed computing in fluid dynamics. *Phys. Fluid Suppl.* **12**, II 240.
- MAXWORTHY, T. 1989 The dynamics of two-dimensional turbulence. *Proc. of Conf. on the "Oceanography of Sea Straits"*, les Arcs, France.

- MAXWORTHY, T., CAPERAN, P. & SPEDDING, G. R. 1987 Two-dimensional turbulence and vortex dynamics in a stratified fluid. *Proc. Third Inter. Conf. on Stratified Flows*. Pasadena, California.
- McWILLIAMS, J. C. 1984 The emergence of isolated coherent vortices in turbulent flow. *J. Fluid Mech.* **146**, 21-43.
- MORY, M. & HOPFINGER, E. J. 1986 Structure functions in a rotationally dominated turbulent flow. *Phys. Fluids* **29**, 2140-2146.
- NARIMOUSA, S. & MAXWORTHY, T. 1985 Two-layer model of shear driven coastal upwelling in the presence of bottom topography. *J. Fluid Mech.* **159**, 503-531.
- NARIMOUSA, S. & MAXWORTHY, T. 1986 Effects of a discontinuous surface stress on a model of coastal upwelling. *J. Phys. Oceanogr.* **16**, 2071-2083.
- NARIMOUSA, S. & MAXWORTHY, T. 1987a Coastal upwelling on a sloping bottom: The formation of plumes, jets and pinched-off cyclones. *J. Fluid Mech.* **176**, 169-190.
- NARIMOUSA, S. & MAXWORTHY, T. 1987b Effects of coastline perturbations on coastal currents and fronts. *J. Phys. Oceanogr.* **17**, 1296-1303.
- NARIMOUSA, S., MAXWORTHY, T. & SPEDDING, G. R. 1987c Structure of meso-scale baroclinic turbulence. *Sixth Symposium on Turbulent Shear Flows*. Toulouse, France, September 7-9.
- NARIMOUSA, S. & MAXWORTHY, T. 1989 Application of a laboratory model to the interpretation of satellite and field observations of coastal upwelling. *Dyn. Atmos. Oceans* **13**, 1-46.
- SALMON, R. 1978 Two-layer quasi-geostrophic turbulence in a simple case. *Geophys. Astrophys. Fluid Dyn.* **10**, 25-51.
- SANTANGELO, R., BENZI, R. & LEGRAS, B. 1989 The generation of vortices in high-resolution, two-dimensional decaying turbulence and the influence of initial conditions on the breaking of self-similarity. *Phys. Fluids* **1**, 1027-1034.
- SIGGIA, E. D. & AREF, H. 1981 Point vortex simulation of the inverse cascade in two-dimensional turbulence. *Phys. Fluids* **24**, 171-173.
- SOMMERIA, J. 1986 Experimental study of the two-dimensional inverse energy cascade in a square box. *J. Fluid Mech.* **170**, 139-168.

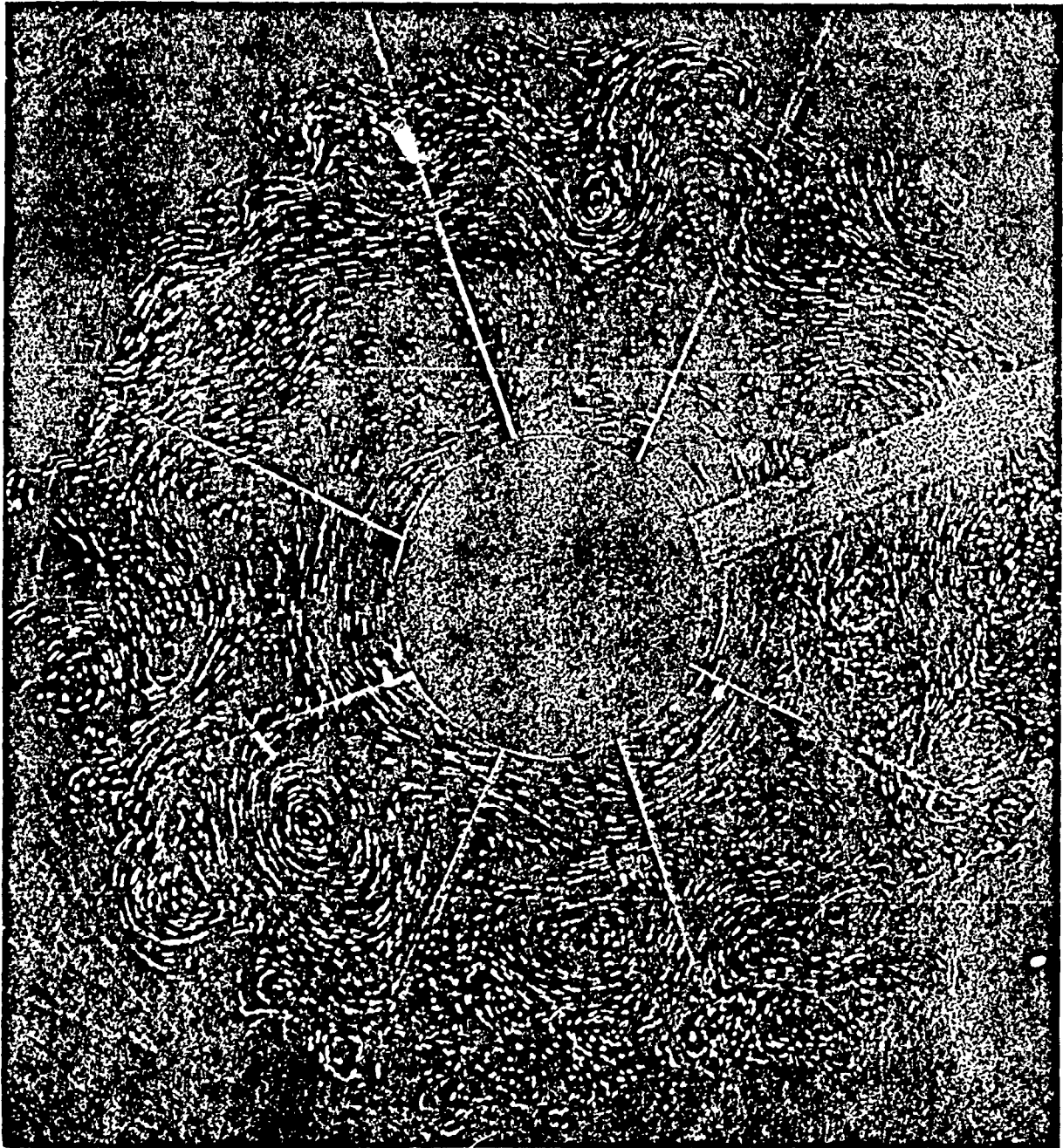
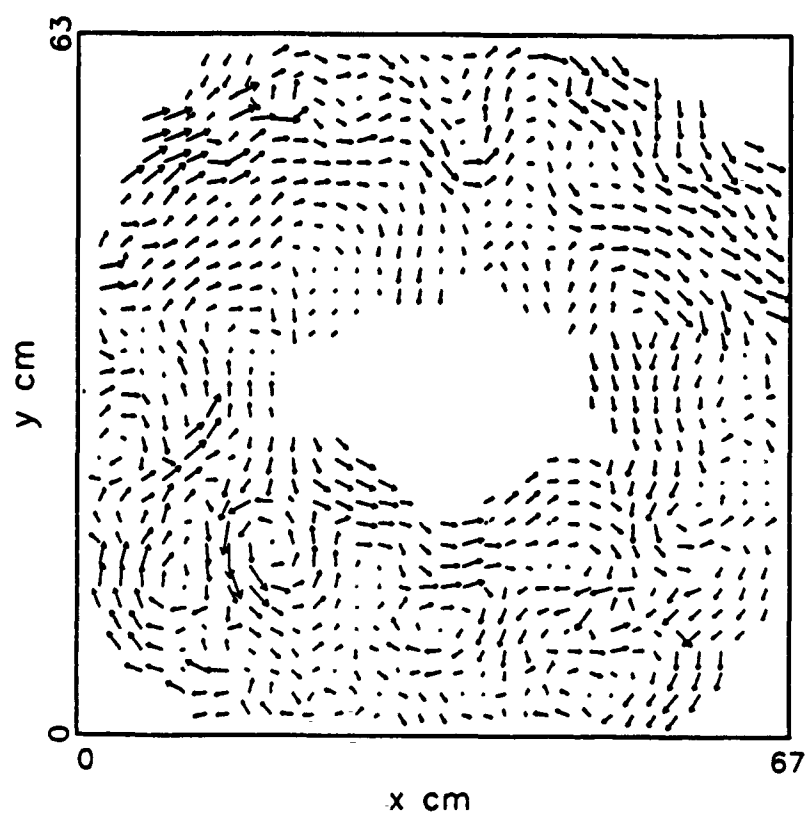


Fig.1. A streak photograph of frozen flow field showing an example of long-time behavior of meso-scale eddy structures at an upwelling front and their immediate vicinity.



**Fig.2.** The original particle streak data (figure 1) as interpolated on to a regular  $32^2$  grid by convolution with an adaptive Gaussian window.



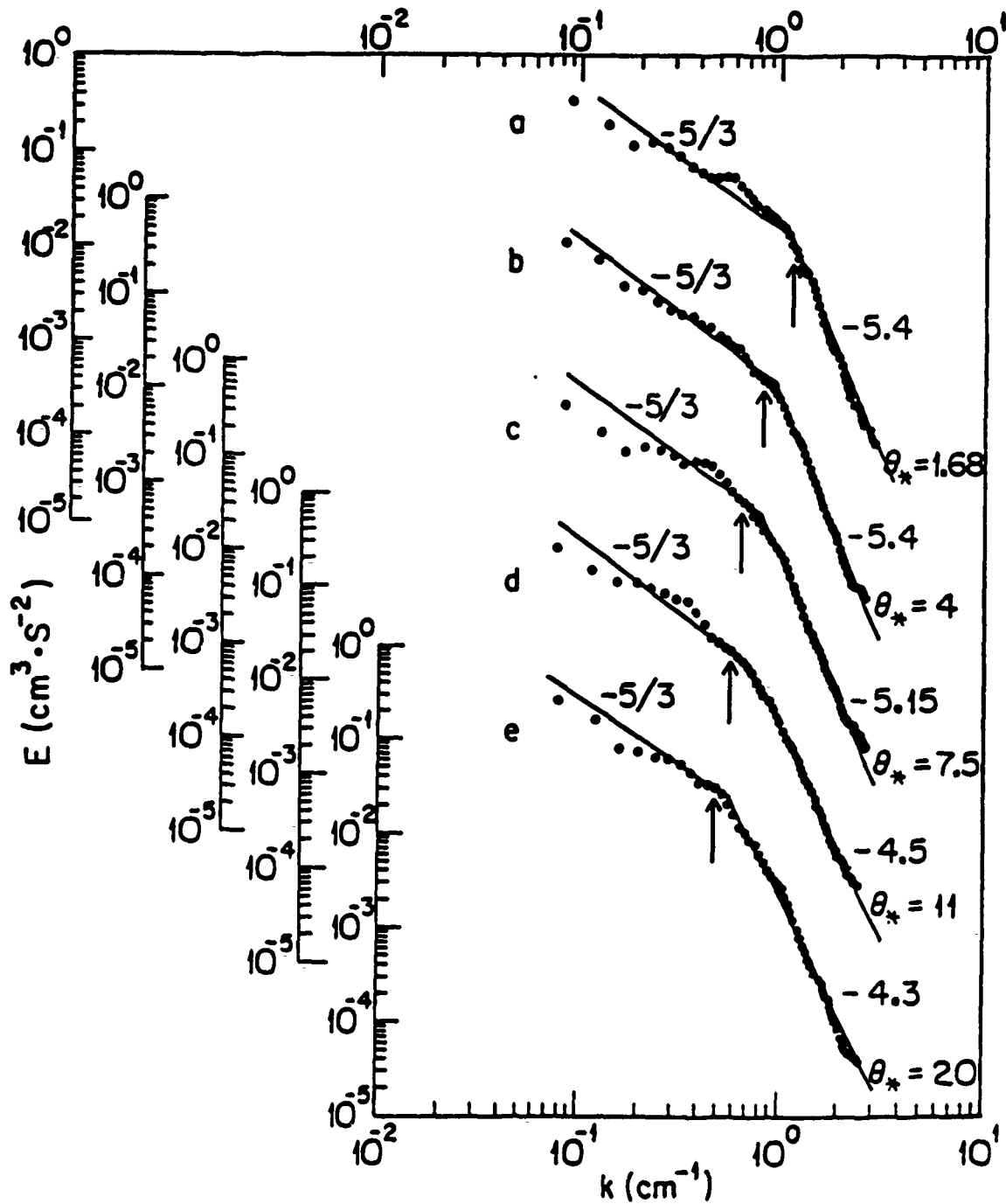


Fig.3. One-dimensional energy spectra ( $E$ ) as a function of wavenumber ( $k$ ), inferred from a direct 2D, FFT of the mean square turbulent velocities deduced from the interpolated data such as that shown in figure 2.

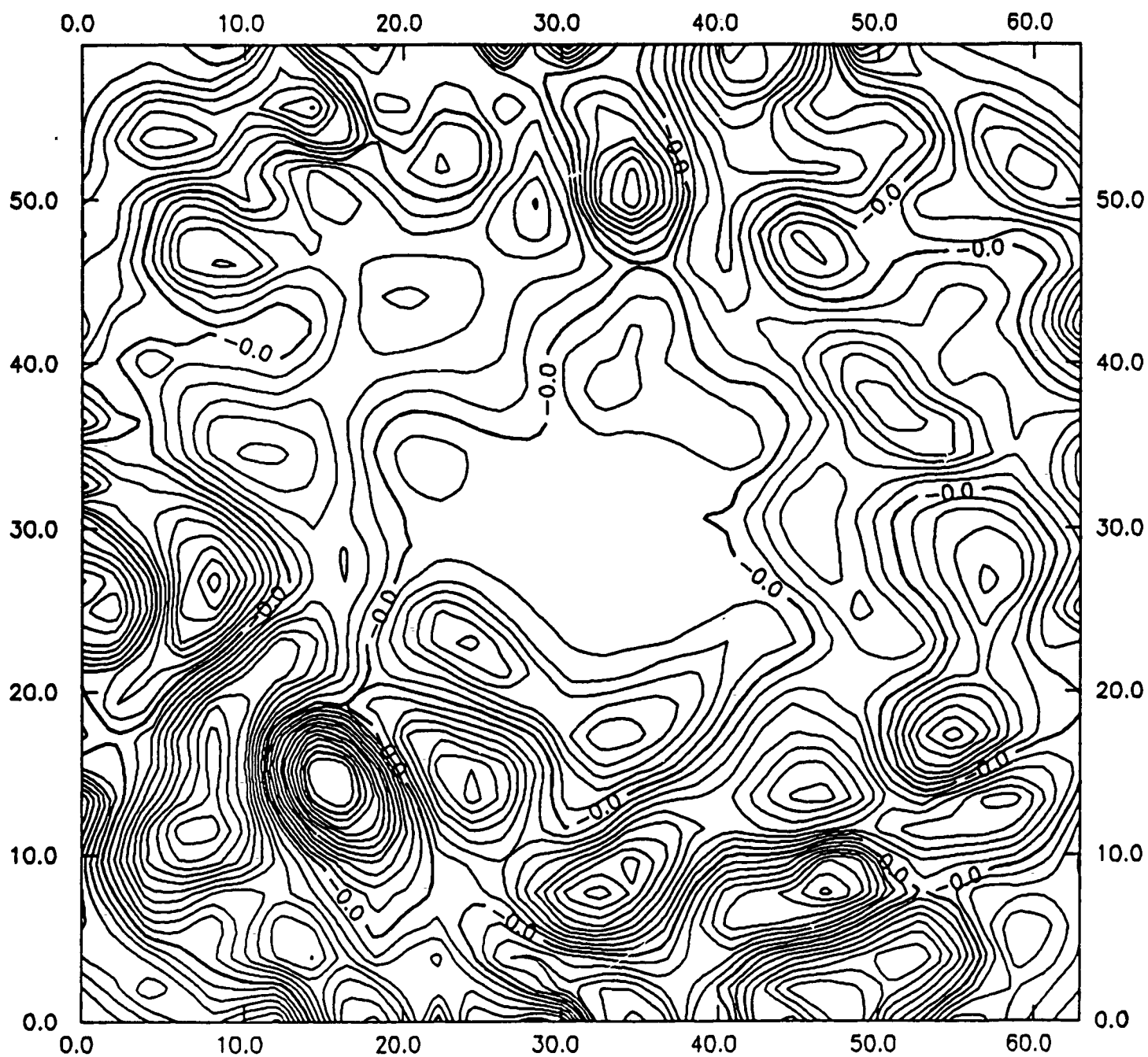


Fig.4. Iso-vorticity contours for figure 1.

**Homogeneous Rotating Flow Past  
A Coastal Submarine Ridge**

**Siavash Narimousa**

**University of Southern California  
Department of Mechanical Engineering  
Los Angeles, CA 90089-1453**

### Abstract

Simulated, alongshore coastal currents driven by surface stress were generated around the outer edge of a rotating cylindrical tank, initially filled with a layer of homogeneous water. The induced flow was allowed to interact with a submarine coastal-ridge. As a result, an alongshore, meandering flow was formed. The meander consisted of a large amplitude, standing wave extending offshore over the ridge and several waves downstream of it. The standing waves contain trapped, cyclonic eddies within them. For values of Rossby  $\beta$ -number  $R_\beta = U/\beta Lw < 0.16$  ( $U$  is the mean current velocity,  $\beta = f\alpha/H$ ,  $f$  is the Coriolis parameter,  $\alpha$  is the bottom slope,  $L$  is the width of the coastal current over the sloping bottom and  $w$  is the average width of the ridge) and aspect ratio  $(h_r/H) > 0.35$  ( $h_r$  and  $H$  are the average heights of the ridge and the water column) the induced meander displayed strong offshore movement over the ridge. Under this circumstances, several stationary, trapped, cyclonic eddies that were aligned in the offshore direction were formed within the standing over the ridge. As a result, the trapped cyclones pinched large patches of coastal water and transport them far offshore over the ridge. Unlike the two-layer stratified experiments of Narimousa and Maxworthy (1985), here cyclonic eddies did not pinch-off from the trough of the standing waves. Measurements of the wavelength of the generated meanders were consistent with  $\lambda_w = 15.5 w (h_r/H)^{1/3} (R_\beta)^{0.75}$ . Horizontal velocity gradients at the edge of the meanders were the site of secondary eddies (shear instabilities).

## 1. INTRODUCTION

The summertime, alongshore, southward component of the wind stress off the west coast of the USA, generates an equatorward current and an upwelling front offshore. The absence of major coastal irregularities to the North of cape Blanco allows a uniform upwelled front and associated frontal eddies to develop in this region. Satellite (IR) images of the upwelling events north of cape Blanco display the presence of a uniform upwelled front and associated eddies [see Narimousa and Maxworthy 1989, Thompson and Papadakis 1987]. The presence of significant coastal topographic features (like the Mendocino ridge) to the south of cape Blanco, drastically affect the appearance of the flow field and the upwelling front. This is evident from the satellite (IR) images that have repeatedly revealed the presence of large amplitude, offshore extending, standing structures at the Mendocino ridge and downstream of it. The presence of significant coastal irregularities, to the south of cape Blanco do not allow a uniform upwelled front to form in this region.

When the two-layer laboratory model of Narimousa and Maxworthy [1987] was free of coastal irregularities alongshore current and upwelling front and associated baroclinic eddies evolved naturally. With a submarine offshore-extending coastal ridge, a uniform upwelled front was formed upstream of the ridge, while a meandering, jet-like flow in the form of standing waves was formed at the ridge and downstream [Narimousa and Maxworthy 1985, here after NM1, and 1989]. These laboratory observations were consistent with the flow fields seen in the

satellite (IR) images of the west coast of the USA.

To further emphasize the significance of a major submarine coastal ridge upon interaction with an alongshore coastal current, new laboratory evidence is presented here. The present experiments consider a single layer flow only. The produced alongshore flow is allowed to interact with a single ridge in place. To test the importance of ridge elevation and width, several ridges are considered. The induced meander, pinched-off eddies and secondary instabilities of the type reported by Washburn and Armi (1988), are visualized by a passive marker. In the absence of stratification, baroclinic eddies are absent and the observed eddies are of the forced, barotropic type. Features observed in the model are compared to those generated by the Mendocino ridge and the ridge at point Sur, as revealed by the satellite (IR) images. The model has predicted an empirical formula (see 5) to estimate the wavelength of the induced meander. Application of this formula to a meander generated by the Mendocino ridge is described in 5.

## 2. THE EXPERIMENT

The present experiments were performed in the original model of Narimousa and Maxworthy [1985]. For a detailed discussion of the apparatus the reader is referred to that paper, only a brief description will be given here.

A single layer of homogeneous, salt water was brought to solid body, counter-clockwise rotation inside a cylindrical tank (90 cm in diameter and a working depth of about 19.5 cm) with a conical bottom [slope 0.27] and a radial ridge in place [figure 1]. The ridge models were manufactured by cutting axial slices from a solid, transparent cone in such a way that the average width ( $W$ ) of the ridges was the same (3.8 cm), while their average height ( $h_r$ ) was 0.875, 1.55 and 2.9 cm for small, medium and large ridge, respectively. A clockwise differentially rotating

disc applied a stress to the top surface of the water. The surface stress caused the water layer to flow around the tank and interact with the given ridge in place. To visualize the induced flow field, a passive marker (white color) was released initially near the ridge at the wall of the tank at a depth of about 2 cm. Consequently, the marker was transported into the induced features. In this way the features were revealed for observation and photography. In order to reveal full field visualization of the flow, streak photography was used in some experiments.

In the present experiments, the parameters took the following values: Average depth of the water layer  $H=8.25$  cm; the Coriolis parameter  $1.37 < f < 5.46$  rad  $s^{-1}$ ; the average mean velocity of the water upstream of the ridge  $2.2 < U < 2.45$  cm  $s^{-1}$  and the Rossby  $\beta$  number  $R_\beta = U/\beta wL$  varied within the range  $0.035 < R_\beta < 0.4$ .

### 3. STRUCTURE OF THE MEANDER

When the system was in solid-body rotation (anticlockwise), the top disk was set to rotate (clockwise), thus applying a stress to the top surface of the water. As a result, the water layer was driven around the tank and interacted with the given ridge. In general, as in the two-layer case (NM1), when the upstream fluid columns reach a ridge, where the water depth is more shallow, then the columns flow offshore toward deeper water, and reverse direction once past the ridge according to conservation of potential vorticity. Such vortex contraction initiated a jet-like flow that meandered a considerable distance downstream in the form of standing topographic waves [figure 2]. At this stage, before giving a description of the flow field revealed by dye for the ridges mentioned in section 2, we should show full field visualization of the flow generated by streak photography [figure 2]. It can be seen that the upstream flow is undisturbed until it

reaches the ridge where the meandering jet-like flow is initiated. A full description of the flow field is given in the caption of the [figure 2], and we will refer to this figure when necessary. In the absence of the sloping bottom, such meandering flow is absent and the generated flow field is quite different, for detail see Maxworthy (1977).

At higher rotation rates ( $f$ ) and with the large ridge ( $h_r/H=0.35$ ), the generated meander was very intense (standing waves have large amplitude), and displayed strong offshore movement at the ridge. As a result several stationary cyclonic eddies were formed within the standing wave over the ridge [figures 2a and 3a, and section 4 for further detail ]. Downstream of the ridge the meander consisted of at least two standing waves. Since amplitude of the downstream standing waves is considerably smaller than the one over the ridge, they contain only one cyclonic eddy within them. Here cyclonic eddies did not pinch-off from the trough of the standing waves over the ridge and those downstream. Similar waves in NM1 , however, did initiate pinched-off cyclones, the demonstration of which was displayed in that paper. In NM1 the sharp, wave trough containing heavier water penetrated into the lighter offshore water and at this stage due to baroclinic instability cyclonic eddies were pinched-off from the wave trough. Since such mechanism (baroclinic instability) is absent in the present study, then no pinch-off processes can occur here. Due to loss of energy to the bottom and side wall boundaries the amplitude of the downstream standing waves continue to decrease until, eventually the meander dies out and the current flow is again parallel with the coast. At moderate rotation rates [figure 3b], the induced meander and the resulting standing waves are less intense (have lower amplitude) when compared to those observed at higher rotation rates. Similar to the large ridge, here, stationary, cyclonic eddies are formed over the ridge also. Downstream of the ridge, the meander consisted of at least



one significant standing wave that contained a cyclonic eddy. At lower rotation rates, the meander was weak, the standing waves over the ridge was in the form of a large, stationary cyclonic eddy and a rather weak standing wave was formed at a considerable distance downstream [ figure 3c].

With the medium ridge in place ( $h/H=0.19$ , 47% shorter than the large ridge), and high rotation rates, the induced meander was rather intense [figure 4a]. The standing wave at the ridge penetrates far offshore, and contained two stationary cyclonic eddy within it. On the downstream side of the ridge, the first standing wave was the most noticeable one, and was not as intense as that produced over the large ridge. At moderate rotation rates, the medium ridge produced a weaker meander and each standing wave contained one cyclonic eddy [figure 4b]. At very low rotation rates [figure 4c] the meander was very weak, yet a large stationary cyclone was formed over the ridge as was a weak standing wave far downstream.

With the small ridge in place ( $h/H=0.11$ , 70% shorter than the large ridge), and high rotation rates, the induced meander resembled those observed at moderate rotation rates of the medium ridge [figure 5a]. At moderate rotation rates, the characteristics of the induced features were similar to those of high rotation rates, only here they were less intense [figure 5b]. At low rotation rates, the meander consisted of a weak cyclonic eddy over the ridge and a weak standing wave far downstream [figure 5c].

In general, for any given ridge, as the rotation rate of the tank decreased, the intensity of the induced meander (amplitude of the waves) decreased, the wavelength of the standing waves increased and the mean position of the wave at the ridge moved away from the ridge [figure 3,4 and 5]. As the mean elevation of the ridge increased the intensity of the meander

increased, and therefore the amplitude of the resulted standing waves increased [figure 6]. With constant rotation rates, as the average height of the ridge increased, the distance of the downstream standing wave from the ridge decreased [figure 6]. No pinched-off processes were initiated by the standing waves for any of the rotation rates and ridge heights used in the experiments.

#### . 4. OFFSHORE TRANSPORT OF COASTAL WATER AND SECONDARY INSTABILITIES

##### 4.1 *Pinch-off Processes*

As mentioned above, at high  $f$ , the large ridge with aspect ratio  $h_r/H=0.35$  generated the most intense meander, such that the standing wave at the ridge contained at least 3 stationary cyclonic eddies within it. These stationary, trapped eddies were aligned in the offshore direction over the ridge. Display of such eddy arrangement has been revealed by streak photography [figure 2a]. When a passive marker was released at the wall of the tank near the ridge we observed a frequent detachment of patches of the marker (coastal water) in the form of cyclonic eddies over the ridge [figures 3a and 7]. A comparison of figures [2a and 3a] demonstrates that the stationary cyclones over the ridge [figure 2a] pinch the patches of coastal water (the marker) within them [figure 7]. The pinched-off patches then moved in the off-shore direction from eddy to eddy, while remaining over the ridge [figure 7]. When a given patch reached the vicinity of the jet flow of the meander far offshore it became stationary and did not leave the ridge. This situation did not last long, because the patch eventually interacted with the jet flow of the meander directly. Thereafter, the strong jet flow of the meander pulled the cyclonic patch along its inner edge (coastal side) to form a strip that extended to a considerable distance downstream

[figure 6]. Eventually the patch vanished and the strip which reached its longest length was advected downstream and then vanished as a separate entity. This process repeated itself during the course of a given experiment.

As mentioned in section 3, at moderate  $f$  with the large ridge, two larger, stationary cyclonic eddies were formed over the ridge. Here, the pinched-off patches eventually interacted with the meander also, and vanished as separate entities in a fashion similar to that described above for high  $f$ . At lower rotation rates and/or ridge heights the above processes was less noticeable.

#### 4.2 *Secondary cyclonic eddies*

The horizontal velocity gradient (shear instabilities) across the inner edge (coastal side) of the alongshore meander allowed secondary cyclonic eddies to develop along this edge at different locations. These secondary eddies, usually, are initiated at the wave crest near the wall of the tank and continue to grow as they move toward the standing wave trough. Two successive eddies of this type are shown in [figure 3b] near the downstream standing wave trough. The larger one (at the wave trough) is fully developed, while the smaller one continues to grow until it replaces the larger one. Once fully developed, the secondary eddies reverse direction and tend to propagate toward the coast along the downstream side of the standing wave. At this stage, the secondary cyclones are seized by the large cyclonic eddy of the standing wave itself. The other location which allowed such secondary instabilities to develop, was along the upstream part of the meander that formed over the ridge. Here the secondary cyclones were initiated and grew in a fashion similar to that described above. A distinct display of such secondary cyclones formed

along the meander over the ridge is shown in [figure 4].

At high  $f$  and with the large ridge, the induced meander was very intense and the width of the horizontal shear layer across the inner edge of the meander was narrow. Therefore small secondary cyclonic eddies formed along this meander [figure 3]. As  $f$  decreased and/or a smaller ridge was in place, the intensity of the meander decreased while the width of the shear layer increased. As a result, larger secondary eddies were formed along the meander [figure 3b & 3c].

## 5. MEASUREMENTS AND APPLICATIONS

From the photographs presented in this paper it is possible to measure the wavelength  $\lambda_w$  of the standing waves. To obtain a universal relationship between  $\lambda_w$  and the important parameters involved, the best choice was to plot  $(\lambda_w/w) (h_r/H)^{1/3}$  as a function of the Rossby number  $R_\beta$  for all the meanders generated in the laboratory [figure 8]. According to these plots one can write,

$$(\lambda_w/w) (h_r/H)^{1/3} = a (R_\beta)^{3/4}, \quad (1)$$

where the constant ( $a=15.5$ ) is estimated from [figure 8]. Relationship (1) can also be written for  $\lambda_w$  as follows;

$$\lambda_w = 13.5 w (h_r/H)^{1/3} (R_\beta)^{3/4}. \quad (2)$$

Since (2) is estimated for many different meanders, one can estimate  $\lambda_w$  for any meander that

is generated along any coast under circumstances similar to those generated in the laboratory.

Let us consider a satellite (IR) image [figure 9] taken from the west coast of the USA, showing an alongshore meander that is generated as a result of an interaction between the coastal current generated by an alongshore wind and the Mendocino ridge. This satellite (IR) image was taken when the southward, alongshore component of the mean wind velocity had a magnitude of about 7 m/s. According to [Tseng 1987] such wind velocity should generate a mean surface velocity of about  $U=20$  cm/s in the water. From the simplified contour map of the bottom topography off the west coast of the USA, one can estimate a value of  $w=70$  km, for the average width of the Mendocino ridge with  $h_i=1$  km and  $H=2$  km. Taking  $f=10^{-4}$  s<sup>-1</sup>,  $L=60$  km, and Substituting this field data in equation (2), the model predicts a value of about  $\lambda_w=75$  km, for the wavelength of the meander shown in [figure 8]. The direct measurement of the wavelength from [figure 8 and 9] gives a value of about  $\lambda_w=80$  km.

The laboratory model, has predicted that at values of  $h_i/H > 0.35$  and  $R_\rho < 0.16$ , large patches of coastal water may pinch-off over the ridge and move offshore ( section 4.1). As indicated above, the Mendocino ridge has values of  $h_i/H=0.5$  and  $R_\rho=0.02$ , therefore, according to the model large patches of coastal water should pinch-off over the Mendocino ridge. Such pinch-off processes have been revealed by satellite (IR) images shown in [figure 11]. Similar processes caused by the ridge at point Sur have been revealed by the satellite (IR) images, also [figure 12].

## 6. SUMMARY AND CONCLUSIONS

Alongshore coastal currents generated by surface stress in the presence of rotation were

allowed to interact with a given coastal submarine ridge. As a result, a meandering flow in the form of a standing, topographic waves was formed over the ridge and downstream. The wavelength of the meander that is predicted by the model may be estimated from  $\lambda_w = 15.5 w_r (h_r/H)^{1/3} (R_p)^{0.74}$ . Knowing the geographic location, the wind information and the geometry of any significant coastal ridge, one can estimate  $\lambda_w$  from above equation. Applications of this equation to the meander generated by Mendocino ridge (July, 1988) predicted a value of  $\lambda_w = 75$  km, which was in a good agreement with that measured from satellite (IR) images. Since each standing waves contain at least one trapped cyclonic eddy, estimating  $\lambda_w$ , helps to locate these trapped cyclones. In the coastal ocean waters, such cyclones can play the role of a pool in accumulating marine life, fish and perhaps the disposal materials that are dumped into the coastal waters.

At aspect ratios  $h_r/H > 0.35$  and values of  $R_p < 0.16$ , large amplitude, offshore extending, standing wave that contained several stationary cyclones is formed over the ridge. As a result patches of coastal water were pinched-off by the stationary eddies and transported offshore over the ridge. At values of  $R_p = 0.08$ , the pinch-off process was more frequent and the detached patches moved farther offshore. Observations [figure 7] showed that these pinched-off patches may interact with the jet flow of the meander and vanish as separate entities. Satellite (IR) images taken from the west coast of the USA, frequently revealed such pinch-off processes taking place over the Mendocino ridge and the ridge at point Sur.

Horizontal velocity gradients at the edge of the meander allowed successive secondary cyclonic eddies to form along the upstream side of the standing waves. Such instabilities are repeatedly seen in the satellite IR images taken from such meanders off the west coast of the

USA.

The author wish to thank Professor Tony Maxworthy, who made this work possible, and the Office of Naval Research (ONR) for supporting this work under ARI on the Coastal Transition Zone, Contract No. N00014-87-K-0809 to USC.

### REFERENCES

Maxworthy, T., Topographic effects in rapidly-rotating fluids: Flow over transverse ridge. *Z. angew. Math Phys.*, 28, 853-864, 1977.

Narimousa, S., and T. Maxworthy, Two-layer model of shear driven coastal upwelling in the presence of bottom topography. *J. Fluid Mech.*, 159, 505-531, 1985.

Narimousa, S., and T. Maxworthy, Coastal upwelling on a sloping bottom: the formation of plumes, jets and pinched-off cyclones. *J. Fluid Mech.*, 176, 169-190, 1987.

Narimousa, S., and T. Maxworthy, Applications of a laboratory model to the interpretation of satellite and field observations of coastal upwelling. *Dyn. Atmos. Oceans*, 13, 1-46, 1989.

Tseng, R. T., Longitudinally-averaged and wave-modulated turbulent boundary layer above and below a wind-induced water surface. *Ph.D. thesis, University of Delever*, 1987.

Thomson, R. E., and Papadakis, Upwelling filaments and motion of a satellite tracker drifter along the west coast of North America. *J. Geophy. Res.*, 92, 6445-6461, 1987.

Washburn, L., and L. Armi, Observations of frontal instabilities on an upwelling filament. *J. Phys. Oceanogr.*, 18, 1066-1092, 1988.

## List of figures

Fig. 1. Cross-sectional side view of the experimental tank (half) and the sloping bottom. Height difference between the small (----), the medium (- - -) and the large ridge (----) is shown also. Here,  $r$  is the distance measured from the side wall (S.W.) and  $h$  is the height measured from the tank base (B.T.).

Fig. 2. Streak photographs showing full field visualization of the fully develop long time behavior of the flow fields that are generated as a result of the interaction between the mean flow and the ridge. This ridge has a width of about  $w=5.7\text{ cm}$ , and a height of about  $h_r=1.55\text{ cm}$ . The time exposure  $\delta t=2s$ , and the differential rotation of the top disc  $\delta\Omega=0.134\text{ s}^{-1}$  is the same for the photographs (a), (b) and (c). Upstream of the ridge the mean flow is parallel to the coast, while a meandering jet-like flow is initiated at the upstream edge of the ridge and extends a considerable distance downstream in the form of standing topographic waves. The standing wave over the ridge has larger amplitude than those formed downstream. Photograph (a) taken at high rotation rate ( $f=5.6\text{ s}^{-1}$ ), showing 3 stationary cyclones (SC) within the large amplitude standing wave over the ridge, and at least one cyclone within each downstream standing wave. Here, after passing the ridge, a part of the meander has been separated at point S, and extended in the offshore direction. Photograph (b) taken at moderate rotation rate ( $f=3\text{ s}^{-1}$ ), showing that the distance between the standing waves (wavelength,  $\lambda_w$ ) has increased, and there is at least one cyclonic eddy within the standing wave over the ridge and that downstream. Photograph (c) taken at low rotation rate ( $f=1.5\text{ s}^{-1}$ ), showing that  $\lambda_w$  has increased further.



Fig. 3. Long time behavior of the fully developed alongshore meander generated by the large ridge ( $h_r/H=0.35$ ) has been revealed by the injected dye. Photograph (a) has a value of  $R_\beta=0.1$ , the intense meander and associated standing waves (SW) are shown. A large patch (PC) of coastal water has been pinched-off by the stationary, trapped cyclone over the ridge, and secondary eddies (SE) are formed at the edge of the first downstream standing wave. Photograph (b) has a value of  $R_\beta=0.17$ , the meander is less intense (standing waves have lower amplitude), its wavelength increased and the secondary eddies (SE) are larger. Photograph (c) has a value of  $R_\beta=0.24$ , and the wavelength of the meander has increased further. Several secondary eddies (SE) have been formed at the edge of the standing wave over the ridge. Also, notice that as  $R_\beta$  increased the standing wave over the ridge moves toward the downstream side of the ridge.

Fig. 4. Similar to [figure 3] only here the medium ridge ( $h_r/H=0.19$ ) is in place. Photograph (a) has a value of  $R_\beta=0.1$ , the meander is less intense when compared to [figure 3]. A train of secondary eddies (SE) has been formed at the edge of the standing wave over the ridge. Photograph (b) has a value of  $R_\beta=0.17$ , the wavelength of the meander has increased and several secondary eddies have formed at the edge of the standing wave over the ridge and the one downstream. Photograph (c) has a value of  $R_\beta=0.28$ , and only one noticeable standing wave in the form of a large cyclonic eddy has been formed over the ridge itself.

Fig. 5. Similar to [figures 3 & 4], only here the small ridge ( $h_r/H = 0.11$ ) is in place. These photographs have values of  $R_\beta=0.09, 0.16$  and  $0.25$  for (a), (b) and (c) respectively. Here the meander is much weaker (standing waves have lower amplitude) than those produced by the

large and the medium ridges for the same values of  $R$ . Secondary eddies (SE) form at the edge of the standing wave over the ridge and the one downstream. At high  $R$  the meander consists of a weak standing wave (SW) over the ridge (c).

Fig. 6. These photographs have a value of  $R_\rho = 0.12$ , for (a) the large, (b) the medium and (c) the small ridge. Notice that as the ridge elevation decreased intensity of the meander decreased, its wavelength increased and the most noticeable pinch-off processes (PC) occurred over the large ridge.

Fig. 7. A sequence of photographs (taken after those shown in figure 3), having a value of  $R_\rho = 0.1$ , and the large ridge in place, showing a large patch (PC) of coastal water that has been pinched-off over the ridge (a). Photograph (b) taken two rotation periods later, showing the patch in (a) has moved farther offshore while remaining over the ridge. Photograph (c) taken two rotation periods later, the patch has interacted with the jet flow of the meander and has been stripped to a considerable distance downstream. Photograph (c) shows a new pinched-off patch which is moving offshore over the ridge.

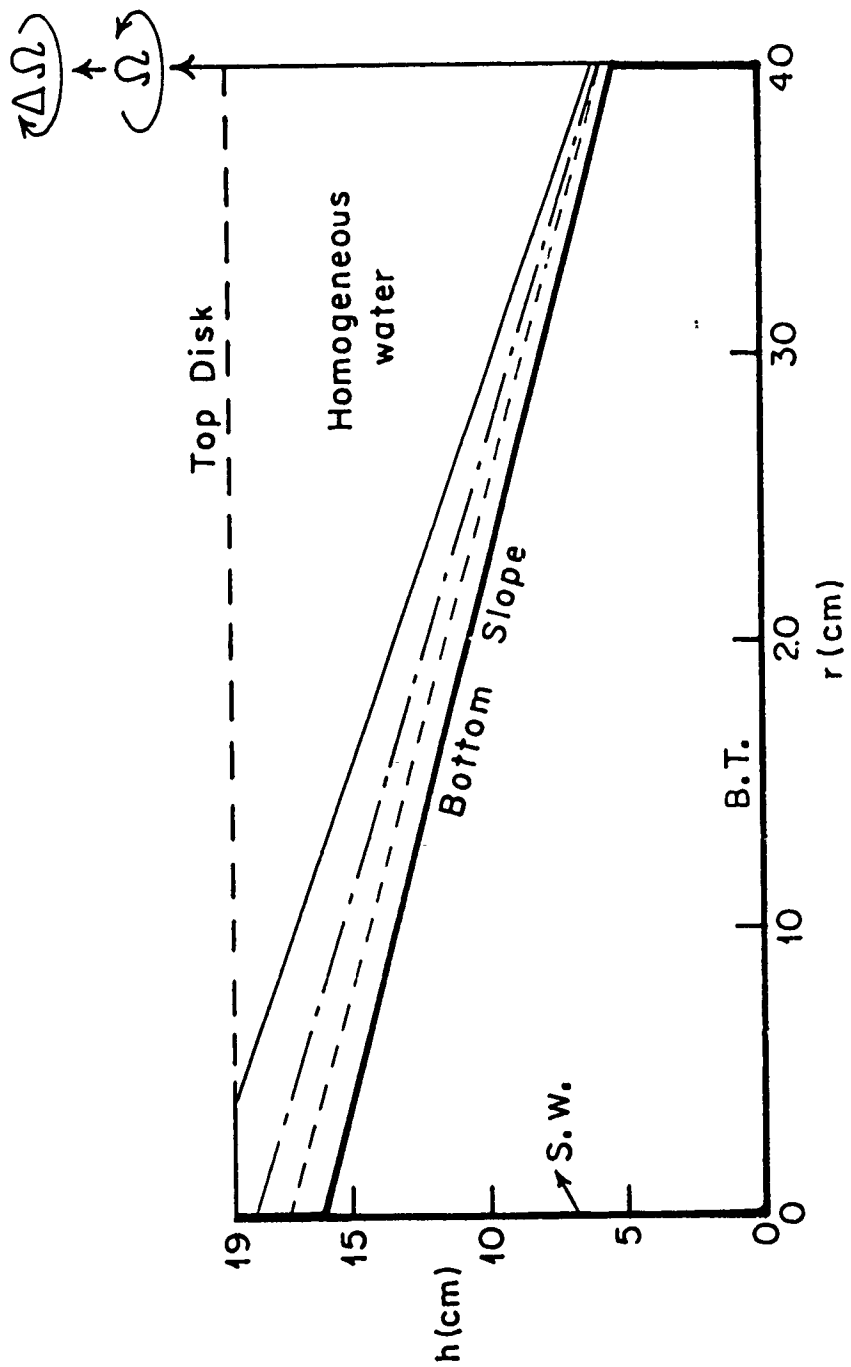
Fig. 8. The variation of  $(\lambda_w/w) (h_r/H)^{1/3}$  with Rossby number  $R_\rho$ , for the large ( $\bullet$ ), the medium ( $+$ ) and the small ( $\times$ ) ridge. The symbol ( $\Delta$ ), represent the data taken from figure 2, and the symbols ( $\blacktriangle$ ), ( $\blacktriangledown$ ), represent the data for ridges similar to figure 2, but with  $w=9.5, 8.5$  cm, and  $h_r=2$  cm, respectively.

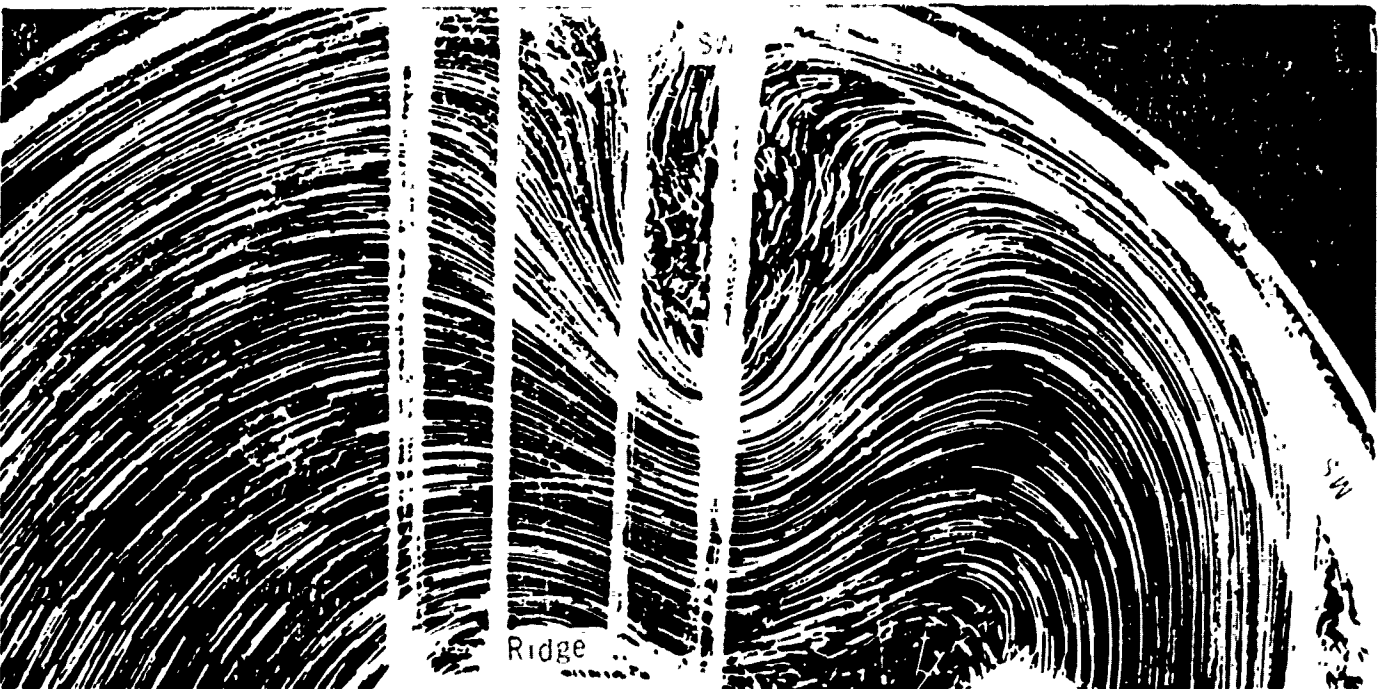
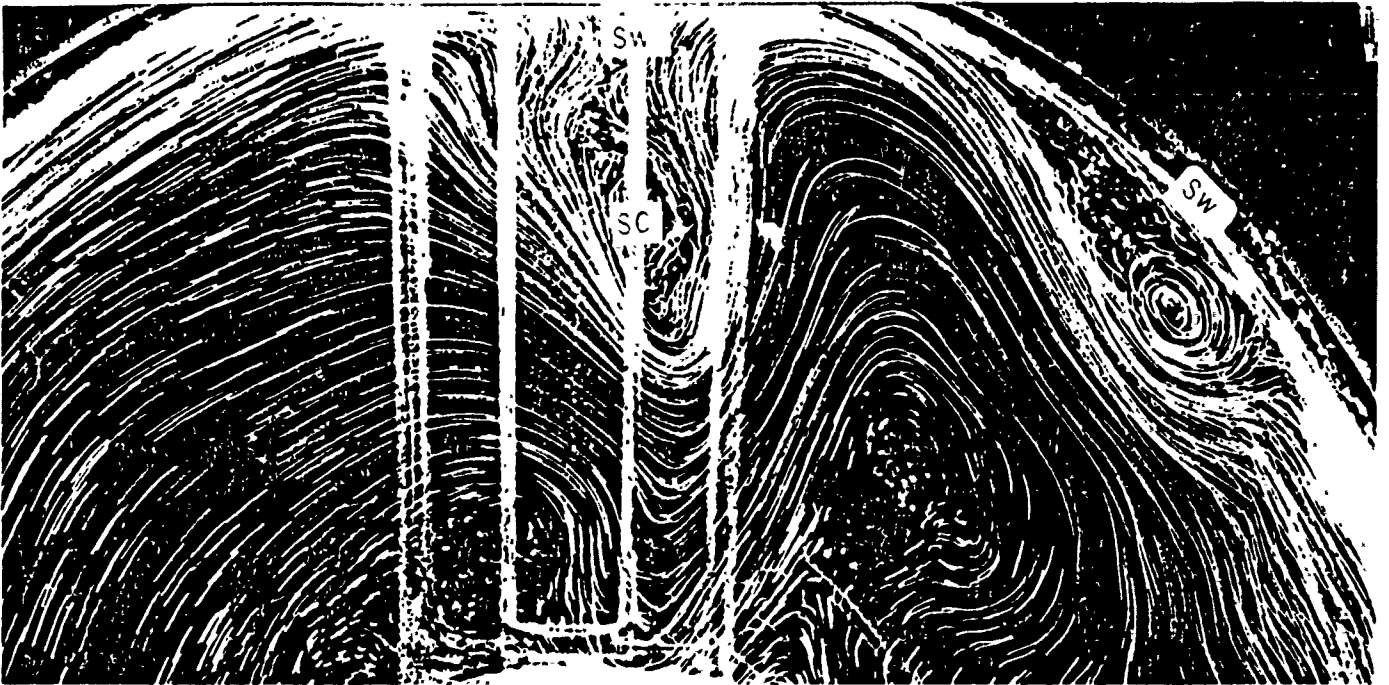
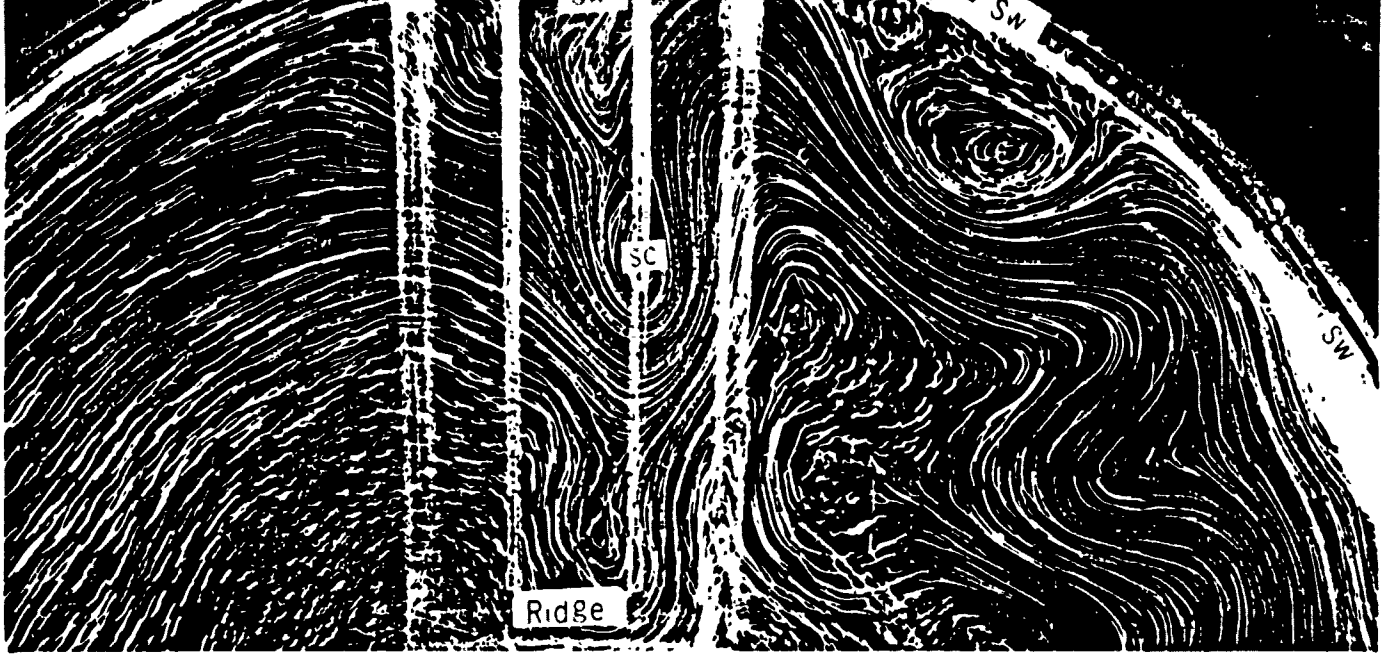
Fig. 9. A satellite (IR) image from the west coast of the USA (taken on July 1988, courtesy of Mark Abbot), showing structure of a meander generated by the Mendocino ridge (MD). A simplified contour map of the Mendocino ridge is shown, also.

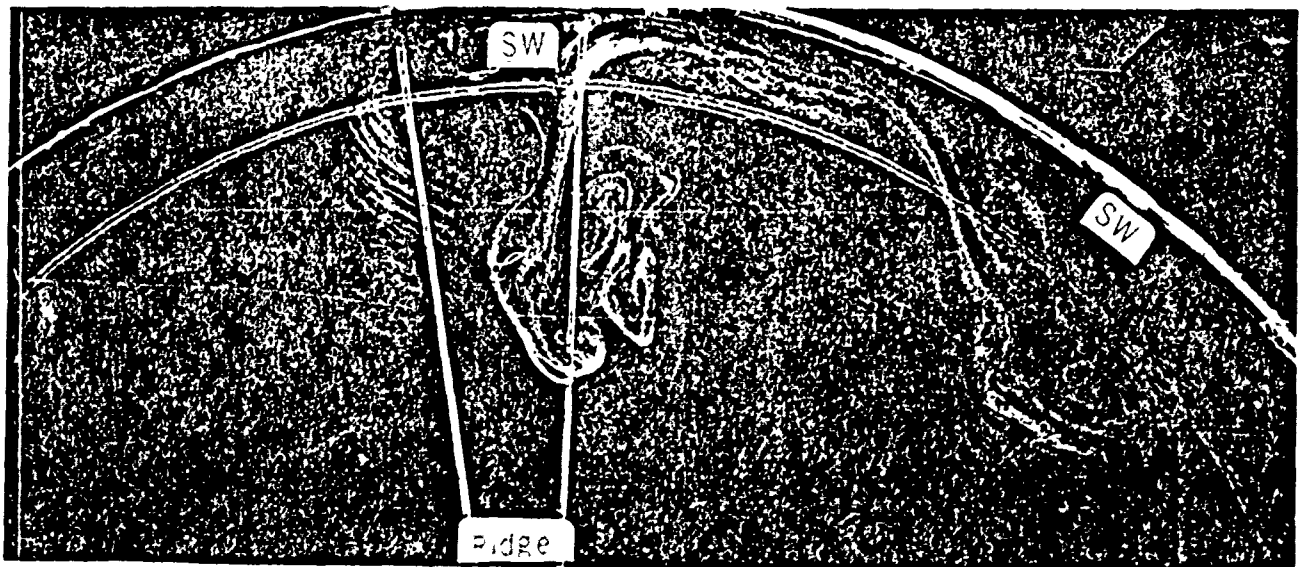
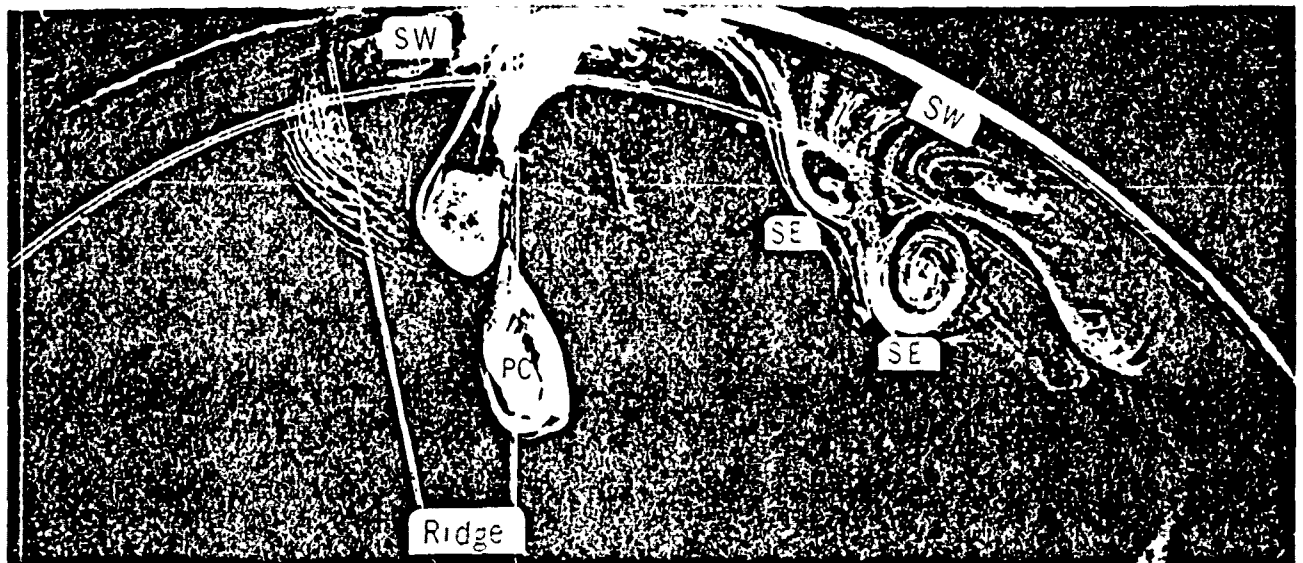
Fig. 10. A satellite (IR) image from the west coast of the USA (taken on September 1980, courtesy of Larry Breaker), showing an intense meander that is generated by the Mendocino ridge, with characteristics similar to some of the meanders generated in the laboratory model (for example see figures 2&3).

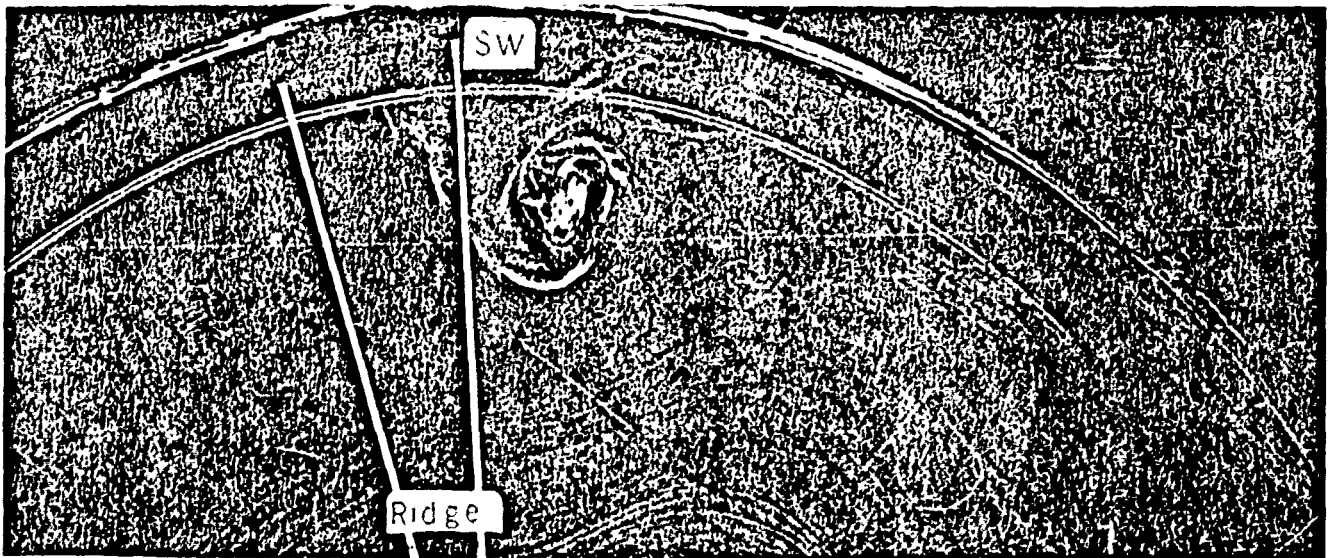
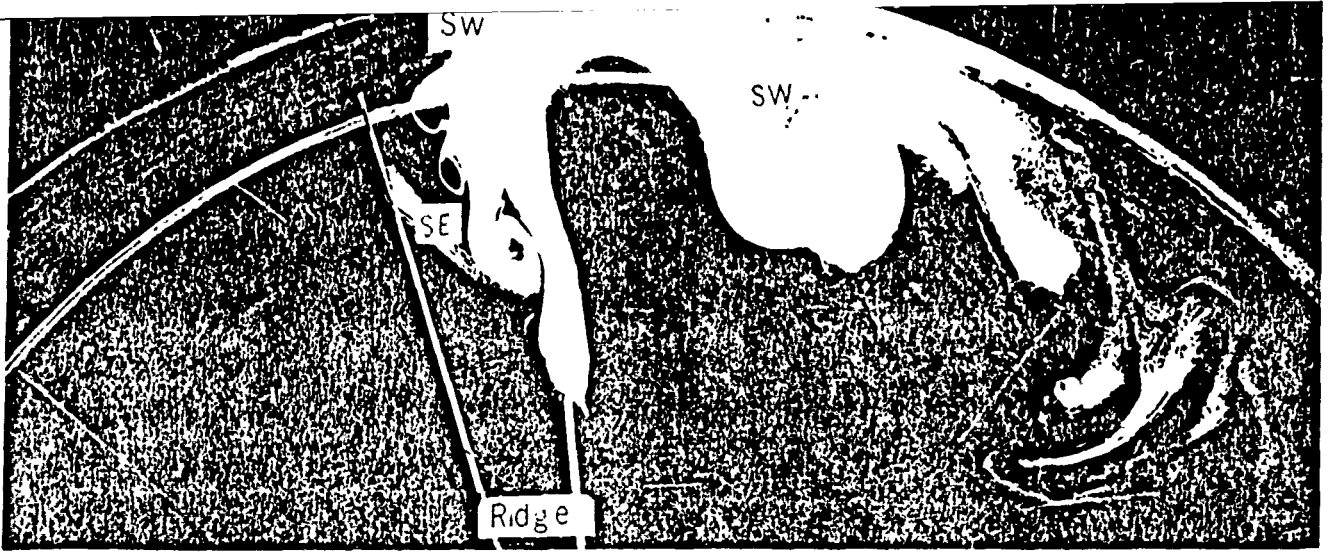
Fig. 11. A satellite (IR) image from the west coast of the USA ((taken on July 1981, courtesy of Pierre Flament), showing the structure of a meander generated by the Mendocino ridge and a pinched-off cyclone over the ridge.

Fig. 12. A satellite (IR) image from the west coast of the USA (taken on June 1980, courtesy of Larry Breaker), showing a pinched-off cyclone over the ridge at point Sur.

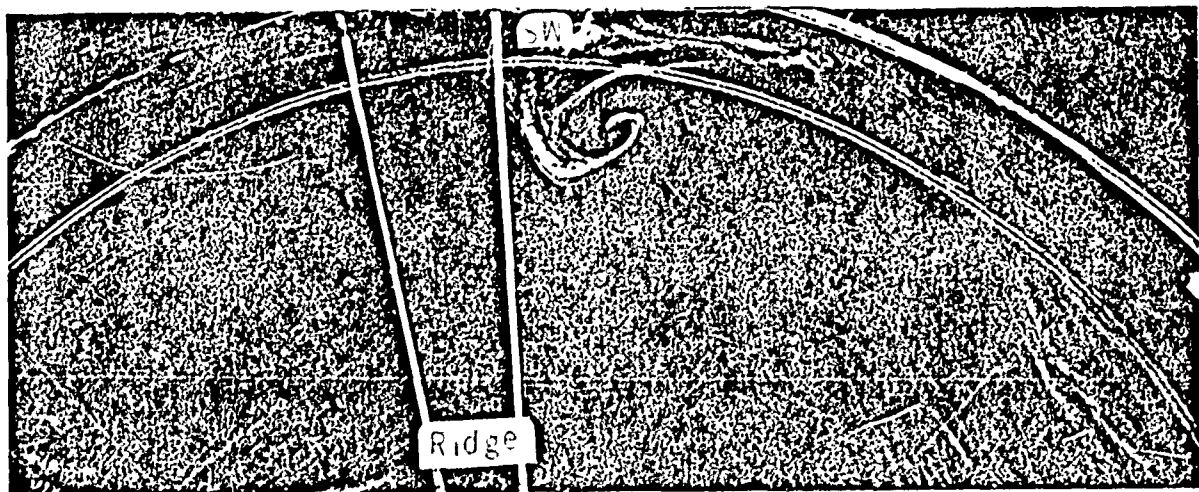
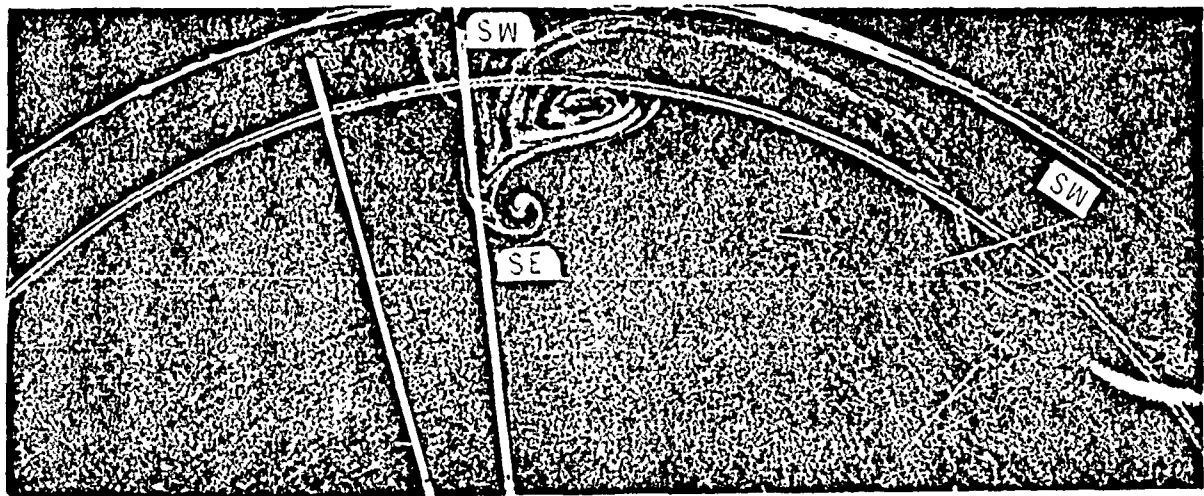
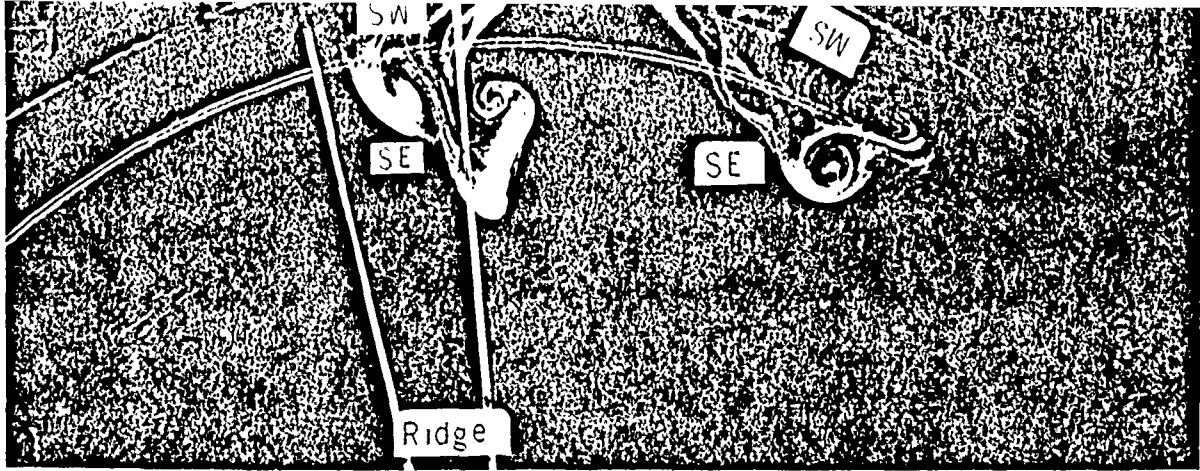














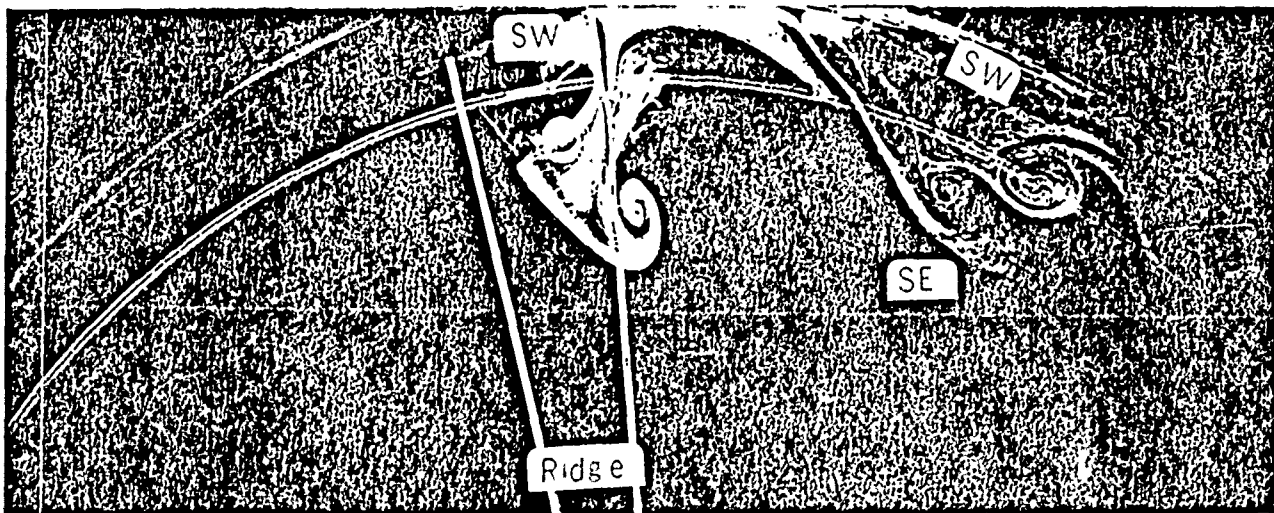
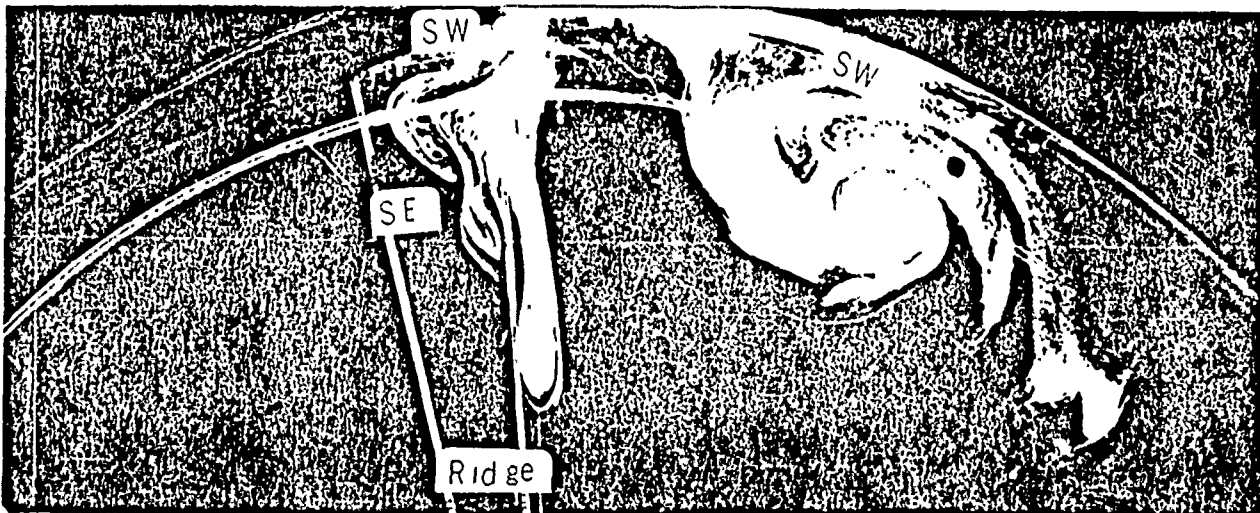
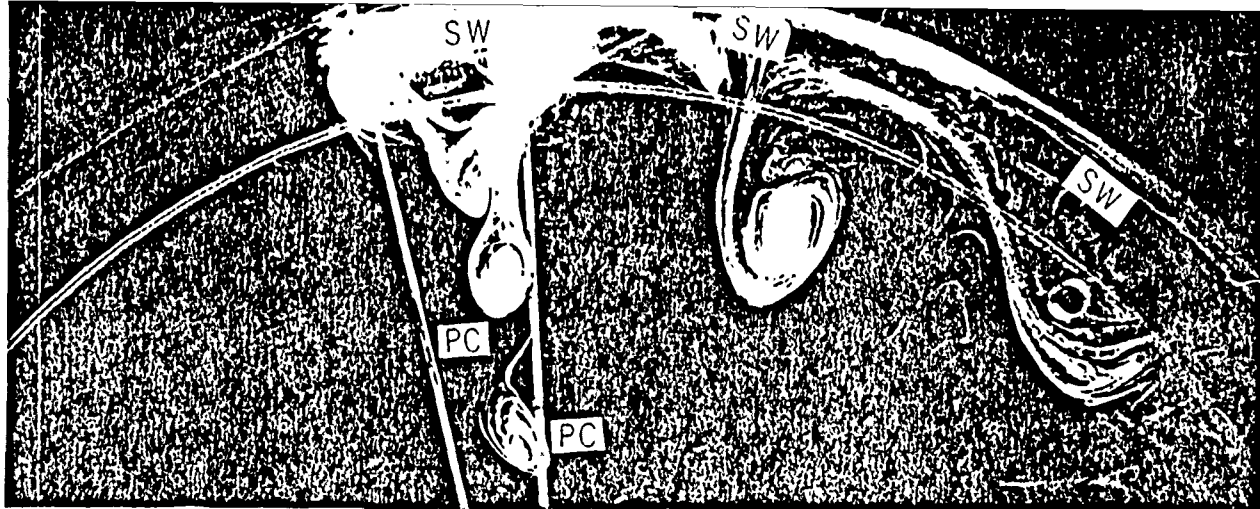


Fig 5

